Dissertation

submitted to the

Combined Faculties for the Natural Sciences and for Mathematics

of the Ruperto-Carola University of Heidelberg, Germany

for the degree of

Doctor of Natural Sciences

presented by

Diplom-Biologe Benedikt Felix Müller

born in: Gießen

Oral-examination: 28th of July 2015

Interactions of EGFR / IGF-1R Signaling in NSCLC

–

A Systems Biology Approach

Referees: Prof. Dr. Ursula Klingmüller

PD Dr. Kai Breuhahn

SUMMARY

Lung cancer is the leading cause of cancer-related deaths worldwide with 50,000 new cases per year in Germany and 220,000 in the USA. Non-small cell lung cancer (NSCLC) is the most prevalent variant, with the majority of cases classifying as the adenocarcinoma subtype. Advances in molecular diagnostics have revealed driving mutations in some tyrosine kinase receptors (TKRs), such as the EGF receptor (EGFR). Other TKRs like the IGF-I receptor (IGF-1R) have been implied in NSCLC carcinogenesis. Consequently, treatment strategies have evolved to include inhibitors against these TRKs (tyrosine kinase inhibitors, TKIs), but only with temporal benefit for the patient. Evidence pointing towards an important role of IGF-1 signaling in the evasion of inhibition of EGFR lead to double inhibition of EGFR and IGF-1R being tested in the clinics. Phase I and II trials were promising, but a phase III study failed to demonstrate benefit for the primary end point of progression-free survival after 12 weeks.

My project used a systems biology approach to investigate the role of the dynamic crosstalk between the signaling from EGFR and IGF-1R on NSCLC cells to better define the effects of pathway interaction and find causes for the failure of clinical combination treatment. To generate meaningful quantitative data for the phenotypical modeling of cell behavior, I established partly novel evaluation algorithms for 2D migration (in cooperation with the group of Dr. F. Matthäus) and 3D invasion (in cooperation with the group of Dr. D. Drasdo). In cooperation with the group of Prof. T. Höfer I could successfully establish a first unified ODE model of EGFR and IGF-1R signaling in NSCLC cells from quantitative time resolved pathway activation data. Even though microarray analysis of EGF stimulated NSCLC cells revealed upregulation of migration associated genes, phenotypical assays showed that NSCLC cell migration was dependent on a more complex signaling environment than double stimulation with EGF and IGF-1. On the other hand, I was able to show rescue of the NSCLC migratory behavior by IGF-1 stimulation after EGFR inhibition in a full medium setting, further corroborating the important role of the interaction between these two growth

SUMMARY

factors for the early spread of NSCLC. The migration data I generated is currently used in the development of an agent-based model of NSCLC migration by the group of Dr. F. Matthäus.

The data presented here and the associated computational evaluation algorithms and models will serve as the basis for the integrated multiscale modeling of the complex conditions governing NSCLC migration and the relevant cell signaling. Thus my work constitutes an important contribution towards understanding the intricate signaling responsible for the early spread of NSCLC and resistance against inhibition of particular TRKs.

ZUSAMMENFASSUNG

Lungenkrebs ist verantwortlich für die meisten krebsbedingten Todesfälle weltweit, mit 50.000 neuen Fällen pro Jahr in Deutschland und 220.000 in den USA. Das nicht-kleinzellige Lungenkarzinom (*non-small cell lung cancer*, NSCLC) ist die am weitesten verbreitete Variante, wobei die Mehrzahl aller Fälle als Adenokarzinom klassifiziert wird. Fortschritte in molekularer Diagnostik führten zur Entdeckung von Driving-Mutationen in *Rezeptor-Tyrosinkinasen* (RTKs) wie dem *EGF Rezeptor* (EGFR) während andere RTKs wie der *IGF-1 Rezeptor* (IGF-1R) mit der NSCLC Karzinogenese in Verbindung gebracht wurden. Folglich entwickelten sich Behandlungsstrategien, die Inhibitoren gegen diese RTKs (*Tyrosinkinase Inhibitoren*, TKIs) beinhalten, aber nur vorrübergehende Verbesserungen für Patienten bewirken. Aufgrund von Untersuchungen deren Ergebnisse auf eine prominente Rolle des IGF-1 Signalweges beim Umgehen der EGFR Inhibierung hinweisen, wurden Doppelinhibierungen von EGFR und IGF-1R in klinischen Studien getestet. Die Phase I- und II- Studien lieferten erfolgsversprechende Ergebnisse, aber eine Phase III-Studie konnte keine Verbesserung für progressionsfreies Überleben nach 12 Wochen als primärem Endpunkt erreichen.

In meinem Projekt verfolgte ich einen system-biologischen Ansatz, um die Rolle der dynamischen Netzwerke zwischen den EGFR und IGF-1R Signalwegen im NSCLC zu untersuchen. Ziel war es, die Effekte diese Interaktionen besser zu verstehen, um Gründe für den Misserfolg der Kombinationsbehandlung in der Klinik zu finden. Um brauchbare quantitative Daten für die Modellierung von phänotypischem Zellverhalten zu gewinnen, etablierte ich zum Teil neue Evaluierungsalgorithmen für 2D-Migration (in Zusammenarbeit mit der Gruppe von Dr. F. Matthäus) und 3D-Invasion (in Kooperation mit der Gruppe von Dr. D. Drasdo). Aus quantitativen, zeitaufgelösten Proteinaktivierungsdaten konnte ich in Zusammenarbeit mit der Gruppe von Prof. T. Höfer ein erstes ODE-Modell etablieren, dass die Signaltransduktion über EGFR und IGF-1R gemeinsam beschreibt. Obwohl Microarray-Analysen von NSCLC Zellen ergaben, dass migrationsassoziierte Gene nach EGF Stimulation

induziert wurden, zeigten phänotypische Versuche dass die NSCLC Zellmigration von komplexeren Signalvorgängen als der einfachen Stimulation mit EGF und/oder IGF-1 abhängt. Andererseits konnte ich zeigen, dass Stimulation mit IGF-1 die Reduktion der Migration von NSCLC Zellen nach EGFR Inhibierung teilweise aufheben kann, wenn den Zellen Vollmedium zur Verfügung steht. Dies unterstreicht die wichtige Rolle, die die Interaktion zwischen diesen beiden Wachstumsfaktoren in Bezug auf Streuung von NSCLC Zellen spielt. Die Migrationsdaten, die ich hier erhob, werden zurzeit in der Gruppe von Dr. F. Matthäus bei der Entwicklung eines agenten-basierten Modells der NSCLC Migration verwendet.

Die hier präsentierten Daten und die assoziierten computergestützten Evaluationsalgorithmen und Modelle werden als Grundlage für integrierte Multiskalenmodelle für die komplexen Zusammenhänge der NSCLC Migration und der relevante Signaltransduktion dienen. Somit stellt meine Arbeit einen wichtigen Beitrag zum Verständnis der vielschichtigen Signalweiterleitungsvorgänge dar, die für das frühe Streuen und die Resistenz gegen die Inhibierung einzelner RTKs verantwortlich sind.

Index

COMMON ABBREVIATIONS

ADC	Adenocarcinoma
AKT	v-akt murine thymoma viral oncogene
ALK	Anaplastic lymphoma kinase
AREG	Amphiregulin
ATCC	America Type Culture Collection
ATP	Adnosine triphosphate
B2M	Beta-2 microglobulin
bp	Base pair
Braf	v-Raf murine sarcoma viral oncogene homologue B1
cDNA	Complementary DNA
CREB	cAMP response element binding protein
DMEM	Dulbecco's modified Eagle's medium
ECM	Extracellular matrix
EGF	Epidermal growth factor
EGFR	Epidermal growth factor receptor
EMT	Epithelial mesenchymal transition
ERK	Extracellular-signal-regulated kinases
FACS	Fluorescence-activated cell sorting
FAK	Focal adhesion kinase
FCS	Fetal calf serum
GO	Gene ontology
HB-EGF	Heparin-binding EGF
HCC	Hepatocellular carcinoma
HNSCC	Head and neck squamous carcinoma
IGF-1	Insulin-like growth Factor-1
IGF-2	Insulin-like growth Factor-2
IGF-1R	Insulin-like growth Factor-1 Receptor
IHC	Immunohistochemical staining
Iκ-K	Inhibitor kappa B protein kinase
JAK2	Janus kinase 2
KRas	V-Ki-Ras2 Kirsten rat sarcoma viral oncogene homologue
LCC	Large cell lung carcinoma
MDM2	Murine double minute 2
MEK1	Mitogen-activated protein kinase kinase-1
MEM	Minimal essential medium
MMP3	Matrix metallo-proteinase 3

MS	Mass spectrometry
mTOR	Mechanistic target of rapamycin
mut	Mutant
NEAS	Non-essential amino acids
NF κB	Nuclear factor 'kappa-light-chain-enhancer' of activated B-cells
NSCLC	Non-small cell lung cancer
ODE	Ordinary differential equation
OS	Overall survival
PBS	Phosphate-buffered saline
PCA	Principal component analysis
PI	Propidium Iodide
$PIP2$	Phosphatidylinositol-4,5-bisphosphate
$PIP3$	Phosphatidylinositol-3,4,5-trisphosphate
PFS	Progresssion free survival
PTB	Phosphotyrosine binding domain
PTEN	phosphatase and tensin
qRT-PCR	Quantitative real-time PCR
SCC	Squamous cell carcinoma
SCLC	Small cell lung cancer
SD	Standard deviation
$SH2$	SRC homology 2 domain
Shc	SH2 domain containing protein
siRNA	Short interfering RNA
$STAT3$	Signal transducers and activators of transcription 3
SOS	Son of sevenless
TGF-β	Transforming growth factor β
TKI	Tyrosine kinase inhibitor
TKR	Tyrosine kinase receptor
wt	Wild-type
XIAP	X-linked inhibitor of apoptosis protein

FIGURE INDEX

TABLE INDEX

1 Introduction

1.1 Lung cancer

1.1.1 Clinical relevance, epidemiology, and etiology of lung cancer

Lung cancer is one of the most important cancer types worldwide, with about 50,000 new cases per year in Germany and 220,000 in the USA. It is the second most common entity with regard to new cases in both men and women, after prostate cancer in men and breast cancer in women, respectively.[1] It is the leading cause of cancer-related deaths, accounting for up to 25% of all cancer-associated deaths in the industrialized nations. The highest incidence rates are found in Europe, North-America, and East-Asia, especially China.[2] The main reason for the development of lung cancer, especially in the industrialized nations, is smoking, with an estimated 85% of affected males and 47% of affected females being smokers or former smokers. Further risk factors, aside from the tobacco-associated carcinogens, are various substances like asbestos, arsenic, and cadmium.[3]

Lung cancer is subdivided in several subclasses. Classification historically differentiates between *small cell lung cancer* (SCLC) and *non-small cell lung cancer* (NSCLC), with NSCLC encompassing various subgroups, based on histological diagnosis. NSCLC is the most prevalent form with about 85% of all lung cancers (Figure 1 A, B). Five-year survival rates vary between 61% in early tumor stages, and only 1% in Stage IV,[3] with the mean survival

rate being as low as 15%. This low number can be explained by the fact that 65% of patients present with locally advanced or metastatic disease,[4] due to very little symptoms in the first phases of cancer development. Additionally, NSCLCs metastasize early and aggressively, which results in over 75% of tumors being inoperable at the moment of first diagnosis. The biggest subgroup under NSCLC are *adenocarcinoma* (ADC), that make up the majority of cases with about 60%, followed by *squamous cell carcinoma* (SCC) and then *large cell lung carcinoma* (LCC) and other forms like adeno-squamous and sarcomatoid carcinomas. (Figure 1 C)
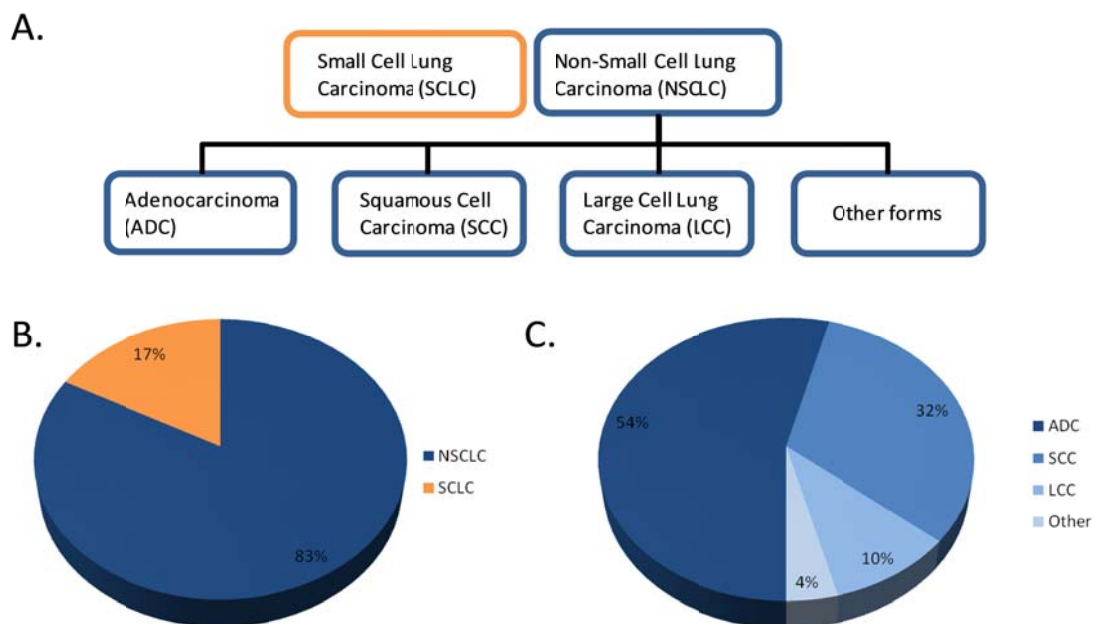
Figure 1: Histological classification of lung cancer. (A) Overview over the histological subtypes in lung cancer. (B) Distribution of SLC and NSCLC. (C) Distribution of NSCLC subtypes. Percentages were taken from Lortet et al.[5]

According to the current WHO-classification, ADCs are divided in the histological growth patterns acinary, papillary, bronchiovascular, and solid. More than 80% of all ADCs grow in a mix form of different growth patterns and are therefore placed in the group of mixed ADC. This is problematic with regard to prognostic stratification, as recent studies strongly imply that the tumor architecture can predict biological behavior and is correlated with specific molecular alterations.[6] In the last decade, advances in molecular diagnostics have made it possible to enhance traditional histological evaluation by identifying driving mutations in cancer (Figure 2). Especially for ADCs, mutations in *V-Ki-Ras2 Kirsten rat sarcoma viral oncogene homologue* (K-Ras), *epithelial growth factor receptor* (EGFR), *v-Raf murine sarcoma*

viral oncogene homologue B1 (B-Raf), and *anaplastic lymphoma kinase* (ALK) are the most common therapeutically relevant alterations.[7]

While some mutations can serve as markers, others represent druggable targets for therapy. In the latter group, *tyrosine kinase receptors* (TKRs) like the EGFR have been identified as especially promising, due to their central role in interpreting environmental signals and their exposed location on the cell surface.
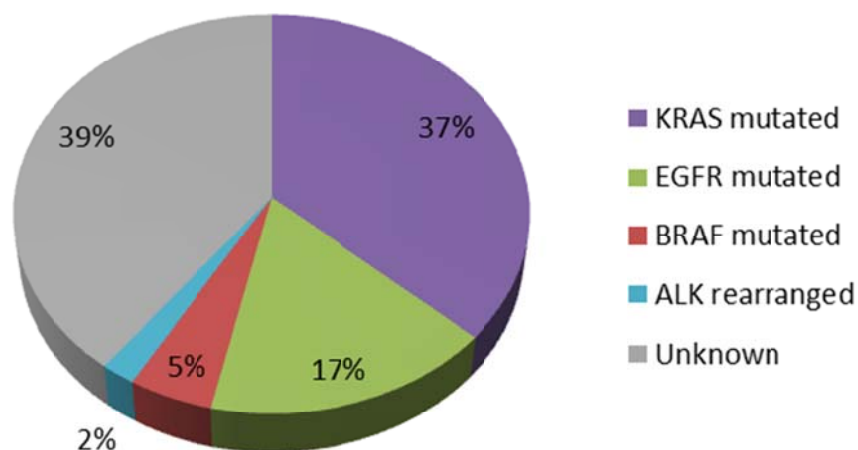
Figure 2: Distribution of common oncogenic driver mutations in resected stage II-IV pulmonary adenocarcinomas (n=150). KRAS: V-Ki-Ras2 Kirsten rat sarcoma viral oncogene homologue; EGFR: epidermal growth factor receptor; BRAF: v-Raf murine sarcoma viral oncogene homologue B1; ALK: anaplastic lymphoma kinase. Modified after Warth et al.[6]

1.1.2 Treatment options

Treatment options for lung cancer have evolved with the advent of molecular profiling and the discovery of druggable driving mutations. In some cases, progression-free survival could be as much as doubled. Nevertheless, long term survival shows no big improvement, with the 5-year survival rates having risen, from 12% in 1977 to 18% in 2009 (compared to e.g. prostate cancer with an increase from 68% in 1977 to 100% in 2009). Generally two options arise, depending on the progression of the disease: if the tumor is deemed inoperable at first diagnosis, only palliative therapy remains. If an operation is still possible, it is usually supplemented by adjuvant radio- and/or chemotherapy for tumor stages II and up. Platinum compounds like cisplatin and pemetrexed are the clinical standard for both the palliative treatment and the supplement therapy after resection.[4] The precise classification of the tumor remains increasingly relevant, as the specific administration of chemotherapeutics

(e.g. permetrexed for ADC) is linked to the histological type. This stratification has led to minor increases in median survival from 8 to 12 months and longer in clinical studies (e.g. shown by Sandler et al.[8]). Still, to date, traditional chemotherapy approaches, even with third generation drugs such as paclitaxel, leave much to be desired concerning *overall survival* (OS) and *progression free survival* (PFS).

Discovery of driving mutations in TKRs has fostered hope for new treatment options that can on the one hand circumvent the adverse side effects of platin-based chemotherapy, but more importantly offer new and improved approaches to handle inoperable cases. Consequently, treatment strategies have evolved to include inhibitors against these TKRs (*tyrosine kinase inhibitors*, TKIs), which in some cases lead to stark increases in OS from few months under conventional chemotherapy to over two years under TKI treatment, for patient groups which carry the relevant mutations (see Figure 3).[9]
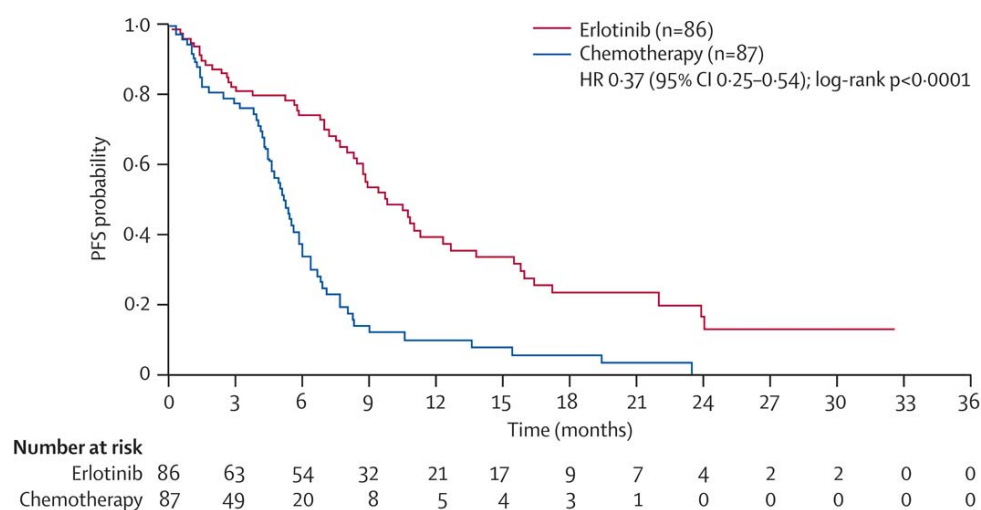
Figure 3: Kaplan-Meier curves of PFS for standard chemotherapy and Erlotinib treatment according to radiographic evidence. From the European EURTAC patient cohort, modified after Rosell et al.[9]

Nevertheless, virtually all patients suffer from relapse after 3 years or less, which leads to the still very low 5-year survival rate. A number of mechanisms have been proposed to explain this, the most prominent being the acquisition of secondary mutations that confer resistance on the receptor level (e.g. the T790M mutation in the EGFR[10]), but also phenotypic transformation like e*pithelial mesenchymal transition* (EMT) or transformation to SCLC[11] and others. Interestingly, recent evidence indicates that in addition to direct molecular alterations, tumors can evade inhibition of single signaling pathways by exploiting the intrinsic redundancy of growth factor signaling.[12]

1.2 Cell signaling

Cells constantly sense and interpret their environment through growth factors binding to receptors on the cell surface. After ligand binding, receptors get modified (e.g. phosphorylated) and enable adaptor proteins to bind the activated receptor and subsequently facilitate the transduction of the signal through cascades of intracellular signaling molecules into the cell. Ultimately, the signaling cascades trigger specific cell reactions, which are often connected to, or the result of changes in gene expression.

Indeed, dysregulation of cell signaling lies at the core of most cancers. Arguing from the expanded hallmarks of cancer introduced by Weinberg and Hanahan (Figure 4),[13] the major characteristics of the cancer cells themselves as well as the effects on their microenvironment are either caused by, or result in changes in cell signaling. For example, sustained proliferation can be achieved by constitutively activated growth factor receptors like EGFR and evasion of growth suppressors can be a result of mutations that de-sensitize the relevant signal transduction proteins for negative feedback regulation. Likewise, changes in the tumor microenvironment can lead to altered signaling by modulating the incoming signals (e.g. increased cytokine concentrations during tumor-promoting inflammation). Thus, cell signaling presents an important target with regard to cancer therapeutics.
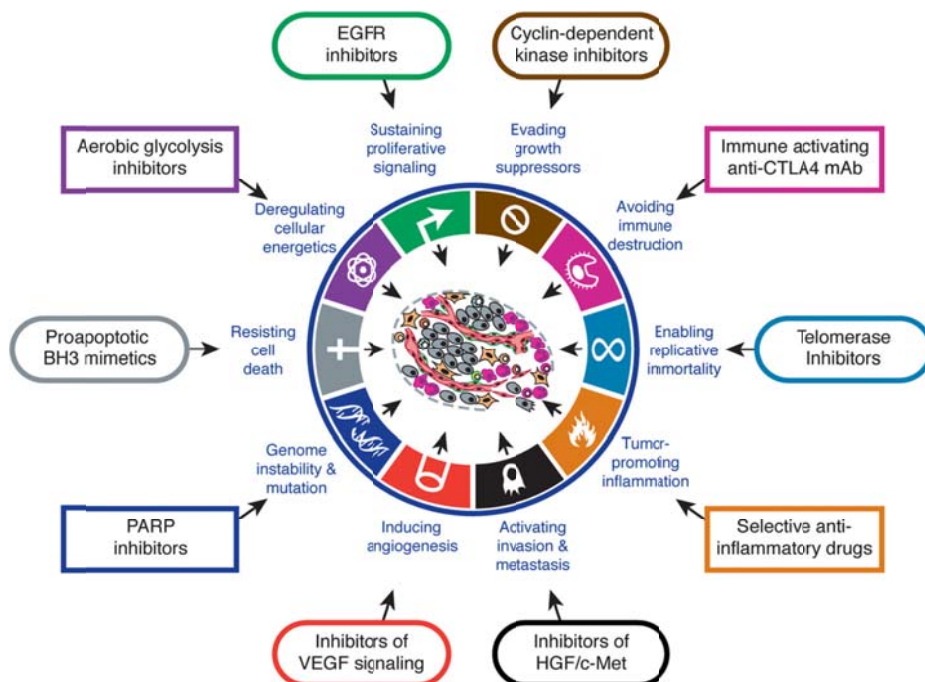
Figure 4: Therapeutic targeting of the "Hallmarks of Cancer" from Weinberg and Hanahan, 2011. Drugs listed are examples of therapeutic intervention strategies that target cell signaling. Modified after Weinberg and Hanahan[13].

1.2.1 Tyrosine kinase receptors

TKRs are one of the main groups of cytokine receptors bound to the cell surface. They typically consist of a single hydrophobic membrane-spanning α-helix connecting an extracellular with a cytosolic domain. TKRs bind soluble or membrane bound peptide hormones like the *epithelial growth factor* (EGF), *Insulin-like growth factors* (IGFs), or the *platelet derived growth factor* (PDGF), which facilitate their tyrosine-specific phosphorylation activity. In most cases, TKR molecules dimerize upon ligand binding and each monomer phosphorylates defined tyrosine residues on the cytosolic domains of its heterologous receptor partner (Figure 5). This leads to conformation changes which, depending on the specific receptor, facilitate the binding of ATP or protein substrates. In a second step, additional amino-acid residues in the cytosolic domain are phosphorylated and can subsequently act as binding sites for proteins that are responsible for the further signal transduction. After ligand binding, many TKRs are internalized and either recycled to the cell surface after deactivation, or directly degraded in lysosomes or proteasomes.[14]

1.2.2 Intracellular signal transduction

In order to affect the cellular phenotype, the signal received by the receptor at the cell surface has to be transduced into the cell interior, resulting e.g. in changes of protein activation, and all the way to the nucleus to impact gene expression. TKRs usually relay their activation *via* adaptor molecules, which then in turn bind and activate other molecules that harbor enzymatic activities. The main classes of these adaptors are proteins that incorporate either the *SRC homology 2* (SH2) or the *phosphotyrosine binding* (PTB) domains. These domains bind to distinct amino-acid sequences that include phosphotyrosine residues. Subsequently, further domains of the adaptors are utilized by signal-transduction molecules and thus initiate signaling cascades that ultimately end in changes of gene expression. Two of the most important downstream signaling pathways are those which transmit the activation along the Ras/MAPK/ERK cascade and the PI3K/AKT axis (Figure 5).

The Ras/MAPK/ERK signaling pathway

After the respective TRK has bound its ligand and is activated, the first adaptor protein binds and recruits further factors like GRB2, followed by the *son of sevenless* (SOS) homolog protein and others that ultimately result in the loading of the membrane-bound Ras protein with GTP (Figure 5).[15] GTP-bound Ras then in turn activates Raf by recruiting it to the membrane.[16] Ras and Raf represent a multi-gene families: there are three Ras members (K-Ras, N-Ras and H-Ras)[15] and three Raf members (B-Raf, RAF-1/c-Raf and A-Raf)[16]. After

activation, Raf is responsible for *serine/threonine* (S/T) phosphorylation of *mitogen-activated protein kinase kinase-1* (MEK1).[15,17,18] MEK1 phosphorylates *extracellular-signal regulated kinases* (ERK) 1 and 2 at specific *threonine* (T) and *tyrosine* (Y) residues.[19] Activated ERK1 and ERK2 act as S/T kinases and further activate a variety of substrates by phosphorylation.[15,17-19] ERK1/2 has many downstream targets and can regulate its own activation by acting on upstream substrates in feedback loops.[20] Consequently, ERK 1/2 is part of many signaling pathways and can cross-activate others. For example, ERK activated p90Rsk1 can activate the *cAMP response element binding protein* (CREB) transcription factor.[21]

To date, the number of identified ERK1/2 targets lies in the hundreds. Through these, ERK1/2 is involved in processes like cell cycle progression[22] and *extracellular matrix* (ECM) density[23]. With regard to migration, especially expression of slug protein, has been shown by Chen et al.[24] to be regulated by ERK1/2 in breast cancer. Additionally, ERK1/2 is involved in cell migration by directly activating calpains and the *focal adhesion kinase* (FAK), among others.[25]

The PI3K/AKT/mTOR signaling pathway

The *phosphatidylinositol 3 kinase* (PI3K) pathway is also a central node in the cellular signaling network (Figure 5). Upon activation by phosphorylated TKRs, the p110 subunit of PI3K phosphorylates *phosphatidylinositol-4,5-bisphosphate* (PIP2) to generate the active second messenger *phosphatidylinositol-3,4,5-trisphosphate* (PIP3), which recruits AKT to the plasma membrane, resulting in its phosphorylation and thus its activation. AKT itself is a S/T kinase that can translocate to the nucleus[26,27] and regulate a very broad spectrum of downstream targets,[28,29] thus having an impact on many cellular processes. As such, AKT effects on proliferation and cell cycle progression have been shown to be conveyed by regulation of p53 (*via murine double minute* 2 (MDM2)) or NFκB (via *inhibitor kappa B protein kinase* (Iκ-K)).[30] This promotes the transcription of genes involved in anti-apoptotic and proliferative responses such as *X-linked inhibitor of apoptosis protein* (XIAP), the apoptosis regulating protein BCL-2, survivin and others.[31] Additionally, cell cycle progression and survival is directly affected by phosphorylation of GSK3,[32] leading to reduced degradation of cyclin D1 and the down regulation of the apoptotic effector caspase 9. AKT has also recently been shown to be implicated in the regulation of EMT and cell migration.[33]

.
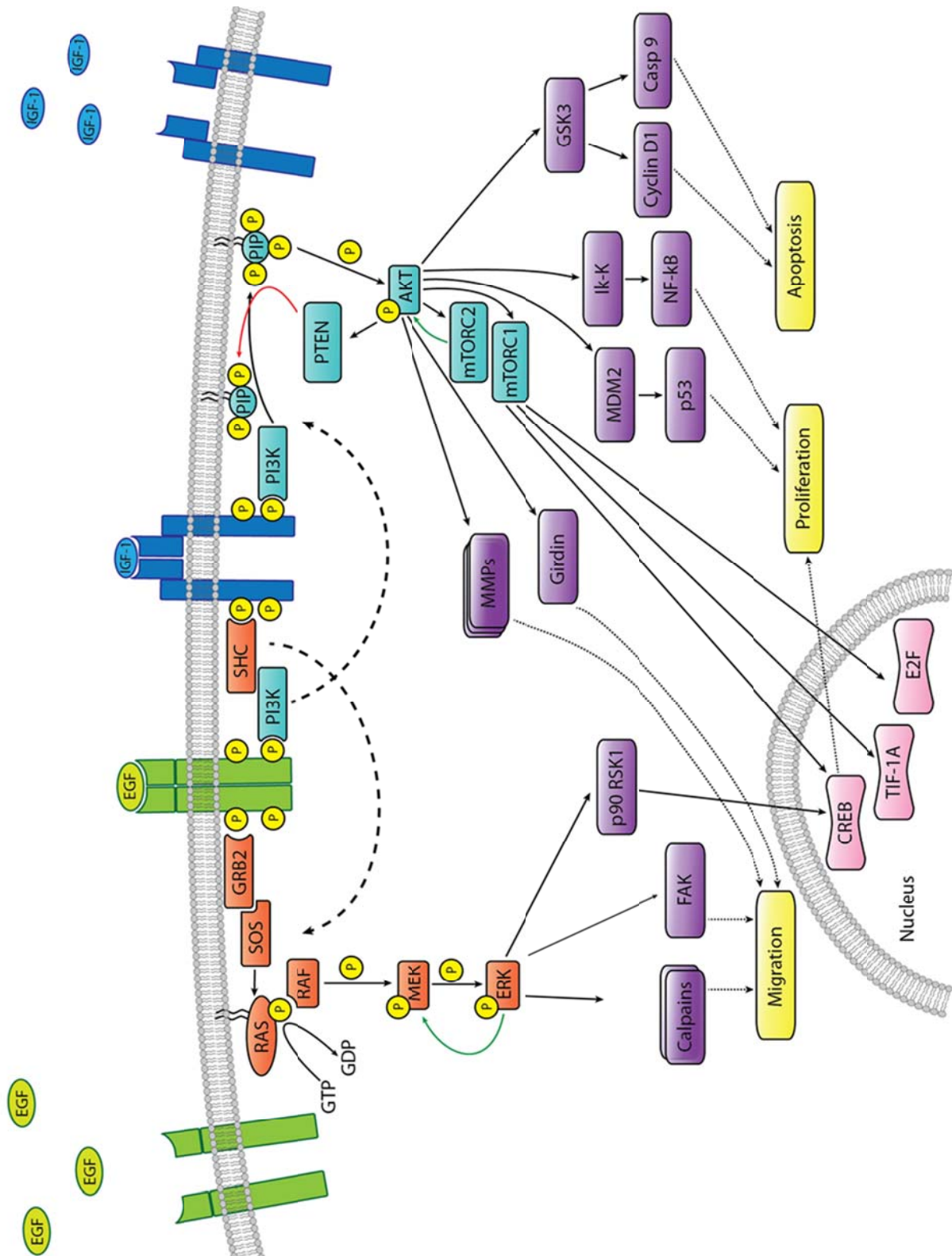
Figure 5: Overview of the EGF and IGF-1 pathways and the downstream effectors relevant in this study. Both IGF-1 and EGF lead to dimerization of their receptors upon binding. The phosphorylation signal is transduced from both receptors along both the ATK and the ERK pathway.

This is achieved through mechanisms like cytoskeletal remodeling (e.g. *via* Girdin[34]) and *matrix metalloproteases* (MMP) production (as shown for fibrosarcoma by Kim et al.[35]). The best described target of AKT is the *mechanistic target of rapamycin* (mTOR) complex with mTORC1-Raptor and mTORC2-Rictor. mTORC1 is responsible for the activation of transcription factors (like TIF-1A[36], CREB[37] and E2F[38]), leading to the expression of genes connected to survival and cell growth, whereas mTORC2 seems to build a positive feedback loop by activating AKT through phosphorylation (Figure 5). Another important node in the pathway is the *phosphatase and tensin* (PTEN) analog protein that acts as an endogenous pathway repressor by de-phosphorylating PIP3 to PIP2.[20]

Considering the multitude of biological processes that are controlled by both pathways, their central role in carcinogenesis upon deregulation becomes apparent, and indeed, aberrant activation of AKT and/or ERK has been shown to be central in lung cancer and affected by treatment. [39,40]

1.2.3 The epithelial growth factor receptor in lung cancer

Structure and signaling

The EGFR, also known as ErbB1/HER-1, is a member of the EGFR family, which also comprises ErbB2/Neu/HER-2, ErbB3/HER-3 and ErbB4/HER-4, all exhibiting the typical TRK structure.[41] EGFR is activated by EGF, *transforming growth factor alpha* (TGF-α), and a number of additional possible ligands like *amphiregulin* (AREG) and *heparin-binding EGF* (HB-EGF). After ligand binding and dimerization (Figure 5), the major first adaptor proteins for EGFR are from the SH2 family such as GRB2, SHC and PLCγ[42], while further downstream signaling is mediated through STAT5 or the Ras/Raf/MAPK and PI3K/AKT pathways (as illustrated in 1.2.2). Through these, EGFR signaling has been shown to be involved in cell proliferation and survival as well as migration.[25]

Relevance in lung cancer

EGFR has been shown to be heavily involved in many human cancer entities, with expression levels strongly affecting the clinical outcome of cancer patients,[43,44] but in lung cancer, EGFR mutations are more relevant than overexpression.[7,45] As discussed in 1.1.1, driver mutations in two thirds of all NSCLCs can be identified by molecular diagnostics. Among these, EGFR-mutations are seen in roughly one third of cases (which translates to 25% of all NSCLCs), with only K-Ras mutations occurring at similar levels.[7,46] NSCLCs that are responsive to specific EGFR inhibition by TKIs are usually associated with EGFR mutations (with some

exhibiting increased EGFR copy number)[47,48]. The EGFR mutations that are most relevant for clinical application are short in-frame deletions of the conserved LRE (Leucine-Arginine-Glutamic acid) motif in exon 19 and point mutations resulting in the substitution of L858 in exon 21 (Figure 6). To date, more than 20 different exon 19 deletions have been identified in lung adenocarcinomas. Cheng et al. and Chung et al. showed that among patients with exon 19 deletions, those with non-LRE deletions had a lower response to EGFR-specific TKIs compared with those harboring LRE deletions.[49,50] However, OS was not significantly different among mutation position groups. Both these mutations (the LRE deletions and the L858 substitutions) are gain-of-function mutations, together accounting for over 85% of all EGFR mutations in NSCLC (Figure 6).[51] They occur more frequently in females, Asians, and in non-smokers[52-54] and, intriguingly, seem to be rather specific for NSCLC, occurring only at a very low frequency in other tumors such as head and neck, ovarian, pancreatic, and colorectal cancers.[45] Interestingly, the mutations occur in the ATP binding cleft of EGFR, which is where first-generation EGFR TKIs bind, imparting sensitivity to those drugs.[45,55] Other less commonly detected sensitizing EGFR mutations include the G719A/C/S and S720F mutations in exon 18, the L861Q/R mutations in exon 21, and the V765A, T783A, and S768I mutations in exon 20.[45,49,56,57]
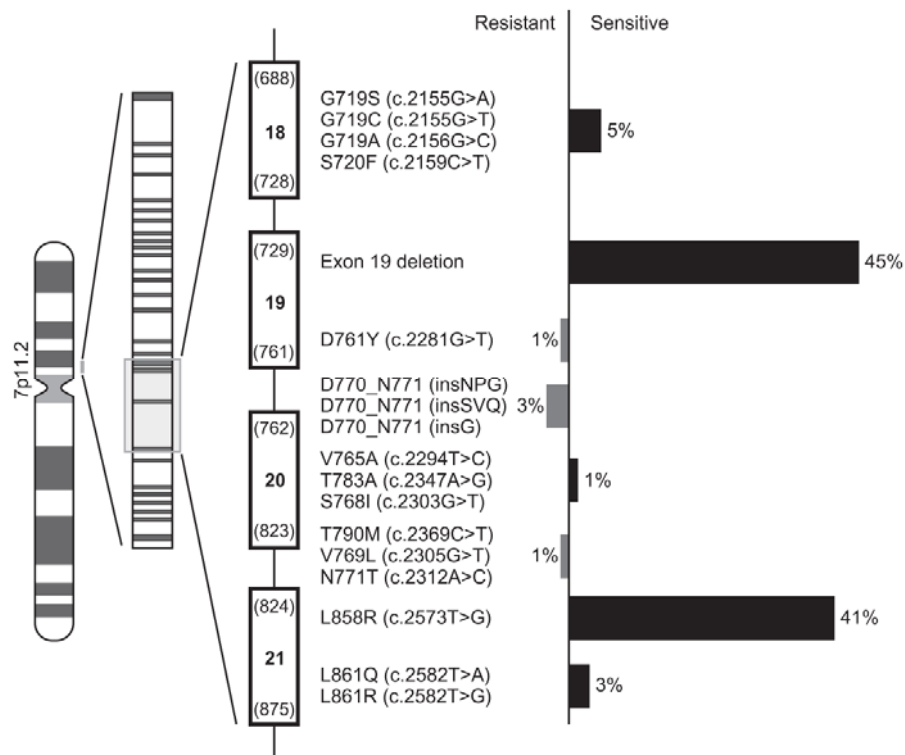
Figure 6: Frequency of mutations in exons 18–21 of the EGFR gene and the association with responsiveness to EGFR TKIs. The diagram depicts the locations and frequencies of EGFR gene mutations detected in NSCLC patients. The most common EGFR mutations are exon 19 deletions and exon 21 point mutations at codon 858, which together account for approximately 80–90% of cases. Modified after Roengvoraphoj.[51]

Therapeutic approaches

These data led to the development of small molecules EGFR inhibitors, such as Erlotinib[58] and Gefitinib[45,59]. Both compounds have been used in the clinic to some success. However, only stabilizing effects of up to 12 months could be achieved. Although the overall response to EGFR TKIs is high for patients with EGFR mutations, almost all patients subsequently develop acquired resistance to Gefitinib and Erlotinib within 10–16 months.[60]

This acquired resistance is conferred in part by additional point mutations in the EGFR at position 790 within the kinase domain, the most prominent one being T790M.[61,62] The T790M mutation weakens the interaction of the inhibitor with the kinase and is analogous to other drug-resistance conferring mutations found in BCR-Abl, PDGFR, and c-Kit, suggesting a general reliance on similar cellular survival or proliferation pathways.[45,63]

Due to the sobering performance of first generation EGFR inhibitors in the clinic, considerable effort has been put in the development of alternative approaches, resulting in second-generation EGFR inhibitors. Some of the more effective approaches combine irreversible inhibition of several ErbB family members with compounds like HKI 272, HKI 357 and Afatinib (BIBW2992). Afatinib was shown to effectively overcome Erlotinib resistance *in vivo* and in xenograft models[48] and was subsequently used successfully in clinical trials[64]. These inhibitors act by covalently binding of cysteine residues, which also confers the ability to overcome the resistance mutations.

1.2.4 The insulin-like growth factor-1 receptor in lung cancer

Structure and signaling

The *insulin-like growth factor-1 receptor* (IGF-1R) is a TRK that shares high homology with the *insulin receptor* (IR), especially in the cytoplasmic kinase domain. Its structure deviates from the conventional TRK blueprint, as it is a heterotetrameric protein with two extracellular α-subunits and two transmembrane β-subunits containing the kinase domains.[65,66] Its main ligands are IGF-1 and IGF-2[67] with their bioavailability being prominently regulated by *IGF binding proteins* (IGFBP1-6)[65]. After ligand binding and reciprocal phosphorylation of the β-subunits, adaptor proteins such as *SH2 domain- containing* (Shc) protein and the PTB-containing *insulin receptor substrates* (IRS1–4) are recruited to the phosphorylation sites.[15,68] Downstream signaling is then mediated along overlapping pathways with a number of other TRKs: the Ras/Raf/MAPK, PI3K/AKT, and JAK2/STAT3 axis (Figure 5).[65]

Relevance in lung cancer

IGF-1R has been reported to be relevant for tumor growth[69] and the IGF-1 system has been shown to be frequently expressed in lung cancer and many different malignant[67,70] and premalignant tissues,[71] as well as NSCLC cell lines.[72] Furthermore, high circulatory IGF-1 levels have been linked to incidence and severity in lung cancer.[73] Consequently, the development of TKIs targeting IGF-1R *via* small molecular inhibitors like OSI-906 and *Picropodophyllin* (PPP) as well as neutralizing antibodies like Cixutumumab and Figitumumab has been in the focus of many scientific efforts. Preclinical data of combination approaches of chemotherapy and Figitumumab,[74] as well as the respective phase I and phase II trials[75,76] were very promising. Unfortunately and somewhat unexpectedly, a phase III trial investigating the combination of Figitumumab with Erlotinib resulted in termination due to worse overall survival in the group receiving Figitumumab.[77]

To date, we do not have comprehensive data on resistance mechanisms like IGF-1R mutations that might cause the adverse effect seen in the Phase III trials.[78] However, the combination of promising in vitro results with sobering clinical data hints at causes that could lie in the interconnected signaling environment of the in vivo situation.

1.2.5 Interactions between EGFR and IGF-1R signaling

It has been hypothesized that tumors evade inhibition of single signaling pathways by exploiting the intrinsic redundancy of growth factor signaling. This redundancy presents itself in the form of a tightly interwoven network, where inputs from different receptors are integrated on the same downstream nodes. Not only are most signaling pathways highly connected, the general shape of the topology of the signalosome can be described as a bow-tie structure, with many different inputs being interpreted by a low number of central signal transduction molecules. This then again leads to a highly diverse output of cell reactions on many different levels (e.g., transcriptional, phenotypical) (Figure 7, discussed in [79]).
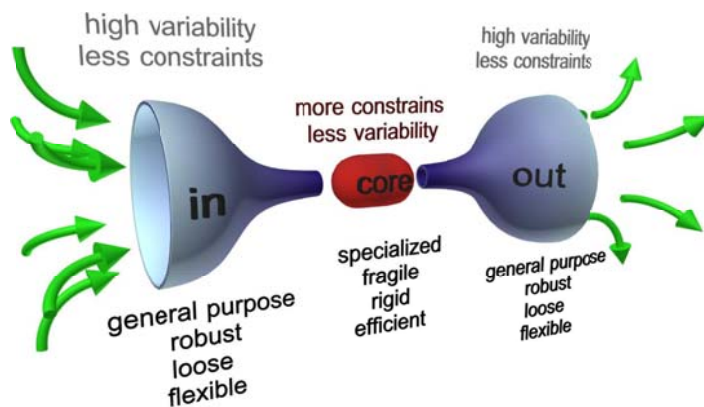
Figure 7: Schematic representation of a general bow-tie architecture. Varied input signals (left) confer flexibility and robustness on the system. In the core, inputs (and information complexity) are 'compressed' by relatively rigid rules and protocols, and processed into basic modular building blocks. Finally, a variety of elaborated output fans out, and the complexity of the original, uncompressed information is restored. Output-input feedback loops may also occur. Modified after Tieri et al.[78]

Consequently, EGFR and IGF-1R share downstream signaling along the JAK-STAT, PI3K/AKT, and Raf/MAPK/ERK pathways. In addition to the shared pathways, heterodimerization events between the two receptors have been shown in different tumor cell types, which may further hamper the establishment of highly specific therapeutic options for individual receptors.[80] Furthermore, in *head and neck squamous carcinoma* (HNSCC), activation of IGF-1R can overcome EGFR inhibition.[81] In *hepatocellular carcinoma* (HCC) it has been shown that simultaneous inhibition of IGF-1R and EGFR resulted in synergistic antineoplastic effects in hepatoma cell lines.[82-84] Upregulation of IGF-1R signalling has also recently been implicated in the development of resistance of breast cancer to therapy approaches such as radiotherapy, hormonal therapy and *human epidermal growth factor receptor 2* (HER2) targeting.[85,86] In breast cancer cell lines, the IGF-1R has also been shown to interact with and activate the HER2 receptor in cells resistant to anti-HER2 therapy (with Trastuzumab). This interaction could be disturbed by Lapatinib (a dual EGFR/HER2 TKI) as well as IGF-1R antibodies.[87] Similar findings have been made in NSCLC, where upregulation of IGF-IR signaling has previously been described to mediate acquired resistance to first-generation EGFR TKIs[88,89] as well as to the irreversible EGFR inhibitors PF299804 and WZ4002.[90] The data from these *in vitro* studies, together with data from *in vivo* studies,[80] successfully showed that simultaneous inhibition of EGFR and IGF-1R presents a promising combinatorial approach that could be of therapeutic relevance for a subset of NSCLC patients.

On the basis of these promising preclinical results, clinical studies with combinatorial inhibition were commissioned. However, these endeavors have unanimously failed. Ramallingam et al. tested Erlotinib and the IGF-1R inhibitor R1507 in patients with only one prior treatment regimen, but the combinatorial treatment failed to show any benefit.[91] As mentioned in 1.2.4, a trial investigating the effect of Figitumumab in combination with

Erlotinib as second line treatment was terminated in 2010 due to failing to reach the desired endpoint. Furthermore, a randomized phase II study of Erlotinib alone or in combination with the IGF-IR/insulin receptor TKI OSI-906, in patients with advanced EGFR-mutant NSCLC was terminated early after an interim analysis in March 2013, showing that there would be no benefit to the combination.[92]

The reasons why these studies failed might lie in the complexity of the TRK signaling network in general and especially in the context of cancer. With direct alterations of the involved molecules, changes in their expression and abundance, as well as evasion of inhibition by rerouting the signal along alternative pathways, tumors have many molecular mechanisms to become resistant to treatment. In addition, not only do the linear activations of signal transducers and their interplay factor into the decision-making processes and cellular behavior, but also the dynamics of these activations may play an important role in coding the signal. As such, even promising results in preclinical studies might lead to failures in later stages of development, until we are able to define the signaling networks involved on a more comprehensive scale in both space and time.

Consequently, I aim to investigate the activation and interactions of IGF-1R and EGFR signaling, concentrating on the dynamic behavior of the pathway players. Special emphasis is put on effect of aberrant signaling of IGF-1R and EGFR on the tumor cell dissemination, as the early spread is one of most important problems in lung cancer. To be able to comprehensively deal with the large amount of spatio-temporal data necessary to decipher cellular signaling in a reasonable resolution, I employ a systems biology approach.

1.3 Systems biology

Systems biology aims to describe highly complex biological systems with mathematical concepts and computational models. This system-level approach to biology has roots in classical physiology as far back as Weiner in 1948 and Bertalanffy in 1968.[93,94] Molecular biology began to apply these ideas and approaches with the mapping of the first regulatory circuits like the feedback inhibition of amino-acid biosynthetic pathways in 1957[95,96] and the definition of the lac operon and the elucidation of its regulation.[97] With the advent of the "-omics" age in biological research, the scale of systems-centered investigations became much larger. For example, in 2004, Westerhoff and Palsson argued that systems biology of that time was synonymous with genomics.[98] As other -omics and high throughput technologies caught up, the central challenge in systems biology moved towards integrating the different levels of cellular signaling from genomic changes to gene expression, protein

activation and metabolics. These efforts resulted in the generation of comprehensive network maps. Although these static "road maps" are important, to really understand the biology behind them, we need to know the "traffic patterns" in which these pathways are activated.[99] Thus, the current focus in the field is the investigation of the connectivity, crosstalk and dynamics of these networks. It has become apparent that temporal dynamics,[100,101] spatial distribution,[102,103] and cell-to-cell variability[104-106] are key systems properties that lead to context-specific cellular responses.

Cancer research is a prime candidate for the successful application of systems biology. It provides many examples of entities that, after first being thought of as dependent on a single aberration, display strong robustness against targeted treatment (thus representing complex systems to investigate). In contrast, there are only very few tumor entities whose pathology relies on a single molecular defect that can be efficiently managed by single agent treatments, e.g. a subset of chronic myeloid leukemia cases that respond to the TKI Imatinib.[107]

In order to answer biological questions, two distinct branches of computational systems biology have proven useful: (1) A top down approach, using data mining in large experimental datasets, to study emerging properties of the system, which would be missed using the traditional reductionist approaches. (2) A bottom up approach using simulation-based analysis of computational models of smaller scale systems. These models enable efficient generation and first testing of hypotheses, saving time and resources in elaborate *in vitro* and *in vivo* studies.[108,109]

Generation of ODE models

Key in the generation of useful mathematical models is choosing the right modeling approach for the observed level of complexity. If quantitative data is available and the system in focus is a relatively limited part of a signaling network, more detailed modeling of the chemical reactions involved becomes feasible. One of the established approaches to this more detailed modeling is the description of chemical reaction networks through *ordinary differential equations* (ODEs). Hereby, the rates of the reaction (i.e. association, dissociation, production and degradation of the individual molecular species) are represented through mass action kinetics[110] or the Michaelis-Menten approximations.[111] One big advantage of ODE models is the integration of quantitative and time-resolved data, thus allowing for interpretation and analysis of complex dynamic behavior on a molecular level. This can lead to nonintuitive insights into the observed biological systems, as for example shown by

Swameye et al. for the JAK-STAT pathway. They found that successive nucleocytoplasmic cycles, rather than unidirectional information flow from the cell surface to the nucleus followed by degradation of STATs, determines the systems activation state.[112]

The generation of a useful ODE pathway model is most successfully achieved by iterative processes between experimental data generation and computational model creation (as shown in Figure 8). After establishing the model topology (e.g. from literature and repositories like the KEGG database for pathway diagrams [113]) and supplying the parameters of the system by estimation or experimental data, the resulting model can either:

(1) fail to completely describe the experimental data. It can be rejected and different hypotheses must be developed and integrated into the ODE model. The new model is then again fitted. This process is iterated until one or more "candidate models" are identified, that can reproduce the data. If more than one model is determined, these can be ranked using model selection strategies[114] while experimental design strategies can help to generate additional data to increase differentiation between models.[115]

(2) completely explain the initial set of experimental data. This model can then be validated by experimentally testing model predictions. When enough confidence in the model is gained for it being indeed a sufficiently correct mathematical representation of the biological system, its behavior can be further investigated.[108]
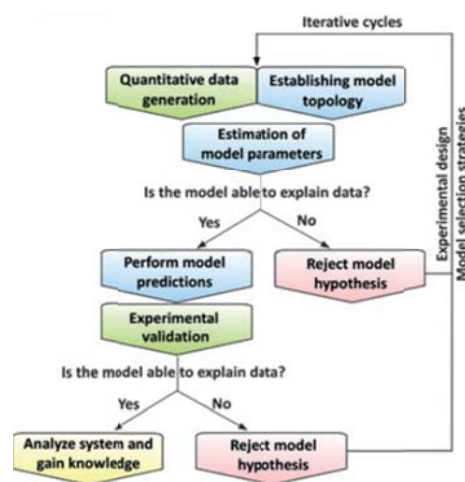
Figure 8: Workflow to establish an ODE model in iterative cycles between experimental validation and model refinement. Modified after Bachmann et al.[107]

2 Objectives

The evasion of TRK inhibition via rerouting of pro-tumorigenic signals along parallel signaling pathways is one of the central mechanisms in therapy resistance in NSCLC. While initially promising, clinical studies investigating combinatorial inhibition approaches targeting EGFR and IGF-1R ultimately failed to show benefit in patients, indicating the need for a better understanding of the molecular mechanisms and dynamics of these interactions.

The aim of my project is to investigate the role of the dynamic crosstalk between the signaling of EGFR and IGF-1R in NSCLC cells to better define the effects of pathway interaction. A special focus is put on the interaction and crosstalk of downstream signaling from both receptors and the effects on growth and migration of NSCLC cells to engage the problem of early spread. To this end, the following goals were pursued:

1. Establishing novel evaluation methods for quantitative time resolved 2D and 3D migration/invasion assays, followed by proof of principle investigations.
2. Generation of quantitative time resolved data of EGF/IGF-1 pathway activation in NSCLC cells for the generation of an ODE pathway model.
3. Application of the newly established phenotypical evaluation methods on the effects of EGF/IGF-1 stimulation and inhibition on NSCLC cells.
4. Definition of downstream pathway effectors that might facilitate the observed phenotypical effects on NSCLC cells.

3 Materials & Methods

3.1 Materials

3.1.1 Cell lines

The cell lines used have been obtained from the American Type Culture Collection (ATCC)/LGC Standards (Wesel).

Table 1: NSCLC cell lines

Trait	H838	H1975	Calu-1
classification	NSCLC (ADC)	NSCLC (ADC)	NSCLC (SCLC)
gender	male	male	male
smoking status	N/A	smoker	N/A
age [years]	59	27	47
cultivation medium	DMEM	DMEM	MEM + NEAS

3.1.2 Media and additives for cell culture

Table 2: Cell culture media and additives

Substance	Company
DMEM	Lonza, Walkersville, MD, USA
Geneticin (G418)	Gibco, Life Technologies, Darmstadt, Germany
L-Glutamine	Gibco, Life Technologies
MEM	PAA Laboratories, Cölbe, Germany
OptiMEM	Gibco, Life Technologies
Penicillin/Streptomycin	PAA Laboratories
Puromycin	Sigma, Hamburg, Germany

3.1.3 Consumables, solutions and reagents

Table 3: Consumables, solutions and reagents

Substance	Company
Absolute qPCR SYBR Green ROX Mix	Thermo Scientific, Offenbach, Germany
Acutase	Sigma, Hamburg
Bradford Reagent	Sigma,Munich, Germany
BSA	Sigma, Hamburg
Cell culture plates	TPP, Trasadingen, Switzerland
Imaging plates	Zell-kontakt, Nörten-Hardenberg, Germany
Cell lysis buffer (10x)	Cell Signaling, New England Biolabs, Frankfurt/Main, Germany
dNTP Mix	Thermo Scientific
Earl's Salt solution (EBBS)	Sigma, Hamburg
EZ-RUN-Pre stained Rec	Thermo Scientific

Prot ladder, BP 3603-500	
FuGENE HD Transfection Reagent	Promega, Madison, USA
IBIDI inserts	IBIDI, Martinsried, Germany
Methocel	Sigma, Hamburg
Nitrocellulose membranes	Whatman, Dassel, Germany
NucBlue Live ReadyProbes	Life Technologies, Darmstadt, Germany
Oligofectamine Reagent	Invitrogen, Life Technologies, Darmstadt, Germany
Protease-Inhibitor-Mix	Serva Electrophoresis, Heidelberg, Germany
PureCol bovine collagen I	AdvancedBioMatrix, Carlsbad, CA, USA
RevertAid^{TM} H Minus M-MuLV	Thermo Scientific
Trypsin	PAA Laboratories

3.1.4 Oligonucleotides

Oligonucelotides (siRNAs)

Scrambled siRNA was obtained from Eurofins MWG (Ebersberg, Germany)

Table 4: Oligonucleotides for RNA interference

siRNA	*Company*
FIR	Stealth RNAi, HSS 146065, Invitrogen, Life Technologies
scrambled	UGGUUUACAUGUCGACUAA-dTdT (-)

Oligonucleotides (primers)

Primers for qRT-PCR were obtained from ThermoFisher Scientific with the following sequences:

Table 5: qRT-PCR primers

Primer	Forward	Reverse
AREG	5'-CGGTGGTGCTGTCGCTCTTG-3'	5'-GAGTAGGTGTCATTGAGGTCC-3'
B2M	5'-CACGTCATCCAGCAGAGAAT-3'	5'-TGCTGCTTACATGTCTCGAT-3'
CCL2	5'-CTTAGCTTCCAGAGACGGTGAC-3'	5'-CTTTTAGACTCTGAATAGGC-3'
CTGF	5'-CCAAGGACCAAACCGTGG-3'	5'-CTGCAGGAGGCGTTGTCAT-3'
IL8	5'-GCTCTCTTGGCAGCCTTCCTG-3'	5'-GTTCTTTAGCACTCCTTGGC-3'

3.1.5 Antibodies

Primary antibodies, and dilutions used for Western immunoblotting:

Table 6: Primary antibodies for Western immunoblotting

Antibody	Species	Dilution	Company
anti-Actin	Mouse	1:10,000	MP Biomedicals, Santa Ana, CA, USA
anti-AKT	Rabbit	1:500	Cell Signaling, New England Biolabs
anti-pAKT	Rabbit	1:500	Cell Signaling, New England Biolabs
anti-EGFR	Rabbit	1:500	Cell Signaling, New England Biolabs
anti-pEGFR Tyr 1066	Rabbit	1:500	Cell Signaling, New England Biolabs
anti-ERK	Rabbit	1:500	Cell Signaling, New England Biolabs
anti-pERK	Rabbit	1:500	Cell Signaling, New England Biolabs
anti-IGF-1R	Rabbit	1:200	Santa Cruz, Heidelberg, Germany
anti-pIGF-1R Tyr1165/1166	Rabbit	1:200	Santa Cruz
anti-Puf60 (FIR)	Goat	1:500	Abcam, Cambridge, UK

Secondary antibodies and dilutions used for Western immunoblotting:

Table 7: Secondary antibodies for Western immunoblotting

Antibody	Species	Dilution	Company
IRDye 680LT anti-mouseIgG	Donkey	1:20000	LiCor Bioscience
IRDye 800CW anti-goat IgG	Donkey	1:10000	LiCor Bioscience
IRDye 800CW anti-rabbit IgG	Donkey	1:10000	LiCor Bioscience

Antibodies for FACS analysis:

Table 8: Antibodies for FACS analysis

Antibody	Species	Company
Anti-IGF-1R - PE	mouse	Antibodies-online.com
Anti-EGFR - FITC	rat	Abcam, Cambridge, UK

3.1.6 Tyrosine kinase inhibitors

Table 9: Tyrosine kinase inhibitors

Substance	Specificity	Company
Picropodophyllin	IGF-1R	Merck Millipore, Darmstadt, Germany
CAS-879127-07-8	EGFR	Merck Millipore, Darmstadt, Germany
Erlotinib	EGFR	Cayman Chemical, Ann Arbor, Mi, USA
Afatinib	EGFR	LC Laboratories, Woburn, MA, USA

3.1.7 Buffers and solutions

Buffers and solutions were prepared with deionized water.

Buffers used for Tris/Glycin-SDS-PAGE

Laemmli-buffer (3x): 50 ml

20% SDS	15 ml
β-Mercaptoethanol	7.5 ml
95.5% Glycerine	15 ml
1M Tris-HCl (pH 7.6)	9.375 ml
H20	3.125 ml
+Bromophenol blue	

Borate buffer

Borate acid	450 nM
EDTA	20 nM
adjust to pH 8.8 with NaOH	

TBS (10x)

Tris-HCl (pH 7.6)	200 mM
NaCl	1.5 M

TBST

10x TBS	10% (v/v)
Tween-20	0.1% (v/v)

Gel electrophoresis buffer

SDS	0.01% [w/v]
Glycine	190 mM
Tris-HCl	25 mM

Nicoletti-Buffer for FACS analysis

Propidiumiodide   50 mg/ml (0.05%)
Sodiumcitrate   0.1% (w/v)
Triton X-100   0.1% (v/v)

Collagen solution

Collagen I   900 µl
H2O   360 µl
EBBS   140 µl
NaOH (1 M)   ~15 µl, until the color changes to red/pink

3.1.8 SDS/PAGE Gels

Composition of separation and collection gel for SDS/PAGE gel electrophoresis for preparation of 10 ml, respectively are given in the table below.

Table 10: Composition of collection and separation gels for SDS/PAGE

substance	8% separation gel	10% separation gel	12% separation gel	collection gel
Acrylamide	8% [v/v]	10% [v/v]	12% [v/v]	5% [v/v]
Tris-HCl, pH 6.8				0.5 mM
Tris-HCl, pH 8.8	375 mM	375 mM	375 mM	
10% (w/v) SDS	0.1% [w/v]	0.1% [w/v]	0.1% [w/v]	0.1% [w/v]
10% APS	0.1% [v/v]	0.1% [v/v]	0.1% [w/v]	0.1% [w/v]
TEMED	0.04% [v/v]	0.05% [v/v]	0.06% [w/v]	0.1% [w/v]
deion. Aqua	ad 10 ml	ad 10 ml	ad 10 ml	ad 10 ml

3.1.9 Chemicals

In general, chemicals were used in p.A. quality and purchased from the following companies except where otherwise specified.

- Sigma Aldrich Chemikalien GmbH (Deisenhofen, Germany)
- Carl Roth GmbH u. Co. KG (Karlsruhe, Germany)
- Biomol GmbH (Hamburg, Germany)
- Invitrogen GmbH (Karlsruhe, Germany)
- Merck KGaA u. Co. KG (Darmstadt, Germany)
- Roche Boehringer GmbH (Mannheim, Germany)
- GE-Healthcare Medical Systems, GmbH u. Co. KG (Munich, Germany)

3.1.10 Kits

- Microarray: GeneChip Human Gene 2.0 ST Array (Affymetrix, Santa Clara, CA; USA)
- NucleoSpin RNA II kit (Macherey-Nagel, Düren, Germany)
- ELISA kits (R&D Systems, Minneapolis, MN, USA):
  - o EGF (DEG00)
  - o IGF-1 (DG100)
- CellTox^{TM} Green cytotoxicity assay (Promega)
- CellTiter-Blue$^®$ cell viability assay (Promega)

3.2 Equipment

Table 11: Equipment

equipment	name	company
Agarosegel electrophoresis systems		Keutz Reiskirchen, Germany
PAA-Agarosegel electrophoresis systems		Biozym, Oldendorf, Germany
Cell counting chamber	Neubauer counting chamber	Brand, Frankfurt am Main, Germany
Cell culture hood	BioWizard Silverline	Kojair Tech OY, Vilppula, Finnland
Centrifuges	Mikro 200R	Hettich, Tuttlingen, Germany
	Centrifuge 5415R	Eppendorf, Hamburg, Germany
	Megafuge 16R	Thermo Scientific, St. Leon Rot, Germany
CO_2 incubator	Hera Cell 150	Thermo Scientific, St. Leon Rot, Germany
	INCOmed	Memmert, Schwabach, Germany
Live cell imaging unit	Olympus IX81 photomicroscope	Olympus, Hamburg, Germany
CCD camera	Hamamatsu ORCA-R2	Hamamatsu Photonics Deutschland GmbH, Hersching, Germany
Microscope	Axiovert 25	Zeiss, Oberkochen, Germany
FACS	FACS-Calibur flow cytometer	Becton-Dickinson, Heidelberg, Germany
Fume hood	Secuflow	Waldner, Wangen, Germany
Gel casting chamber		BioRad, Munich, Germany

Microfuge	Micro 200	HettichZentrifugen, Tuttlingen, Germany
Microplatereader	FLUOstar Omega	BMG Labtech, Ortenberg, Germany
	MultiSkan Ascent	Thermo Scientific, St. Leon Rot, Germany
Microwave		Panasonic, Hamburg, Germany
Orbital shaker	Biometra WT17	Biometra, Göttingen, Germany
PCR	DNA Engine PTC 200	BioRad, Munich, Germany
	Multi Cycler PTC	Biozym, Oldendorf, Germany
Photometer		Eppendorf, Hamburg
pH-Meter	pH 210 Microprocessor	Hanna Instruments (Kehl am Rhein)
Power supply	EV 231	Consort, Turnhout, Belgium
qRT-PCR Thermocycler	StepOnePlus	Applied Biosystems, Darmstadt, Germany
Rolling shaker	CAT RM5	NeoLab, Heidelberg, Germany
Running chamber	Mini PROTEAN Tetra Cell	BioRad, Munich, Germany
Spectrometer	NanoDrop® ND-1000	Thermo Scientific, St. Leon Rot, Germany
Thermoblock	Thermomixer compact	Eppendorf, Hamburg, Germany
Transfer chamber	Mini PROTEAN Tetra Mini Trans Blot Module	BioRad, Munich, Germany
Western blot imaging system	Odysee Sa Infrared Imaging System	LI-COR Bioscience, Bad Homburg, Germany

3.3 Software

FIJI (ImageJ v1.46j), (http://fiji.sc/Fiji)

Photoshop CS5, (Adobe Systems GmbH, Munich, Germany)

Image Studio v3.1.4 (LiCor Biosciences,Bad Homburg, Germany)

StepOne software v2.3 life technologies (Applied Biosystems, Darmstadt, Germany)

SAS JMP7 Genomics, version 4 (SAS Institute, Cary, NC, USA)

3.4 Methods

3.4.1 Cultivation of cells

Adherent growing cells were cultivated on 15 cm dishes in a humid atmosphere containing 5% CO_2 at a temperature of 37°C. H838 and H1975 cells were cultivated with DMEM, supplemented with 10% *fetal calf serum* (FCS) and 1% penicillin/streptomycin. Calu-1 cells were cultivated in MEM medium, supplemented with 10% FCS and 1% penicillin/streptomycin as well as 1% NEAS and 1% sodium pyruvate.

3.4.2 Starvation for growth factor treatment

In order to decrease background activation of pathways by FCS, cells were starved in propagation medium without FCS, but supplemented with 1% of BSA. To this end, the propagation medium was aspirated and the cells were washed at least twice with PBS. Subsequently, starvation medium was added and the cells were starved overnight.

3.4.3 Cryo conservation

Cells from a sub-confluent 10 cm plate were trypsinated, centrifuged at 1,000 rpm for 5 min at 4°C and resuspended in 1 ml medium containing 10% DMSO. The cells were carefully cooled down over night at -20 °C and finally frozen at -80°C for 24 h and stored in the gaseous phase of nitrogen for long-time storage. Cells were thawed in a water bath at 37°C, resuspended in 10 ml of corresponding medium and centrifuged at 1000 rpm for 5 min at RT to eliminate the DMSO. Cells were again resuspended in 8 ml of corresponding medium und transferred to a 10 cm plate. Twenty-four hours after thawing the medium was exchanged again.

3.4.4 Cell line characterization

For the molecular characterization of the different cell lines, H838 and H1975 cells of a confluent 10 cm dish each were trypsinated and pelleted by centrifuging at 1,000 rpm. The cells were characterized for a panel of mutations and differentiation markers, which are frequently found in human NSCLC. These analyses were performed in the Molecular Diagnostics Facility of the iPH.

ALK translocation, overexpression of c-MET, and EGFR were tested using FISH analysis. Sequencing was employed to check for mutations in EGFR (exons 18, 19, 20, 21), K-Ras (exons 2 and 3), B-Raf (exon 15) PIK3CA (exons 1, 5, 7, 9, 20), and PTEN (exons 1-9). The degree of dedifferentiation was assessed with immunohistological staining against cytokeratins (CK) 5/6, CK7, *transcription intermediary factor 1-alpha* (TIF) and p63.

3.4.5 Seeding cells

Cells were trypsinated, centrifuged at 1000 rpm for 5 min at RT, and resuspended in the corresponding media. The cells were counted using a Neubauer chamber and seeded with different cell numbers per dish/well for each experiment:

Table 12: Seeding concentrations for different experiment and cell culture dishes

Assay Cell line	Protein Kinetics 10cm dish	Transfection 10 cm dish	RNA extraction 6-well	12-well for ELISA assays	24-well IBIDI migration assay	96 well cell viability and cell death assays
H838	1×10^6			5×10^5	20,000 / side	5,000
H1975	1×10^6		1.5×10^5	5×10^5	20,000 / side	5,000
Calu-1		8.5×10^5			20,000 / side	5,000

3.4.6 FACS

Cells of 10 cm dishes at ~70% confluence were detached using Accutase according to the manufacturer's protocol and further processed for FACS staining in the Cytometry Facility of the iPH. Staining was performed against IGF-1R with an anti-IGF-1R antibody labeled with phycoerythrine (PE) and against EGFR with an anti-EGFR antibody labeled with FITC (see Table 8). For both stains, 10 µl of the undiluted antibody were added to 1×10^6 cells in 100 µl.

Furthermore, cell cycle distribution was assessed by DAPI staining. Multiparametric analysis was performed on a Galaxy Pro Flow Cytometer (PARTEC, Münster, Germany) by stimulating the fluorochromes DAPI with a mercury 100 W vapour lamp, FITC with a 488 nm air-cooled argon laser and measuring the fluorescence intensities at 530/30 nm, and PE at 570/20 nm. EGF-FITC and IGF-PE were measured in the logarithmic mode, DAPI stained DNA was measured in linear mode [116]. For each measurement, 5,000 to 10,000 cells were analyzed. Calculation of the cut off (negative vs. positive cells) was performed with the Flowmax program (PARTEC, Münster, Germany) and results from isotype controls for FITC and PE multiparametric acquisition and analyses. Cell cycle analysis and DNA-index were calculated using the MultiCycle AV program (Phoenix flow systems, San Diego, CA 92121).

3.4.7 Ligand secretion

H838 and H1975 cells were seeded in 12-well plates in triplicates as detailed in 3.4.5 and allowed to attach overnight. After starvation (see 3.4.2), the cells were supplied with fresh DMEM medium without FCS and incubated for up to 24 h. Supernatant was collected after 0, 6, 12, and 24 h and the concentrations of EGF and IGF-1 were assessed using ELISA.

3.4.8 Ligand depletion

H838 and H1975 cells were seeded in 12-well plates in triplicates as detailed in 3.4.5 and allowed to attach overnight. After starving overnight in DMEM without FCS, media containing 500 pg/ml EGF or 5 ng/ml IGF-1, respectively, were added with 1 ml/well. At 0, 30, 60, 90, 120, 180, and 240 min after stimulation, cells were placed on ice and medium was taken off and frozen at -20°C. An aliquot of stimulation medium was frozen as a control. For cytokine analysis, the supernatants were thawed and the ligand concentration was measured *via* ELISA.

3.4.9 ELISA

ELISA assays for IGF-1 and EGF were performed according to the manufacturer´s protocol.

3.4.10 Transfection of siRNAs

As detailed in 3.4.5., twenty-four hours after seeding, siRNA-transfections were performed using Oligofectamine according to the manufacturer´s instructions. siRNAs were used at a final concentration of 50 nM. After letting the cells attach overnight, they were washed with 2 ml OptiMEM and then supplied with 4.8 ml OptiMEM. For each siRNA condition, a solution of 1,080 µl OptiMEM with 12 µl of the respective siRNA (solution A), and, separately, 90 µl OptiMEM with 18 µl Oligofectamin (solution B), were mixed. After incubating for 8 min at

RT, solution A and solution B were mixed and again incubated for a further 20 min at RT. Subsequently, the transfection mix was dripped onto the cells. Untreated control cells were supplemented with just 6 ml OptiMEM. To ensure thorough distribution, dishes were carefully mixed in circular motions. After further incubation for 4 h in the incubator, 6 ml of the normal propagation medium was added to the cells. Medium was changed again on the next day.

3.4.11 Growth factor stimulation for protein extraction

H838 and H1975 cells were seeded in 10 cm dishes as described in 3.4.5. After cultivation for three days, cells were washed three times and starved overnight. The following day, cells were stimulated with different concentrations of IGF-1 and/or EGF diluted in starvation medium.

Dose-response tests and time-resolved kinetics using different cytokine concentrations and time points are detailed in the table below. At the respective time points, cells were lysed as described in 3.4.13.

Table 13: Concentrations and time points for dose-response and time course kinetics experiments

	Concentrations [ng/ml]	Time points [min]
Dose-response	0,1, 2,5, 10, 50	10
Kinetics	50	0, 5, 10, 15, 20, 30, 60, 120, 240, 320

3.4.12 Receptor inhibition for phenotypical assays

For the measurement of lateral migration, cells were seeded in 24 well plates with IBIDI inserts or 96 well plates with full medium as described in 3.4.5. After letting the cells attach overnight, medium was renewed and supplemented with the relevant inhibitor concentrations.

3.4.13 Isolation of protein lysates

Cells were washed twice with ice-cold PBS and harvested in cell-lysis buffer supplemented with a protease inhibitor cocktail. Cell lysates were collected in reaction tubes, immediately frozen in liquid nitrogen and stored at -20°C until further preparation. For isolation of total proteins lysates, tubes were centrifuged for 10 min at 4°C with 10,000 rpm. The supernatants were transferred into new tubes and the pellets were discarded.

3.4.14 Determination of total protein concentration

Total protein concentration was determined using the Bradford assay. To this end, 1.25 µl lysate was mixed with 625 µl Bradford reagent in a cuvette. Optical density was measured at 595 nm using a photometer. In parallel, a standard curve using defined concentration (0.2, 0.4, 0.6, 0.8, and 1 µg/ml) of BSA was measured for calibration. Total protein concentrations of the lysates were calculated with respect to the standard curve.

3.4.15 SDS-PAGE and immunoblotting

Equivalent aliquots of whole protein lysates (50 µg) were adjusted with PBS and 3xLaemmi buffer to a final volume of 30 µl to be separated by SDS/PAGE gel electrophoresis. For this study, 8%, 10%, and 12% separation gels were prepared as described in Table 10, using a gel casting chamber from BioRad. After denaturation of proteins at 95°C for 5 min, samples and protein-size marker were loaded onto the gels and separated with a voltage of 70 V for 15 min followed by 1.5 h to 2 h of 120 V in running buffer (see 3.1.7). Separated proteins were transferred to nitrocellulose membranes using Mini PROTEAN blot modules from BioRad with ice-cold borate buffer (see 3.1.7) at a voltage of 100 V for 90 min.

After blocking of unspecific bindings with blocking solution containing 5% skim milk in TBST for 1 h at RT, membranes were incubated with primary antibodies (Table 6) diluted in blocking solution overnight at 4°C. Membranes were washed three times with TBST for 10 min and incubated with the respective secondary antibodies coupled with a fluorochrome (Table 7) diluted in blocking solution for 1h at RT. Membranes were again washed three times with TBST for 10 min. All incubations were performed in plastic trays on an orbital shaker or in 50 ml Falcon tubes on a roll shaker. After the final washing step, detection was performed using an Odysee Sa Imaging System. The molecular weight of the proteins was determined using the protein marker and equal loading of protein samples was confirmed *via* β-actin detection. Quantification of the detected bands was performed using the Odysee Image Studio software.

Randomizing samples to minimize blotting effects

Figure 9 shows the randomization approach employed for the semi-quantitative Western immunoblot analysis of proteins. In order to allow comparability between different treatments, samples were distributed so that all treatments from one time point were measured on one gel. Additionally, to avoid position effects, samples were randomized according to Schilling et al. (Figure 9 A).[117] Western immunoblot bands were quantified using the Odysee SA system. In order to increase the data space and thus the confidence in the estimated mean, additional data points were estimated by linear interpolation between two measured values (Figure 9 B). The estimated mean was computed by minimizing the equation given in Figure 9 B.

$$RSS = \sum_{i,j,k} (S_{ijk} - y_{ik}/s_j)^2$$
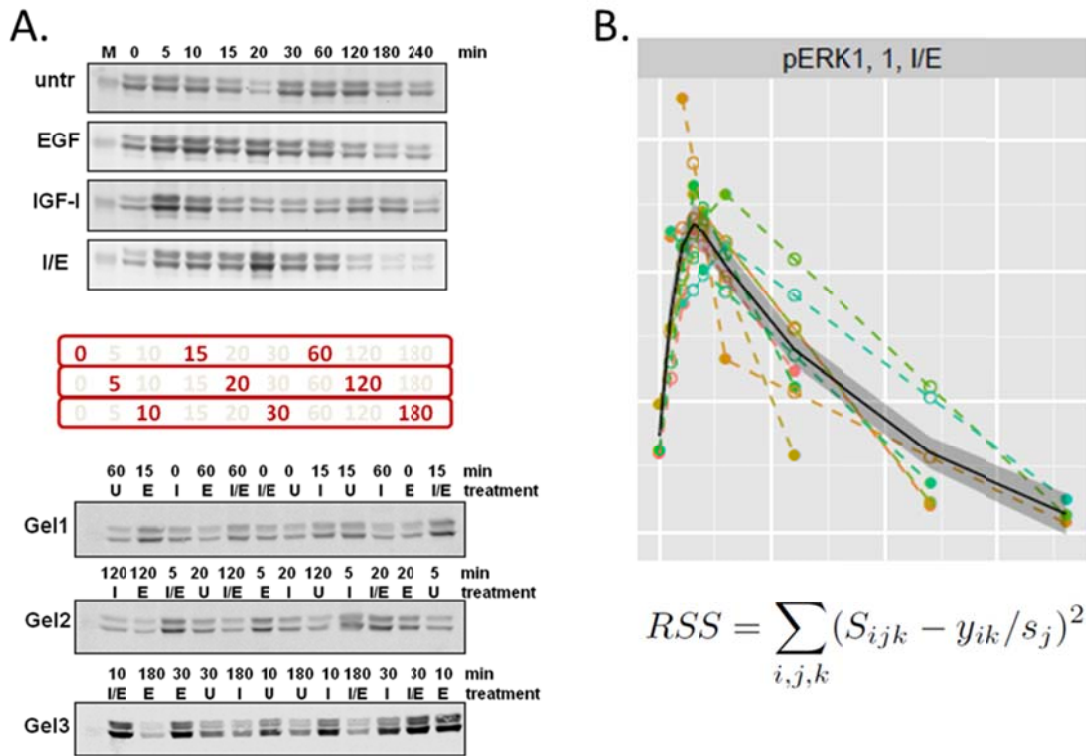
Figure 9: Randomization of Western immunoblot data, estimation of mean signal intensity and augmentation of trajectories *via* linear interpolation between measured time points. A. Example of randomization layout. Top: Western blots with linear loading of samples. Middle: distribution of time points for the randomization. Three time points from each treatment, marked in red, are combined on one gel. Bottom: Western blots with randomized layout. B. Top: example of augmented trajectories from quantified Western immunoblot data. Filled circles represent measured data points, empty circles are results of linear interpolation between two real data points. The mean is depicted by the black line. The grey band around the mean denotes the standard error of the mean estimation. Bottom: Equation to estimate mean signal intensity with measured data point *S*, estimated mean *y* and scaling factor *s* over all time points *i*, gels *j*, and experimental conditions *k*. This equation is minimized to estimate the mean.

3.4.16 ODE pathway model generation

For mathematical modeling the Data2Dynamics-Software was used.[118] The ODE system underlying the model was generated with mass-action kinetics. To generate model simulations, the ODE system was solved by a parallelized implementation of the CVODES algorithm.[119] The model parameters were estimated by maximum likelihood estimation applying the MATLAB lsqnonlin algorithm. The parameter name prefix "init" indicates the initial value of a dynamic variable. In order to evaluate the identifiability of the model parameters and to assess confidence intervals, the profile likelihood was calculated.[120] Computational modeling was perfomed by Dr. C. Maus in the group of Prof. T. Höfer (Bioquant, Heidelberg).

3.4.17 Growth factor stimulation for RNA extraction

H1975 cells were seeded in 6 well dishes as described in 3.4.5. After cultivation for 3 days, cells were washed 3 times and starved overnight. The following day, cells were stimulated with 50 ng/ml of IGF-1 or EGF diluted in starvation medium. Samples were harvested at 0, 0.5, 1, 2, 4, 6, 8, 12, 24, and 48 h. Subsequently RNA was extracted as described in 3.4.18.

3.4.18 Total RNA isolation, cDNA synthesis, and semi-quantitative real-time polymerase chain reaction (qRT-PCR)

Total cellular RNA was isolated with the NucleoSpin RNA II kit according to the manufacturers' instructions. RNA concentrations were determined by measuring the absorbance (230 – 400 nm) using a NanoDrop® ND-1000 spectrometer. The purity of the RNA was determined through the quotient Abs. 260 nm/Abs. 280 nm. RNA with a quotient ≥ 1.8 was used for further analysis.

For semi-quantitative real-time PCR analysis, 1 µg total RNA was reversely transcribed. cDNA was amplified using 0.8 mM dNTPs and 200 ng/µl Poly-dT primers on a Multi Cycler PTC with the following cycling program:

cDNAsynthesis

temperature [°C]	time
70	5 min
95	5 min
42	60 min
70	10 min

RevertAidTM H minusM MuLV(1 U/µl) was added after the second step (25°C, 5 min).

qRT-PCR reactions were performed on the StepOnePlus thermocycler. To this end, samples were analyzed in triplicates using cDNAs corresponding to 2.5 ng of RNA, 1 µM of corresponding primers, 50% [v/v] Absolute qPCR SYBR Green ROX Mix and following cycling program:

qRT-PCR	
temperature [°C]	time
50	2 min
95	15 min
95	15 s
60	1 min

40x

The SYBR Green fluorescence signal is directly proportional to the amount of synthesized cDNA. To control for unspecific primer binding and primer dimers, a melting curve analysis was performed after amplification, using the following program:

Melting curve	
temperature [°C]	time
95	15 s
60	30 s
95-60°C	-0,5°C/5 s
95	15 s

First, cDNA dilution series (1:12.5, 1:25, 1:50, 1:100, 1:200 und 1:400) of all primer pairs were used to generate standard curves. These were then used to generate relative gene expression numbers, from the Ct-values of the investigated samples. The relative gene expression was then normalized to the relative expression of the housekeeping gene *beta-2 microglobulin* (B2M).

3.4.19 Microarray analysis with the GeneChip Human Gene 2.0 ST Array

Total RNA was extracted as detailed in 3.4.18 for each time point in triplicates. Microarray analysis was performed using Affimetrix GeneChip Human Gene 2.0 ST Arrays in collaboration with the Group of Prof. N. Gretz at the Center for Medical Research in Mannheim (ZMF Mannheim). To this end, all triplicates were used for the 0 h, 24 h, and 48 h time points, whereas only one of the triplicates was used for the other time points. Quality assessment was performed with the Agilent Bioanalyzer. After amplification and reverese transcription, labelling with biotin and fragmentation of the resultant cDNA, hybridization (i.e. the loading of the array with the labeled cDNA fragments) was performed for 16 h at 45 °C. Due to the number of samples, three separate arrays had to be used and the samples were distributed in three hybridization batches as shown in Table 14. Subsequently, washing and staining was performed using an Affymetrix Fluidics Station 450 and the microarray was scanned using an Affymetrix GeneArray Scanner 3,000.

Table 14: Distribution of microarray samples over three hybridization batches. A, B and C stand for the respective hybridization batch. For 0 h and both 24 h and 48 h, triplicates were measured. For all other time points, single samples were used.

Replicas Time [h]	Control A	Control B	Control C	IGF-1 A	IGF-1 B	IGF-1 C	EGF A	EGF B	EGF C
0	1	1	1						
0.5		2				2			3
1	2					2	3		
2	2					2			3
4			2			2	3		
6		2				2	3		
8						2	3		
12		2				2		3	
18						2		3	
24	2	2	2	2	2	2	3	3	3
48	2	2	2	3	3	3	3	3	3

Data preprocessing and *Gene Ontology* (GO) annotation was then performed by the group of Dr. F. Matthäus (IWR Heidelberg). For data preprocessing, the SCAN method was used as described by Piccolo et al.[121] in order to control for probe composition (e.g. GC content) and batch effects. The big advantage of SCAN lies in the independence from external reference samples. Comparative *Principal Component Analysis* (PCA) of SCAN to other methods by Marco Albrecht revealed than preprocessing with SCAN lead to a useful temporal resolution of the time course data (Figure 10).
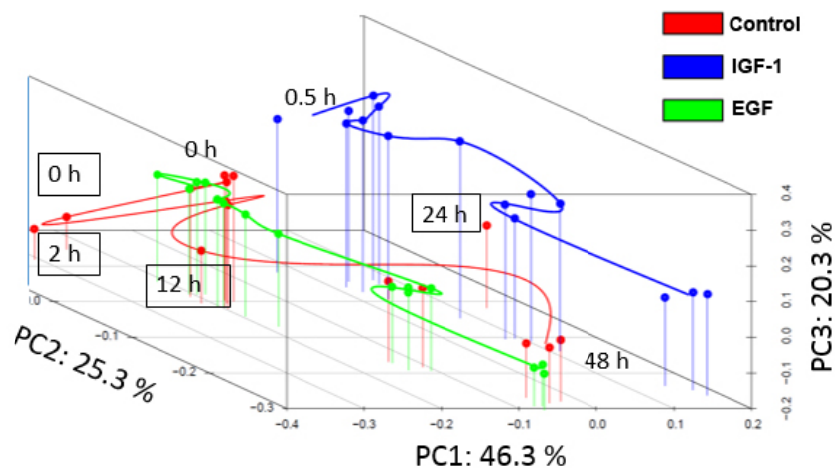
Figure 10: PCA of the datasets from EGF (green) and IGF-1 (blue) as well as the unstimulated control (red) after SCAN preprocessing. Time points in frames denote outliers. Image kindly provided by Dr. F. Matthäus.

The PCA also revealed that at 0 h and 24 h, one of each of the triplicates was determined to be an outlier and was eliminated from the analysis. Also, the data points for 2 h, 12 h, and 24 h were determined to be outliers and eliminated as well. In order to deal with the low replication and temporal dynamics of the dataset, a new method was developed for GO annotation and analysis of differential expression. Hereby, scores for the dynamic expression, peak expression, integral under the curve and relevance (as determined from numbers of publications) are weighted and combined into a consensus score.

3.4.20 Multiplex analysis of cell death and cell viability

In order to determine cell viability and cell death, the CellTox™ Glow cytotoxicity assay was multiplexed with the CellTiter-Blue ® cell viability assay. To this end, cells were seeded in 96 well plates (see Table 12) and cytotoxicity as well as cell viability were determined at indicated time points. First, CellTox™ Glow solution was prepared according to the manufacturers' instructions and used in a 1:5 dilution in each well. After incubation for 15 min, the amount of dead cells was quantified in the FLUOSTAR Omega microplate reader using the filter combination excitation: 485 nm / emission: 520 nm. Subsequently, CellTiter-Blue ® solution was prepared according to the manufacturers' protocol and employed in a 1:5 dilution in the wells of the same plate. After incubation for 1 h, metabolic activity was measured in the FLUOSTAR Omega microplate reader using the filter combination excitation: 540 nm / emission: 610 nm. For absolute quantification, a standard curve was prepared on a 96-well plate with cell numbers ranging from 1,000 to 10,000 cells in five technical replicates.

In contrast to the procedure with the test plates, the standard plate was first tested for viability and subsequently for cell death: After letting the cells attach over night, they were first treated with Cell Titer Blue to measure cell viability as described above. Thereafter, the cells were lysed with the lysis buffer supplied in the CellTox[TM] Green kit and then treated as described above to measure total cell number. Cell numbers and amount of dead cells were subsequently calculated with respect to the standard curve.

3.4.21 2D Migration assay with IBIDI inserts

For 2D migration assays, cells were seeded in IBIDI inserts in a 24-well plate (with concentrations of 2×10^4 cells in each chamber of the insert, see 3.4.5) and left to attach overnight in the incubator. The inserts were carefully peeled off, resulting in a gap of 500 µm between the populations. The wells were then washed once with PBS to clear away detached cells, and subsequently filled with 500 µl of the respective treatment medium. For growth factor stimulation experiments, medium was carefully aspirated from the inserts and replaced with starvation medium in the inserts after washing twice with starvation medium for overnight starvation before continuing as described above. Cell nuclei were stained with NucBlue Live ReadyProbes by adding one drop / 500 µl medium.

3.4.22 3D Spheroid migration/invasion assay

Spheroids were generated with 500 cells per spheroid using a hanging drop approach as follows:
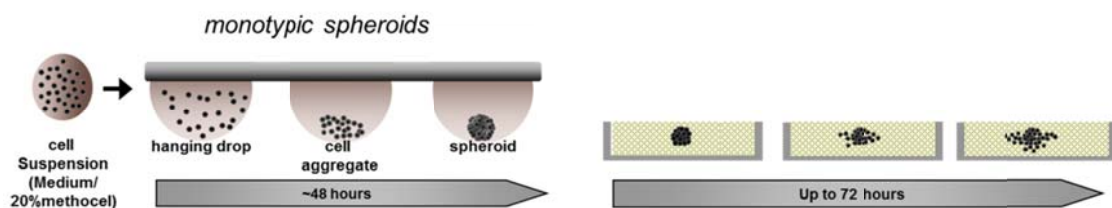
Figure 11: Generation of spheroids with the hanging drop method. 20 µl drops of cell suspension were pipetted on the lid of a cell culture dish. The lid was inverted and cells aggregate in the tip of the hanging drop. Over 48 h the cells increase cohesion and form compact spheroids. These spheroids were then embedded in a matrix and monitored over up to 72 h.

Cells were first trypsinized, counted and then centrifuged and resuspended in propagation medium with 20% of a 12 mg/ml solution of methocel in basal medium to the desired concentration. Unless otherwise specified, this was 2500 cells/ml, resulting in 500 cells per drop of 20 µl of this cell suspension. Drops were pipetted on the lid of a 150 cm²-culture dish, which was subsequently carefully inverted back onto the dish. In this approach, all suspended cells in the resulting hanging drop contribute to the formation of a single

spheroid as illustrated in Figure 11. To prevent excessive evaporation, the dish bottom was filled with 15 ml of PBS. After 48 h, the spheroids were harvested by carefully washing them off the culture dish lids and collecting them in a 5 ml Eppendorf tube. After letting the spheroids sediment for 10 min and taking off the supernatant, spheroids were embedded in 400 µl of a 1:1 mix of 1 mg/ml collagen I solution and methocel-solution. To this end, 24-well imaging plates were pre-coated with 200 µl of collagen I/methocel solution that were then allowed to polymerize for 30 min. The sedimented spheroids were taken up in collagen I/methocel solution to a final concentration of 30 spheroids per 200 µl and then distributed into the wells with 200 µl per well. After polymerization in the incubator for 30 min, the embedded spheroids were supplied with 500 µl of full propagation medium containing the relevant stimulation agents.

3.4.23 Manual evaluation of 3D spheroid migration/invasion

For manual evaluation of 3D spheroid migration/invasion, bright field images were acquired on an IX81 motorized inverted microscope and a Hamamatsu ORCA-R2 camera with the Olympus excellence RT software. Further image processing and evaluation was carried out using FIJI. The size of the spheroid body was assessed by measuring the projection area. Sprouting activity was assessed by counting the sprouts and summing up their measured length.

3.4.24 Live cell imaging data acquisition for migration and invasion analyses

Live cell imaging was conducted using an Olympus Cell^R Live Cell Imaging System with an IX81 motorized inverted microscope and a Hamamatsu ORCA-R2 camera, fitted with a climate chamber. Images were acquired using the Olympus excellence RT software. Further image processing was carried out using FIJI and computational approaches detailed below.

2D migration analysis

For the analysis of 2D migration assays, images were acquired over a period of up to 72 h using the excellence RT software, with 4x magnification in both phase contrast and at 460 nm channels in intervals of 90 min between pictures. Each gap was covered by a vertical line of 5 pictures with an overlap of ~20%. Image stacks were stitched using the "stitch grid of images" plugin in FIJI, with automated computation of image overlap (Figure 12A). The stitched image stacks were then further analyzed together with the group of Dr. F. Matthäus (IWR Heidelberg).

Here, the time-lapse videos were analyzed by particle image velocimetry (PIV)[122] using a Matlab implementation (MatPIV).[123] The method is based on defining a window in one image and computing its correlation with pixel-wise shifted windows of the subsequent frame. The windows in this analysis had a size of 64 x 64 pixels, with an image resolution of 3.2 μm^2 per pixel. Consecutive windows were overlapping each other by 50%, yielding velocity vectors at intervals of 32 pixels (Figure 12 B). For every pair of images, a velocity field consisting of speeds (|v|), x-components (direction perpendicular to the gap), and y-components (parallel to the gap) were obtained. Speed dynamics were computed by averaging the speeds of every frame. The resulting vector fields can be summed up over the y-axis and plotted over time as seen in (Figure 12 C on the left), to visualize the migration dynamics over time. To estimate the relative contribution of directed motion to the overall motility we computed the ratio between the magnitude of the x-component with respect to the sum of both components: $|vx|/(|vx|+|vy|)$. To generate the cell density data, images were first segmented using a wavelet-based method for detecting Hoechst-labeled cell nuclei.[124] From this we obtained the positions of each cell for each video frame. To calculate the cell density, space was then divided into 50 rectangular boxes. From the amount of cells in each box, normed local cell densities were computed. These cell densities were plotted over time in a similar way, visualizing the gap closure (Figure 12 C on the right). For all migration analyses we used only frames taken during the first 30 h, during which significant speed dynamics were observed.
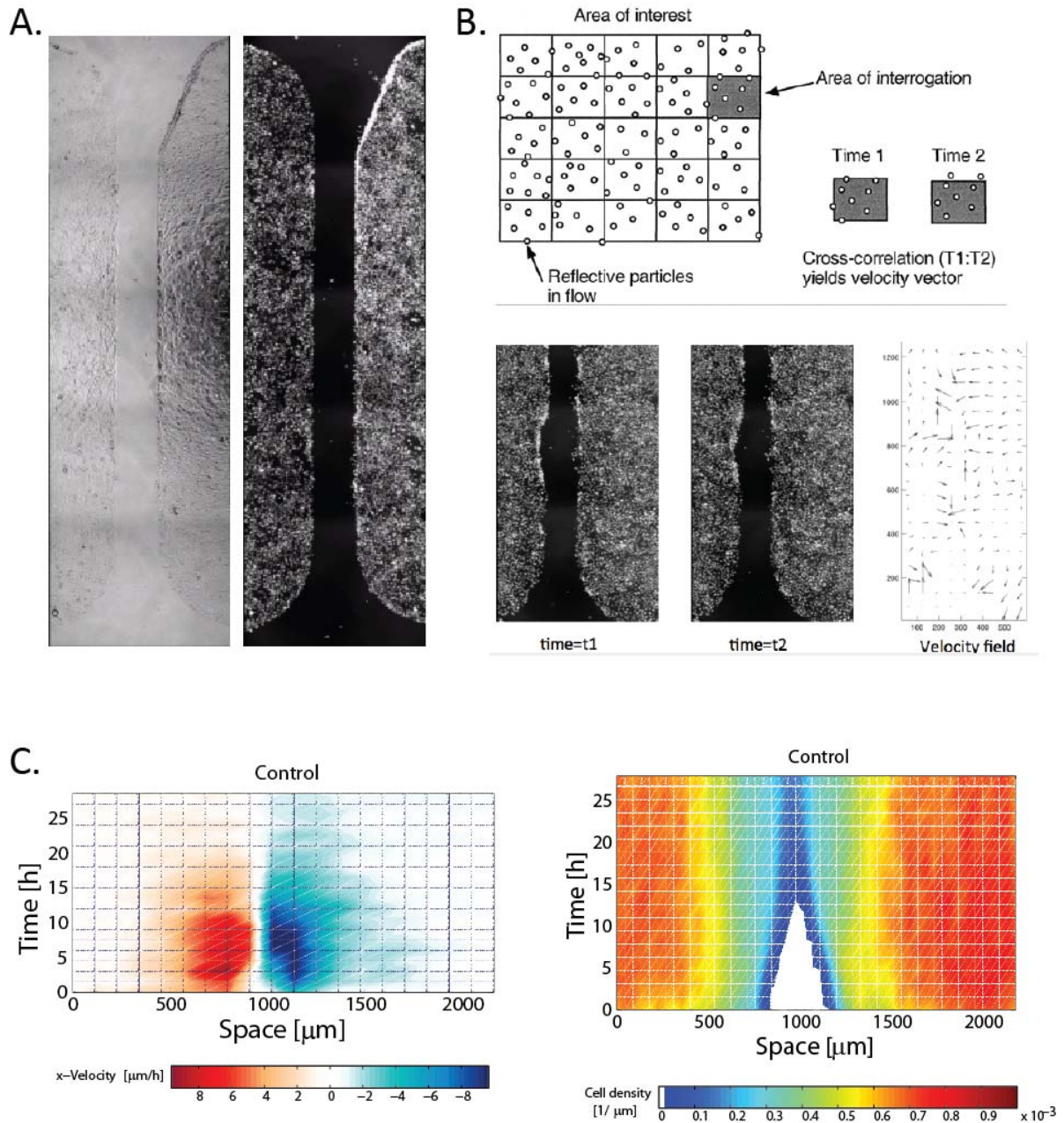
Figure 12: Overview over the *particle image velocimetry* **(PIV) technique. A. Stitched images from IBIDI 2D migration assays. Left: phase contrast, Right: HOECHST staining of nuclei. B. Schematics of PIV. Top: Distribution of rectangular regions of interest and cross correlation between two time points. Bottom: HOECHST staining of two consecutive time points and the resulting velocity vector field after cross correlation (pictures kindly provided by Dr. F. Matthäus. C. Left: speed distribution from HOECHST staining. Intensities were summed up over the y-axis of the images and plotted over time. Red color denotes movement to the right, blue color to the left. Color intensity stands for movement speed. Right: density distribution from HOECHST staining. Intensities were summed up over the y-axis of the images and plotted over time.**

3D migration/invasion analyses

For 3D migration/invasion assay analysis, phase contrast images were acquired over up to 72 h using the excellence RT software, with 90 min between pictures in 4x magnification. Images were analyzed together with the Group of Dr. D. Drasdo (INRIA, Paris).

For quantification of the spheroid invasion pattern the projection area, the area of the sprouts, the radius of gyration, the number of detached cells, and the space-filling fraction, i.e., the fraction of space occupied by cells, were considered. To be able to quantify and compare the brightfield images, the spheroid was segmented using a threshold, combining local grey level intensity and gradient information. In a pre-processing step, non-uniform illumination was corrected by using an iterative polynomial interpolation method.[125]

Figure 13 shows the result of this image processing algorithm, with spheroid segmentation (B) and density measurement (C) as well as the available measures. The area of the spheroid is the projection area given by the number of all pixels occupied by the cell body multiplied with the area of one pixel. The sprout area provides a measure for the spread of tumor cells from a sphere. Sprouting is described by a circle representing the radius of the spheroid body and sprout-associated pixel numbers, which do not belong to the spheroid body.
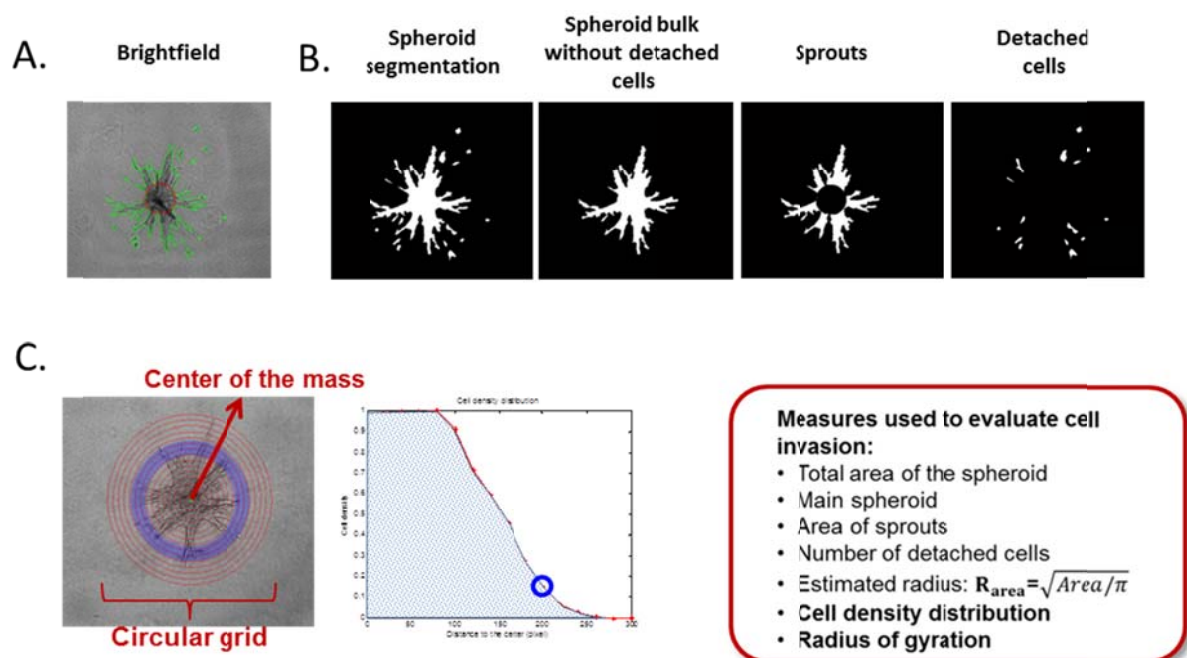
Figure 13: Results of novel image processing algorithm for spheroid assays. (A) Brightfield image of collagen embedded spheroids with sprouts and detached cells. Red circle defines the spheroid "body", while the green contour denotes the sprouts and detached cells. (B) Example for data segmentation of all pixels covered by cell material, the spheroid bulk, tumor cell sprouts, and detached cells. (C) Left: Circular grid originating from the spheroid center of mass . Right: Cell density plot over each grid circle

The radius of gyration is defined by $R_{gyr} = \sqrt{\frac{1}{N}\sum_i (r_i - R_{cm})^2}$ and represents an additional measure for the tumor cell spread. Here $R_{cm} = \frac{1}{N}\sum_i r_i$ defines the position of the spheroid mass center of all occupied pixels, with N the total number of documented pixels. If all pixels occupied by cell bodies fit into a circle, the radius of that circle is $R_{area} = \sqrt{A/\pi} = \sqrt{2}R_{gyr}$. In contrast, if the cell population forms fingers or if cells detach from the cell mass $\sqrt{A/\pi} < \sqrt{2}R_{gyr}$ is true. The space-filling fraction represents the proportion of space filled with cells. Inside a circle completely filled with cell material, this value is 1. Outside the circle the value decreases with increasing distance of cell material from the center of the circle. The area of the sprouts measure the extent of protrusions taking into account only cells connected to the main tumor cell mass. These are taken into account by the number of detached cells. The radius of gyration can be defined by all cells emerging from one spheroid with and without detached cells.

3.4.25 Statistical analysis and software

Data are presented as mean of at least three independent experiments including standard deviation (SD), except otherwise specified. P-values (significance level: < 0.01) were determined by the student's t-test. Statistical analyses were performed using IBM SSPS (V) Statistics and SAS version 9.2.

4 Results

4.1 Molecular characterization of model cell lines

Two independent adenocarcinoma cell lines (H838, H1975) were used in this study to analyze the effects of IGF-1/EGF signaling on pathway activation and cell phenotypes. Because the genetic background of these lines must have significant impact on the biological outcome and data interpretation, in a first step a molecular characterization for both model systems was performed using molecular diagnostics in the Institute for Pathology (Table 15). Fluorescence-*in situ* hybridization (FISH) analysis for amplification of c-MET and EGFR as well as for ALK translocation was negative in both cell lines. Sequencing for common aberrations in K-Ras, B-Raf, PIK3CA, and PTEN yielded negative results as well. Sequencing for EGFR mutations revealed the activating L858R and the T790M mutation, which confers resistance to Erlotinib in H1975, whereas H838 possesses non-mutated wild type receptor. Additionally, differentiation markers such as cytokeratins (CK5/6, CK7), *transcription intermediary factor 1-α* (TIF) and p63 were investigated: H838 showed CK7 positivity with CK5/6, TIF and p63 being negative, which represents a poorly differentiated phenotype, whereas H1975 showed a well differentiated phenotype with CK7 and TIF positivity and CK5/6 and p63 negativity.

Table 15: Results of cell line characterization for H838 and H1975 cell lines

Technique	Gene of interest	Exons [§]	Frequency (%) [$]	H838	H1975
FISH	c-MET		22	neg.	neg.
	EGFR		22	neg.	neg.
	ALK translocation		2-5	neg.	neg.
Sequencing	EGFR	ex 18, 19, 20, 21	15	neg.	T790M, L858R
	KRAS	ex 2, 3	30	neg.	neg.
	BRAF	ex 15	1-3	neg.	neg.
	PIK3CA	ex 1, 5, 7, 9, 20	1-3	neg.	neg.
	PTEN	ex 1 - 9	4-8	neg.	neg.
Differentiation				poor	well
				CK5/6⁻, CK7⁺, TIF⁻, p63⁻	CK5/6⁻, CK7⁺, TIF⁺, p63⁻

§ Exons: exons with clinically relevant alterations
$ Frequency: occurance of respective alteration in patients in percent
CK: cytokeratin, TIF: Transcription intermediary factor 1-alpha

To be able to investigate the effects of EGF and IGF-1 signaling in both cell lines used, the respective receptors need to be present on the cell surface. FACS analysis was employed to check for both EGFR and IGF-1R surface expression on both cell lines as shown in Table 16. IGF1-R positivity could be verified on the surface of 80.97% of H1975 cells and on 97.48% of H838 cells. EGFR surface expression was measured on 34.62% of H1975 and 15.42% of H838 cells, respectively. Combined positivity for both receptors was shown for 34% of H1975 and 15.34% of H838 cells.

Table 16: FACS analysis of IGF-1R and EGFR surface expression in H838 and H1975 cell lines

	+ IGFR	+ EGFR	+ IGFR / + EGFR
H1975	80.97	34.62	34.00
H838	97.48	15.42	15.34

4.2 Ligand secretion by NSCLC cells and cytokine uptake

To ensure that IGF-1 and EGF are taken up by the cells used, depletion experiments were performed using ELISA assays. Additionally, to exclude the possibility of signaling pathway activation through secretion and autocrine stimulation of IGF-1 and EGF, we investigated if H838 or H1975 produce EGF or IGF-1.
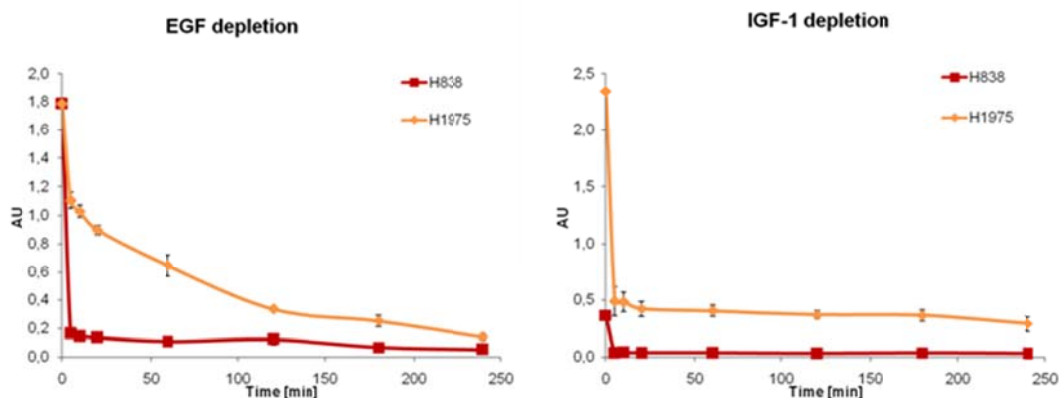
Figure 14: Uptake of EGF and IGF-1 by H838 and H1975 cells. (B) Uptake of EGF (left) and IGF-1 (right) in both H838 (orange) and H1975 (red) over 240 min. EGF was supplied with 500 pg/ml, IGF-1 with 5 ng/ml. Supernatant was collected after 5, 15, 30, 60, 120, 180 and 240 min and the residual amounts of growth factor were measured via ELISA. AU: arbitrary units.

Figure 14 shows that both cell lines depleted IGF-1 and EGF over a timeframe of 4 h with the strongest effects (at least 50% reduction) within the first 5 to 15 min. H838 cells showed complete depletion of both factors in the first 10 min. H1975 cells showed a similar dynamic for IGF-1, but a less pronounced depletion for EGF, where total depletion was achieved around 180 min. Additionally, neither H838 nor H1975 cells secrete any EGF or IGF-1 in measurable amounts over 24 h (data not shown). Thus, any stimulation with exogenous EGF and/or IGF-1 will not be distorted by secretion of the cells themselves.

4.3 Generation of an IGF-1/EGF-induced pathway model in NSCLC cells

In order to build a computational model to investigate the effects of EGF and IGF-1 stimulation on NSCLC cells, protein activation of key players in the pathway was assessed. This protein activation represents the most direct readout to link stimulation input with cellular responses. Randomized Western immunoblotting was used as a well-established and defined method to generate semi-quantitative time course data with high reproducibility.

4.3.1 Data acquisition

Specific antibodies (see Table 6) recognizing key nodes in the IGF-1R and EGFR pathways were tested by Western immunoblotting using total protein extracts from H838 cells. As shown in Figure 15, IGF-1R, EGFR, ERK, and AKT could be detected. Antibody specificity was tested by siRNA-mediated knockdown of total receptors, which reduced the signal for both IGF1-R and EGFR. After treatment with EGF or IGF, phosphorylation of EGFR or IGF-1R was detected, respectively. Equally, phosphorylation of the downstream effectors ERK1/2, AKT was observed.
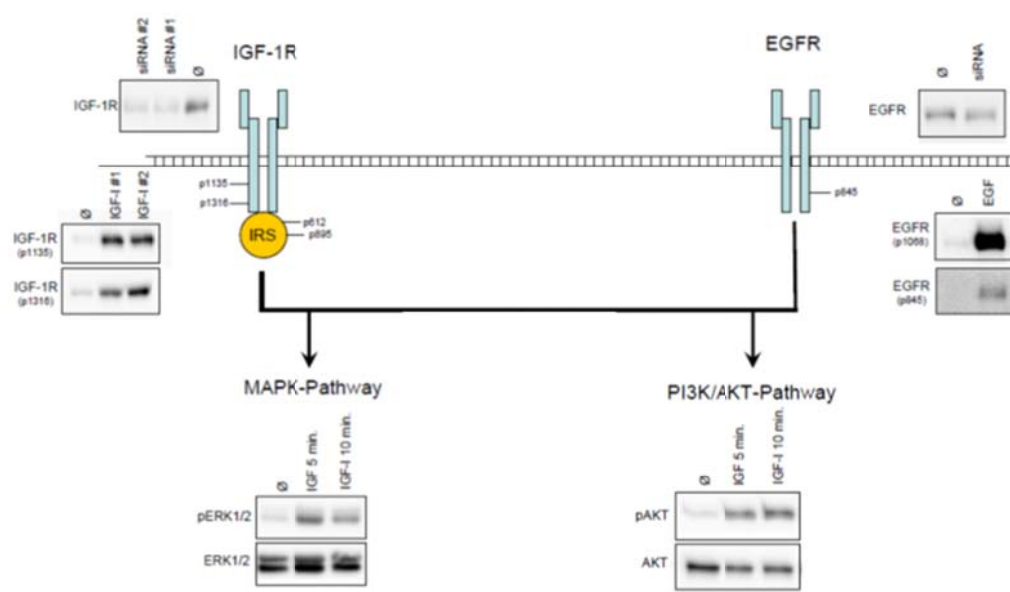
Figure 15: Western immunoblot analysis of key pathway components for IGF-1R and EGFR. Shown are bands for the total receptors, two phosphorylation sites for each receptor as well as total and phosphorylated forms of downstream effectors ERK1/2 and AKT. Antibody specificity for the total receptors was shown by siRNA knockdown of the receptors. Inducibility of the pathway is illustrated by an increase in phosphorylated receptors and downstream effectors after administration of EGF or IGF, 50 ng/ml each.

4.3.2 Protein activation kinetics for H838 cells

The ODE modeling approach used here is especially suited to simulate the important dynamic behavior of cell signaling. In order to generate a dataset as the foundation for such an ODE model, kinetics of H838 cells after stimulation with IGF-1, EGF, or both were generated. To this end, H838 cells were stimulated with 50 ng/ml of IGF-1, 50 ng/ml EGF or 50 ng/ml of both IGF-1 and EGF. Cells were harvested at 0, 5, 10, 20, 30, 60, 120, and 240 min after stimulation, lysed and analyzed with semi quantitative Western immunoblotting. Figure 16 shows the augmented trajectories of the quantified protein kinetics.

The unstimulated control cells showed no phosphorylation in the observed pathway components. In contrast, stimulation with EGF, IGF and both growth factors showed distinct effects, with EGF stimulation resulting in in the following:

- No crossactivation of IGF-1R.
- EGFR reacted to EGF stimulation with rapid but transient induction of EGFR phosphorylation, with the peak activation being reached at 10 min.
- Total EGFR levels decreased after EGF administration, with a steep drop in the first 10 min and a sustained reduction over the observed treatment.
- Phosphorylation levels of ERK displayed a steep increase after EGF stimulation, with a peak activation after 10 min and a reduction in levels to about the starting amounts over the 240 min timeframe, closely resembling the EGFR activation dynamic.
- AKT phosphorylation responded quickly to EGF treatment with a similar dynamic as ERK activation after EGF treatment: a steep increase and a maximum at 10 min followed by a reduction to the starting amounts.

IGF-1 stimulation resulted in an equally clear, but partly different activation behavior:

- No cross-activation with EGFR
- Rapid phosphorylation IGF-1R after 5 min with sustained activation over the observed timeframe of 240 min.
- In contrast to EGF treatment, AKT phosphorylation showed a slower increase, with a comparatively lower maximum at 30 min and a sustained activation over the 240 min.
- Treatment with IGF-1 elicited only a moderate response in ERK phosphorylation.

Double stimulation with IGF-1 and EGF yielded the following results:

- The IGF-1R phosphorylation dynamic was similar to treatment with IGF-1 alone.
- EGFR phosphorylation was reduced compared to EGF alone.
- Total EGFR levels behaved like with EGF treatment
- An additive response in pAKT, with a steep increase and a maximum at 10 min that was higher than after treatment with EGF alone and a sustained activation similar to the IGF-1 treatment.
- Phosphorylation levels of ERK showed no difference from the dynamic displayed after treatment with only EGF

Thus distinct differences in pathway activation between EGF and IGF-1 treatment could be observed, with the EGF signal being transduced over both ERK and AKT, whereas the IGF-1 signal elicited only a low response in ERK and a strong one in AKT. Curiously, double stimulation reduced the activation of EGFR, although no receptor cross activation was detected. Crosstalk between the pathways could be detected in AKT phosphorylation, where double stimulation resulted in an additive response. ERK showed no reduced phosphorylation in the double stimulation compared to EGF alone, even though EGFR activation was reduced in the double stimulation. This also implies an additive effect with the low activation of ERK *via* IGF-1R.
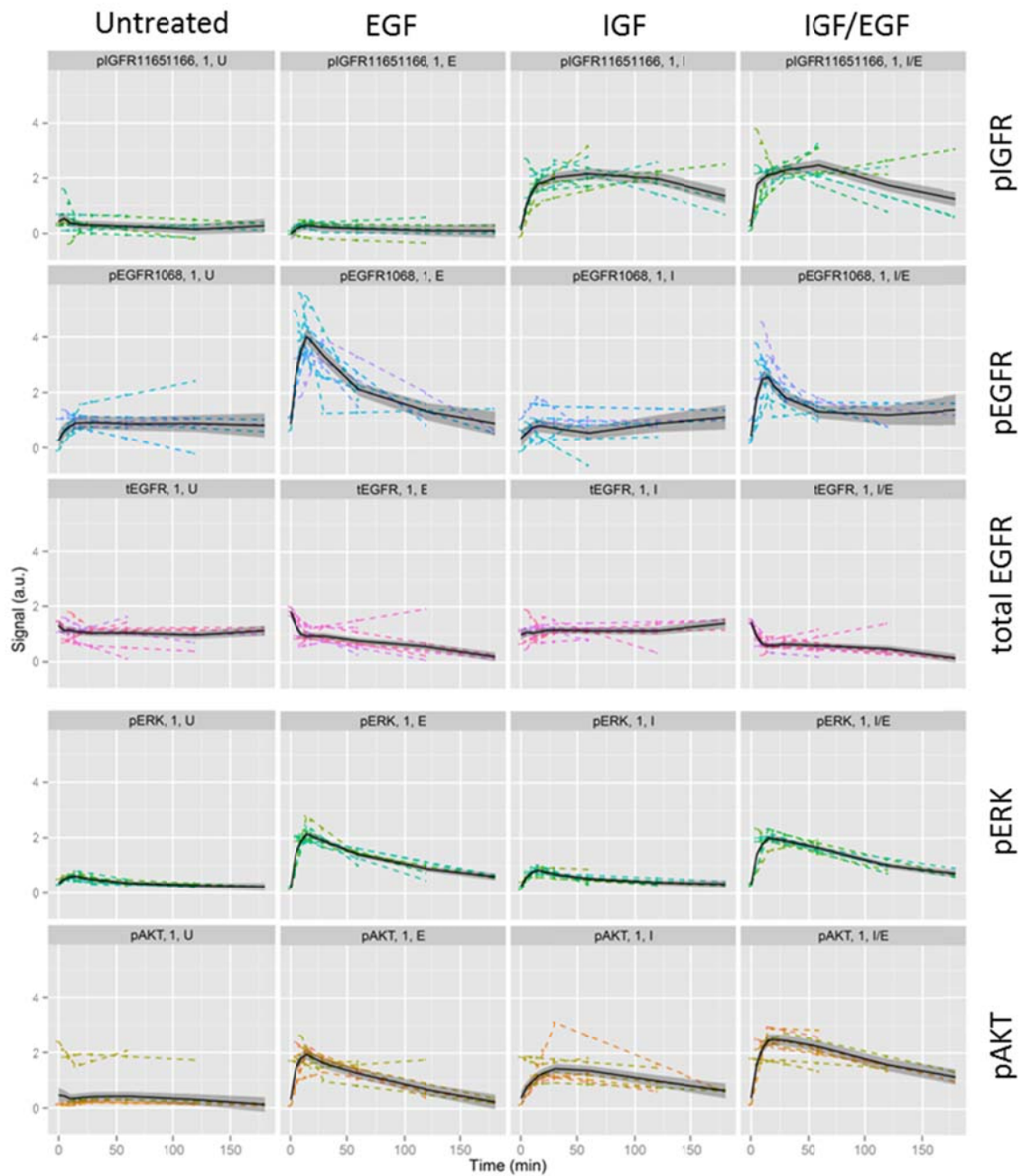
Figure 16: Protein kinetics of key pathway components in H838 cells after stimulation with 50 ng/ml EGF, 50 ng/ml IGF-1 and double stimulation with 50 ng/ml of both factors as well as the untreated control, monitored over 180 min. Filled circles represent quantifications of Western immunoblotting signals; empty circles are results of linear interpolation between two real data points. Results of three independent biological experiments are displayed. The mean is depicted by the black line. The grey band around the mean denotes the standard error of the mean estimation.

4.3.3 First ODE model for IGF-1/EGF-induced signaling in H838 cells

Model topology and ODEs

Based on the H838 pathway activation dataset, a first model was constructed by Dr. C. Maus from the Group of Prof. T. Höfer using ODEs. The topology is shown in Figure 17. Boxes represent the observed protein species, arrows represent the reactions. In total the model comprises 12 protein species (proteins and protein conditions) and 17 reactions.
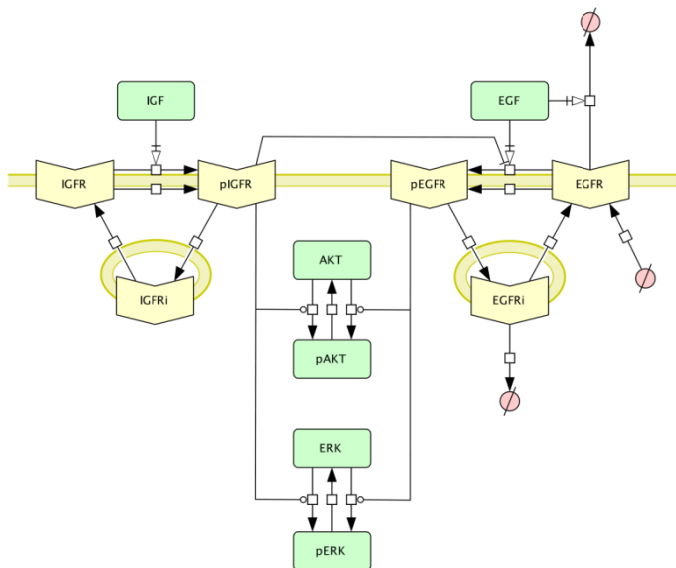
Figure 17: Model topology for the first pathway model constructed from H838 pathway activation data. Boxes represent observed protein species. Arrows represent reactions. Generated with CellDesigner.

For the generation of the pathway model the following requirements were considered:

- The receptors can be phosphorylated with a baseline speed. Adding the ligand increases this speed.

- The phosphorylated receptors are internalized and recycled to the cell surface.

- The phosphorylated receptors effect the phosphorylation of AKT and ERK. pAKT and pERK both are dephosphorylated at a constant rate.

- In order to explain the steep drop of total EGFR in the early time points before phosphorylation of the receptor, EGFR can be degraded directly after ligand binding, but before phosphorylation.

- The internalized EGFR can be degraded as well, to explain the sustained reduction over the observed 240 min.

- The activated IGF-1R can inhibit the phosphorylation of EGFR in order to model the reduced activation of EGFR under double stimulation.

The underlying ODEs are summarized in Figure 18, together with initial concentration parameters that were established by solving the respective ODE systems in order to start the unstimulated system from a steady state.

$$
\begin{aligned}
\mathrm{d[IGFR]}/\mathrm{dt} &= -v_1 - v_2 + v_4 \\
\mathrm{d[pIGFR]}/\mathrm{dt} &= +v_1 + v_2 - v_3 \\
\mathrm{d[IGFRi]}/\mathrm{dt} &= +v_3 - v_4 \\
\mathrm{d[EGFR]}/\mathrm{dt} &= +v_5 - v_6 - v_7 - v_8 + v_{10} \\
\mathrm{d[pEGFR]}/\mathrm{dt} &= +v_6 + v_7 - v_9 \\
\mathrm{d[EGFRi]}/\mathrm{dt} &= +v_9 - v_{10} - v_{11} \\
\mathrm{d[AKT]}/\mathrm{dt} &= -v_{12} - v_{13} + v_{14} \\
\mathrm{d[pAKT]}/\mathrm{dt} &= +v_{12} + v_{13} - v_{14} \\
\mathrm{d[ERK]}/\mathrm{dt} &= -v_{15} - v_{16} + v_{17} \\
\mathrm{d[pERK]}/\mathrm{dt} &= +v_{15} + v_{16} - v_{17}
\end{aligned}
$$

$$
\begin{aligned}
v_1 &= \mathrm{[IGFR] \cdot k\_phos\_IGFR\_basal} \\
v_2 &= \mathrm{[IGF] \cdot [IGFR] \cdot k\_phos\_IGFR} \\
v_3 &= \mathrm{k\_endo\_IGFR \cdot [pIGFR]} \\
v_4 &= \mathrm{[IGFRi] \cdot k\_rec\_IGFR} \\
v_5 &= \mathrm{k\_syn\_EGFR} \\
v_6 &= \mathrm{[EGFR] \cdot k\_phos\_EGFR\_basal} \\
v_7 &= \frac{\mathrm{[EGF] \cdot [EGFR] \cdot k\_phos\_EGFR}}{\mathrm{[pIGFR]} + 1} \\
v_8 &= \mathrm{[EGF] \cdot [EGFR] \cdot k\_deg\_EGFR} \\
v_9 &= \mathrm{k\_endo\_EGFR \cdot [pEGFR]} \\
v_{10} &= \mathrm{[EGFRi] \cdot k\_rec\_EGFR} \\
v_{11} &= \mathrm{[EGFRi] \cdot k\_deg\_EGFRi} \\
v_{12} &= \mathrm{[AKT] \cdot k\_phos\_AKT\_E \cdot [pEGFR]} \\
v_{13} &= \mathrm{[AKT] \cdot k\_phos\_AKT\_I \cdot [pIGFR]} \\
v_{14} &= \mathrm{k\_dephos\_AKT \cdot [pAKT]} \\
v_{15} &= \mathrm{[ERK] \cdot k\_phos\_ERK\_E \cdot [pEGFR]} \\
v_{16} &= \mathrm{[ERK] \cdot k\_phos\_ERK\_I \cdot [pIGFR]} \\
v_{17} &= \mathrm{k\_dephos\_ERK \cdot [pERK]}
\end{aligned}
$$

Transformation of initial concentration parameters to achieve steady-state of unstimulated system:

$$
\mathrm{init\_IGFR} \rightarrow \frac{\mathrm{init\_pIGFR \cdot k\_endo\_IGFR}}{\mathrm{k\_phos\_IGFR\_basal}}
$$

$$
\mathrm{init\_IGFRi} \rightarrow \frac{\mathrm{init\_pIGFR \cdot k\_endo\_IGFR}}{\mathrm{k\_rec\_IGFR}}
$$

$$
\mathrm{init\_EGFR} \rightarrow \frac{\mathrm{k\_syn\_EGFR \cdot (k\_deg\_EGFRi + k\_rec\_EGFR)}}{\mathrm{k\_deg\_EGFRi \cdot k\_phos\_EGFR\_basal}}
$$

$$
\mathrm{init\_pEGFR} \rightarrow \frac{\mathrm{k\_syn\_EGFR \cdot (k\_deg\_EGFRi + k\_rec\_EGFR)}}{\mathrm{k\_deg\_EGFRi \cdot k\_endo\_EGFR}}
$$

$$
\mathrm{init\_EGFRi} \rightarrow \frac{\mathrm{k\_syn\_EGFR}}{\mathrm{k\_deg\_EGFRi}}
$$

$$
\mathrm{init\_AKT} \rightarrow \frac{\mathrm{init\_pAKT \cdot k\_deg\_EGFRi \cdot k\_dephos\_AKT \cdot k\_endo\_EGFR}}{\mathrm{k\_deg\_EGFRi \cdot k\_phos\_AKT\_E \cdot k\_syn\_EGFR + k\_phos\_AKT\_E \cdot k\_rec\_EGFR \cdot k\_syn\_EGFR + init\_pIGFR \cdot k\_deg\_EGFRi \cdot k\_endo\_EGFR \cdot k\_phos\_AKT\_I}}
$$

$$
\mathrm{init\_ERK} \rightarrow \frac{\mathrm{init\_pERK \cdot k\_deg\_EGFRi \cdot k\_dephos\_ERK \cdot k\_endo\_EGFR}}{\mathrm{k\_deg\_EGFRi \cdot k\_phos\_ERK\_E \cdot k\_syn\_EGFR + k\_phos\_ERK\_E \cdot k\_rec\_EGFR \cdot k\_syn\_EGFR + int\_pIGFR \cdot k\_deg\_EGFRi \cdot k\_endo\_EGFR \cdot k\_phos\_ERK\_I}}
$$

Figure 18: ODEs underlying the first pathway model from H838 data. Left: v1 to v17 describe the reactions in the model with the relevant concentrations and reaction constants. Bottom: initial concentrations of total and phosphorylated receptors and total AKT and ERK, computed by solving the ODEs at time point zero. ODEs were defined by Dr. Carsten Maus (Prof. Thomas Höfer, Bioquant).

Model calibration and parameter identifiability

After establishing the model structure and generating the ODEs describing the reactions, the model was calibrated and model fits assessed. Figure 19A shows the calibration fits for all relevant observables (pAKT, pERK, pEGFR, pIGF-1R and total EGFR) in all four biological conditions. Total IGF-1R levels did not react to any of the treatments, and are therefore not shown. Agreement between the data points (dots) and the model fits (lines) was very good for pAKT in the unstimulated control, the EGF, and the double stimulation treatment. For the IGF-1 treatment, the values and model fit diverged after 60 min with the last two time points outside the confidence interval. For pERK, the situation was similar, with EGF and double stimulation showing good fits to the data points. The fit for IGF treatment in principle showed the same dynamic as the data with slight misalignment at 15 min. For pEGFR, all four biological conditions were described by the model. The fits for pIGFR also captured the dynamics of the control, EGF, and double stimulation. The IGF-1 stimulation dynamic is also described quite well, if overestimating the maximal activation (the fit overlaps the one for the double stimulation). Lastly, the fits for the total EGFR kinetics accurately described the depletion of EGFR under EGF and double stimulation.

Table 17: Nomenclature of relevant model parameters. Parameters for scaling factors and standard deviation estimation are omitted for clarity.

Parameter name	Description
init_pAKT	initial amount of phosphorylated AKT as defined in Figure 18
init_pERK	initial amount of phosphorylated ERK as defined in Figure 18
init_pIGFR	initial amount of phosphorylated IGF-1R as defined in Figure 18
init_ EGFR	initial amount of phosphorylated EGFR as defined in Figure 18
k_deg_EGFR	reaction constant of the degradation of EGF bound EGFR before phosphorylation
k_deg_EGFRi	reaction constant of the degradation of internalized EGFR
k_dephos_AKT	reaction constant of the dephosphorylation of activated AKT
k_dephos_ERK	reaction constant of the dephosphorylation of activated ERK
k_endo_EGFR	reaction constant of the internalization of EGFR

k_endo_IGFR	reaction constant of the internalization of IGF-1R
k_phos_AKT_E	reaction constant of the phosphorylation of AKT *via* the activated EGFR
k_phos_AKT_I	reaction constant of the phosphorylation of AKT via the activated IGF-1R
k_phos_EGFR	reaction constant of the ligand induced phosphorylation of EGFR
k_phos_EGFR_basal	reaction constant of the basal phosphorylation of EGFR
k_phos_ERK_E	reaction constant of the phosphorylation of ERK via the activated EGFR
k_phos_ERK_I	reaction constant of the phosphorylation of ERK via the activated IGF-1R
k_phos_IGFR	reaction constant of the ligand induced phosphorylation of IGF-1R
k_phos_IGFR_basal	reaction constant of the basal phosphorylation of IGF-1R
k_rec_EGFR	reaction constant of the recycling of internalized EGFR to the cell surface
k_rec_IGFR	reaction constant of the recycling of internalized IGF-1R to the cell surface
k_syn_EGFR	reaction constant of the synthesis of EGFR

The profile-likelihood analysis shown in Figure 19B revealed good identifiability of most parameters, with nine parameters being structurally non-identifiable: The phosphorylation and dephosphorylation constants for both ERK and AKT (k_dephos_AKT, k_dephos_ERK. k_phos_AKT_E, k_phos_AKT_I,k_phos_ERK_E, k_phos_ERK_I) as well as the constant for the phosphorylation of the IGF-1R (k_phos_IGFR), the constant for internalization of IGF-1R (k_endo_IGFR), and the constants for recycling of both receptors to the plasma membrane (k_rec_EGFR and k_rec_IGFR).
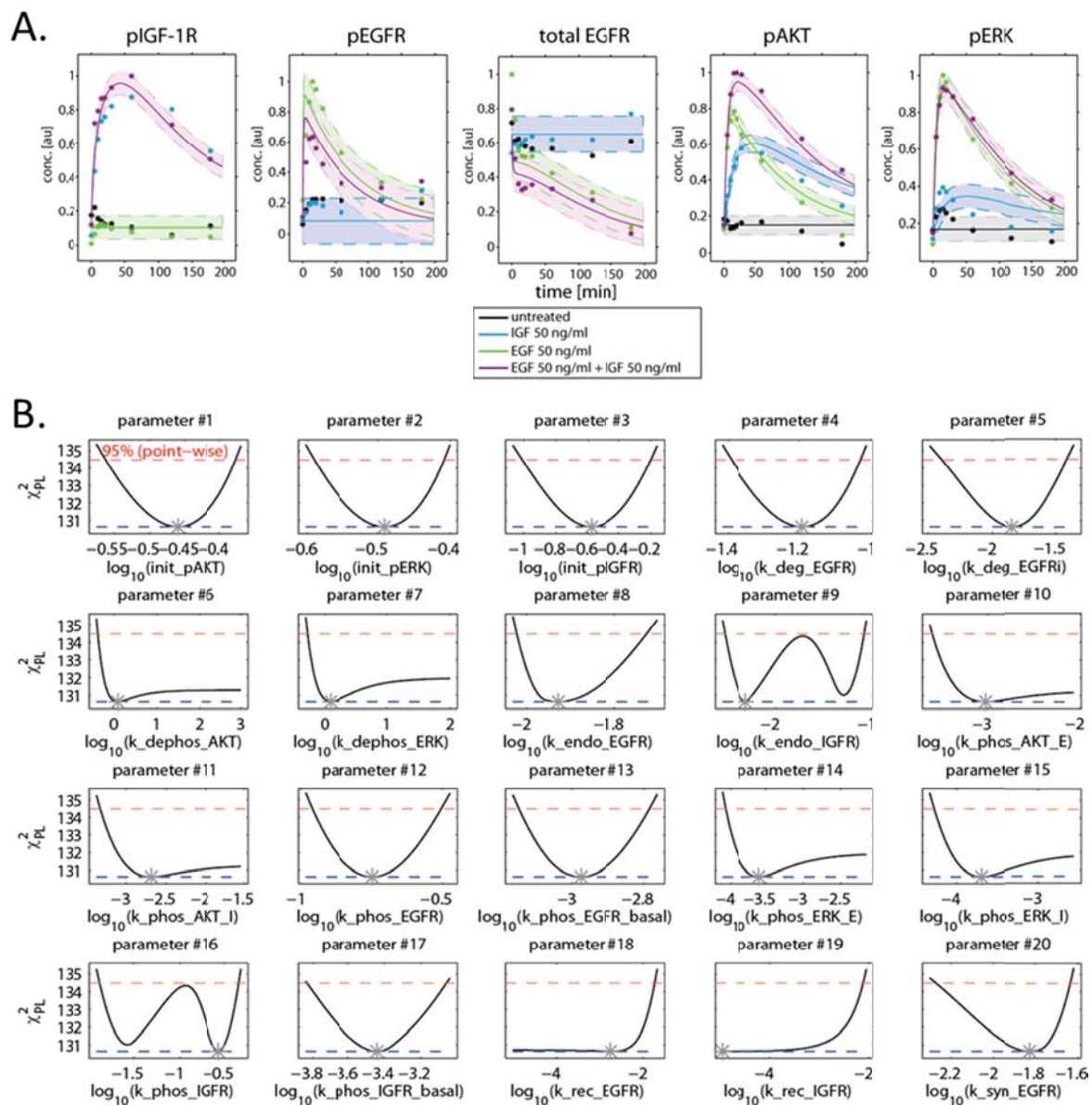
Figure 19: Calibration and parameter profile likelihoods for the first EGFR/IGF-1R pathway model in H838 cells. (A). Calibration fits for the important activated nodes in the pathway: pIGFR, pEGFR and total EGFR, as well as pAKT and pERK. Measured data points are represented by dots, lines denote the model fits with confidence bands. (B) Parameter profile likelihood plots. Shown are the *profile-likelihood estimation* (PLE) plots for all biological parameters. PLEs for scaling factors and standard deviations are fully identifiable and omitted for clarity. Red line denotes 95% confidence interval. Blue line denotes the minimal log likelihood.

4.3.4 Dose response of H838 cells and refining the pathway model

In order to increase parameter identifiability of the ODE pathway model, dose response data of H838 cells at 10 min after stimulation with 0, 0.1, 2.5, 5, 10, 50 ng/ml of IGF-1, EGF, and double stimulation of both factors was generated. Figure 20A shows the resultant dose-response curves of phosphorylated IGF-1R, EGFR ERK, and AKT.
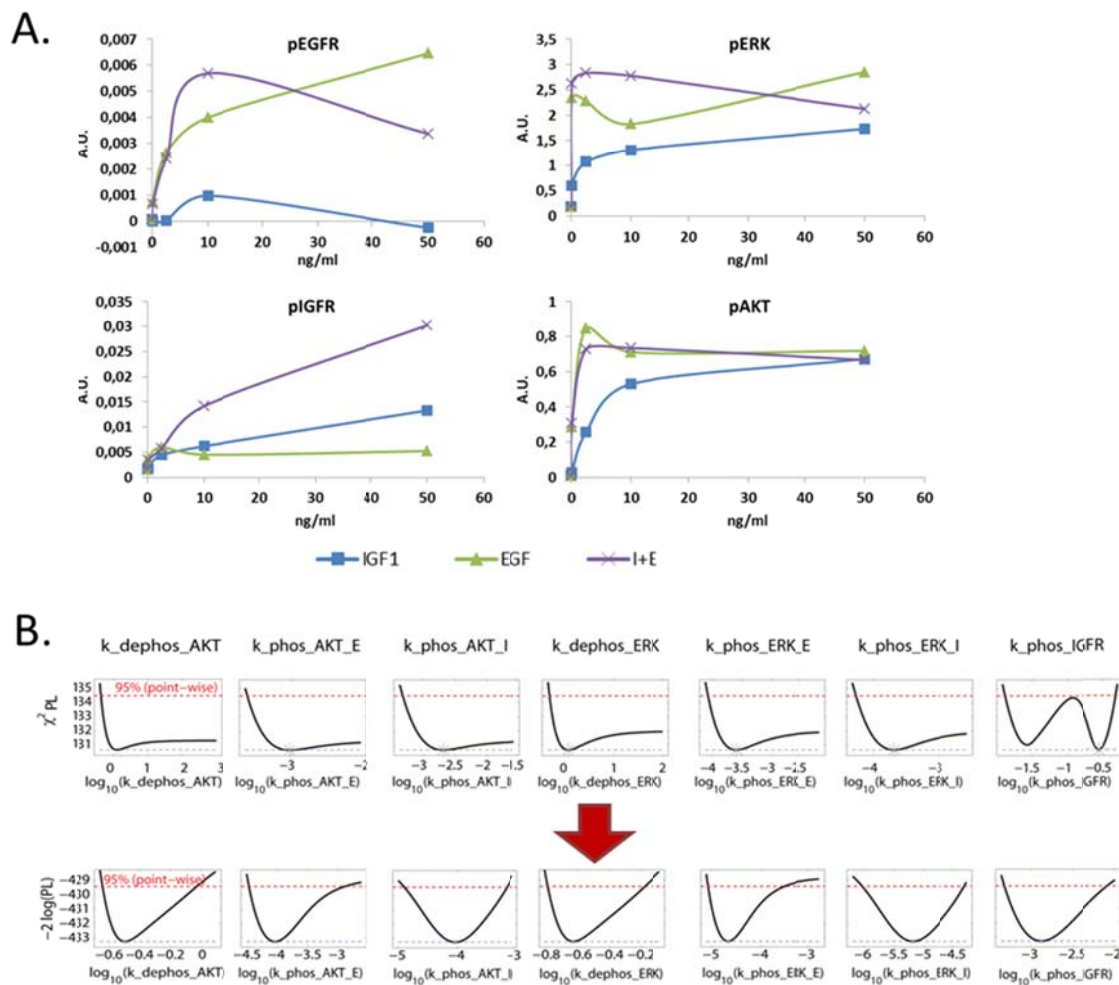
Figure 20: Dose-response protein kinetics of key pathway components in H838 cells. Cells were stimulated with 0, 0.1, 2.5, 5, 10, 50 ng/ml of IGF-1 (blue), EGF (green), and double stimulation of both factors (violet). Shown are the resultant curves of phosphorylated EGFR, IGF-1R, ERK and AKT after quantification. (B) Parameter profile likelihood plots before (upper row) and after (lower row) incorporation of dose-response data. Shown are the PLE plots for those biological parameters with improved identifiability. Red line denotes 95% confidence interval. Blue line denotes the minimal log likelihood.

EGFR and IGF-1R showed dose dependency for their ligands up to 50 ng/ml and no influence of the opposite ligand. Double stimulation increased phosphorylation compared to single treatment for both receptors at 10 ng/ml and for IGF-1R at 50 ng/ml, whereas EGFR phosphorylation decreased at that point. ERK phosphorylation after EGF stimulation showed a moderate increase in strength depending with rising concentration. IGF stimulation resulted in a generally lower but more differentiated dose response, with a

strong increase in signal until 5 ng/ml, saturating after 10 ng/ml at about half the intensity of treatment with 50 ng/ml of EGF. Double stimulation showed an increase over EGF stimulation at concentrations up to 10 ng/ml. 50 ng/ml of both factors decrease the phosphorylation compared to EGF treatment. Activation of AKT resulted in a strong increase in both single treatments until 10 ng/ml where the response saturated, with IGF starting a lower but reaching comparable phosphorylation levels with 50 ng/ml. Double treatment did not increase the phosphorylation of AKT compared to EGF stimulation.

Incorporating these data into the model calibration significantly improved identifiability for k_dephos_AKT, k_dephos_ERK. k_phos_AKT_E, k_phos_AKT_I,k_phos_ERK_E, k_phos_ERK_I and k_phos_IGFR (Figure 7B). Only k_endo_IGFR as well as k_rec_EGFR and k_rec_IGFR remain unidentifiable.

4.3.5 Utilization of the IGF-1/EGF pathway model on H1975 cells

After generating a first ODE pathway model derived from H838 data, we took steps to adapt this model to data from the H1975 cell line. To this end, cells were stimulated with 50 ng/ml of IGF-1, 50 ng/ml EGF or 50 ng/ml of both IGF-1 and EGF, analogous to the dataset from H838. Cells were also harvested at identical time points (4.3.2). Generally, the data was noisier than the results derived from H838 cells. Especially large variances were observed in the pAKT signals upon cytokine stimulation. Nonetheless, there was an IGF-1R activation after IGF-1 and double stimulation which progressed more transient than in H838, with a steep increase and a peak at 10 min. Only a low EGFR activation was detectable for all biological conditions, which was probably due to the L858R activation mutation in exon 21. Nevertheless, a clear downstream activation of ERK after EGF administration was apparent. This pERK signal increased sharply until it reached a maximum at 10 min and then decreased until baseline activation was reached between 120 and 240 min. Effects on AKT phosphorylation were only detected in double stimulations, where an increase until 20 min results in sustained activation over the observed timeframe. Effects in the other biological conditions could be masked by the high variance in the data.

4.3.6 Dose response of H1975 cells

Analogous to H838 cells, the dose response was quantitatively defined for model integration. Therefore, H1975 cells were harvested at 10 min after stimulation with 0, 0.1, 2.5, 5, 10, and 50 ng/ml of IGF-1, EGF, and double stimulation of both factors identical concentrations. Figure 21 shows the resultant dose-response curves of phosphorylated IGF-1R, EGFR ERK and AKT after quantification. Phosphorylation of EGFR was unresponsive to

all three treatments, probably due to the activating L858 mutation. In contrast, IGF-1R phosphorylation showed clear dose dependency with a steep increase in activation at 10 ng/ml and a slight reduction again at 50 ng/ml. EGF treatment showed no effect and, consequently, double stimulation with 50 ng/ml of both IGF-1 and EGF resulted in the same activation as IGF-1 treatment alone. Surprisingly, although no change in EGFR phosphorylation was detectable, downstream activation of both ERK and AKT after EGF stimulation showed clear dose effects. ERK phosphorylation increased steeply until 10 ng/ml of EGF and then saturated. AKT phosphorylation after EGF stimulation also increased until 10 ng/ml, followed by a less pronounced increase with 50 ng/ml. Stimulation with IGF-1 generally resulted in lower responses, with ERK phosphorylation saturating already at 0.1 ng/ml whereas AKT phosphorylation saturated at 10 ng/ml. Double stimulation with EGF and IGF-1 revealed a phospho-ERK response on the same level as EGF treatment alone, while phospho-AKT levels showed an increase over EGF stimulation at concentrations up to 10 ng/ml, where the curve saturated.
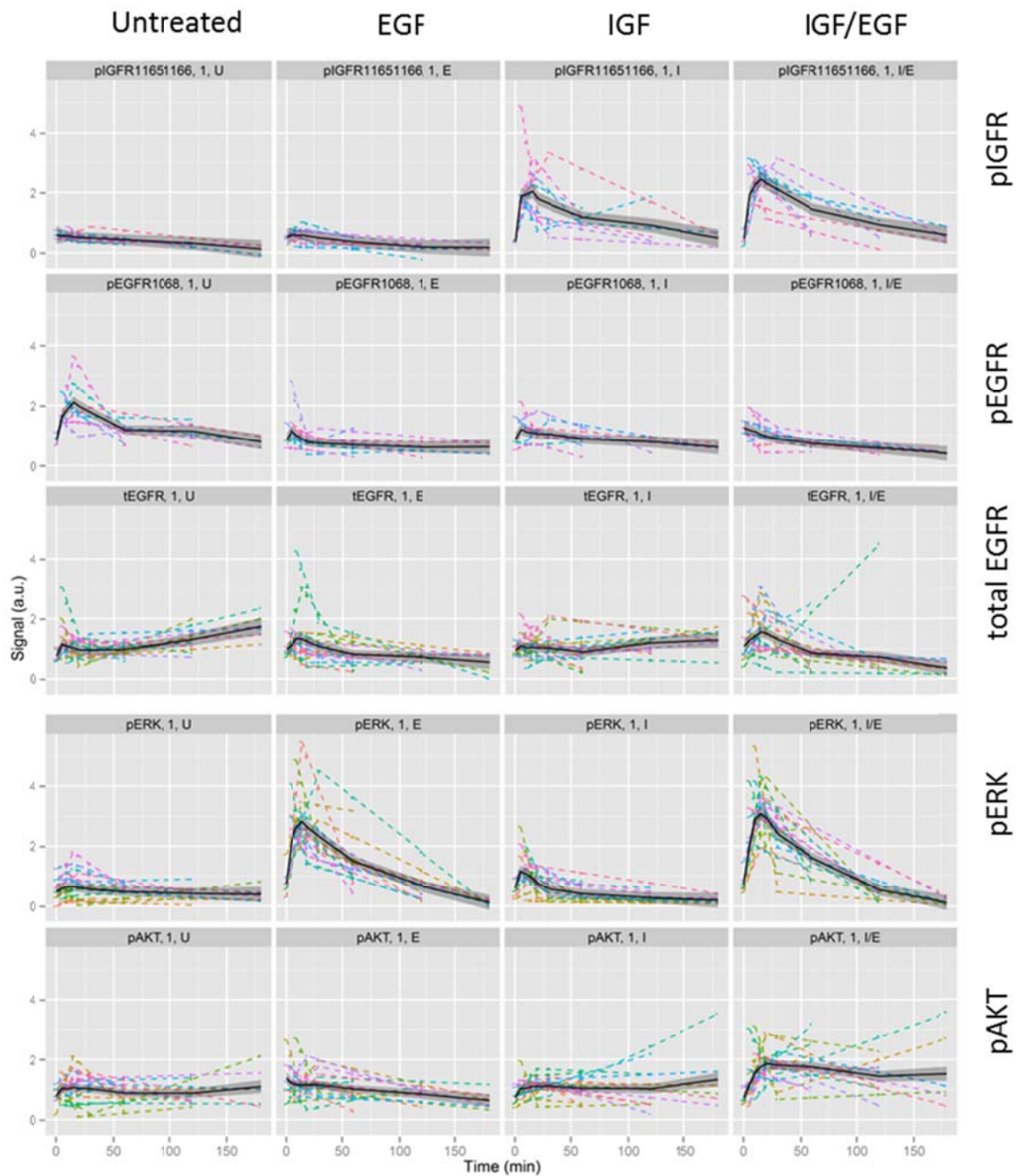
Figure 21: Protein kinetics of key pathway components in H1975 cells. Activation was measured over 180 min after stimulation with 50 ng/ml EGF, 50 ng/ml IGF-1, and double stimulation with 50 ng/ml of both factors as well as the untreated control. Filled circles represent quantifications of actual Western blot bands, empty circles are results of linear interpolation between two real data points. Shown are the results of 6 independent experiments. The mean is depicted by the black line. The grey band around the mean denotes the standard error of the mean estimation.
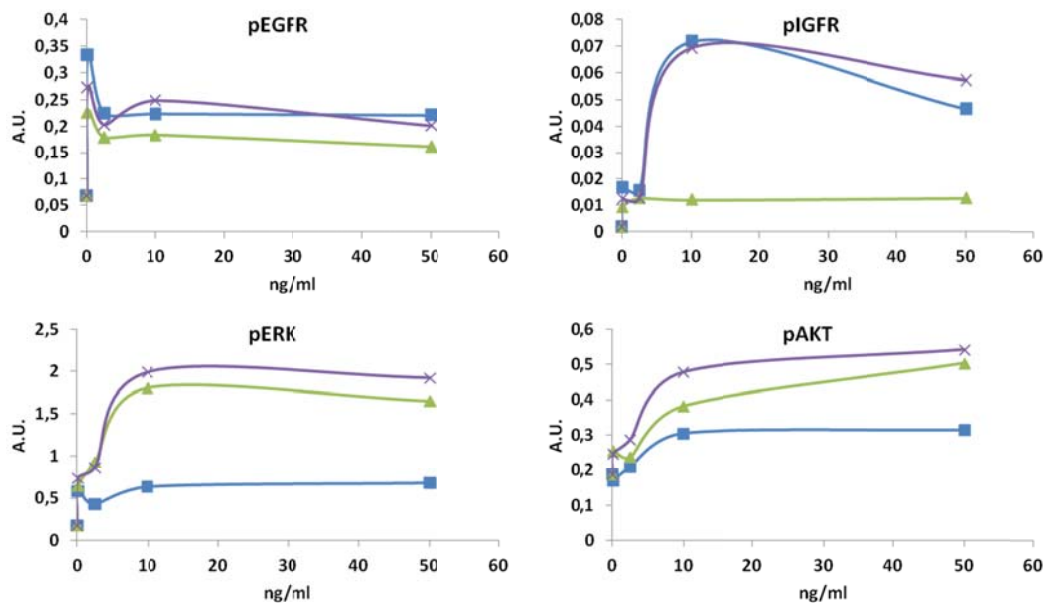
Figure 22: Dose-response protein kinetics of key pathway components in H1975. Cells were stimulated with 0, 0.1, 2.5, 5, 10, 50 ng/ml of IGF-1 (blue), EGF (green), and double stimulation with both factors (violet). Shown are the resultant curves of phosphorylated EGFR, IGF-1R, ERK and AKT

4.3.7 Adaptation of the ODE pathway model to the H1975 data and model confirmation

As a first step towards adapting the H838 pathway model to the H1975 cell line, it was fitted to the IGF-1R activation data of both datasets. The IGF1-R portion of the pathway could be explained with the same model for both pathways. To increase the quality of model fits, an inhibitory loop from activated IGF-1R for the phosphorylation of IGF-1R was introduced as shown in Figure 24 A/B as an abstract representation of autoinhibitory mechanisms. This resulted in better model fits for both the H838 and the H1975 data (Figure 24). PLE analysis of the model fitted with the H838 kinetics, H838 dose-response, and IGFR-1 dynamic data from H1975 cells yielded improved identifiabilty, with the constant for internalization of IGF-1R (k_endo_IGFR) becoming identifiable as evidenced by Figure 24C. Thus, only the constants for recycling of both receptors to the cell surface (k_rec_IGFR and k_rec_EGFR) remained unidentifiable.

Additionally, to be able to explain both datasets at once, the assumption that H838 cells contain 17 times more total IGF-1R than H1975, has to be taken by the model. Validation by semi quantitative Western immunoblotting comparing the total amounts of IGF-1R between the two cell lines revealed that H838 cells express 21-times as much IGF-1R than H1975

(Figure 23). As this result presents satisfactory agreement between the model assumption and experimental validation, we gained first evidence for the accuracy of the combined model so far.
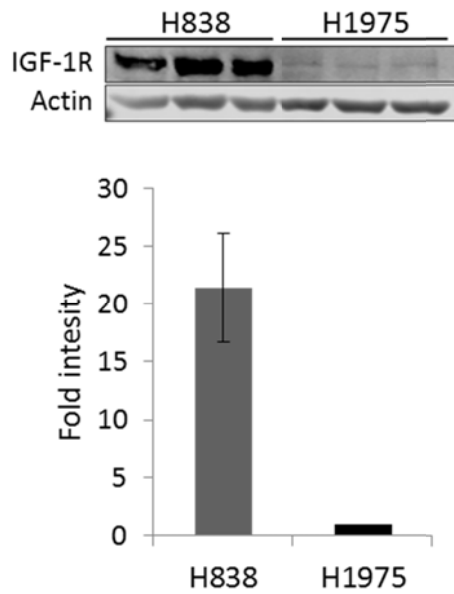
Figure 23: Western immunoblot validation of model assumption for total IGF-1R amounts. Left: image of total cell lysates of H838 and H1975 in technical triplicates, probed with antibodies against total IGF-1R. Right: fold change quantification of the Western immunoblot data.
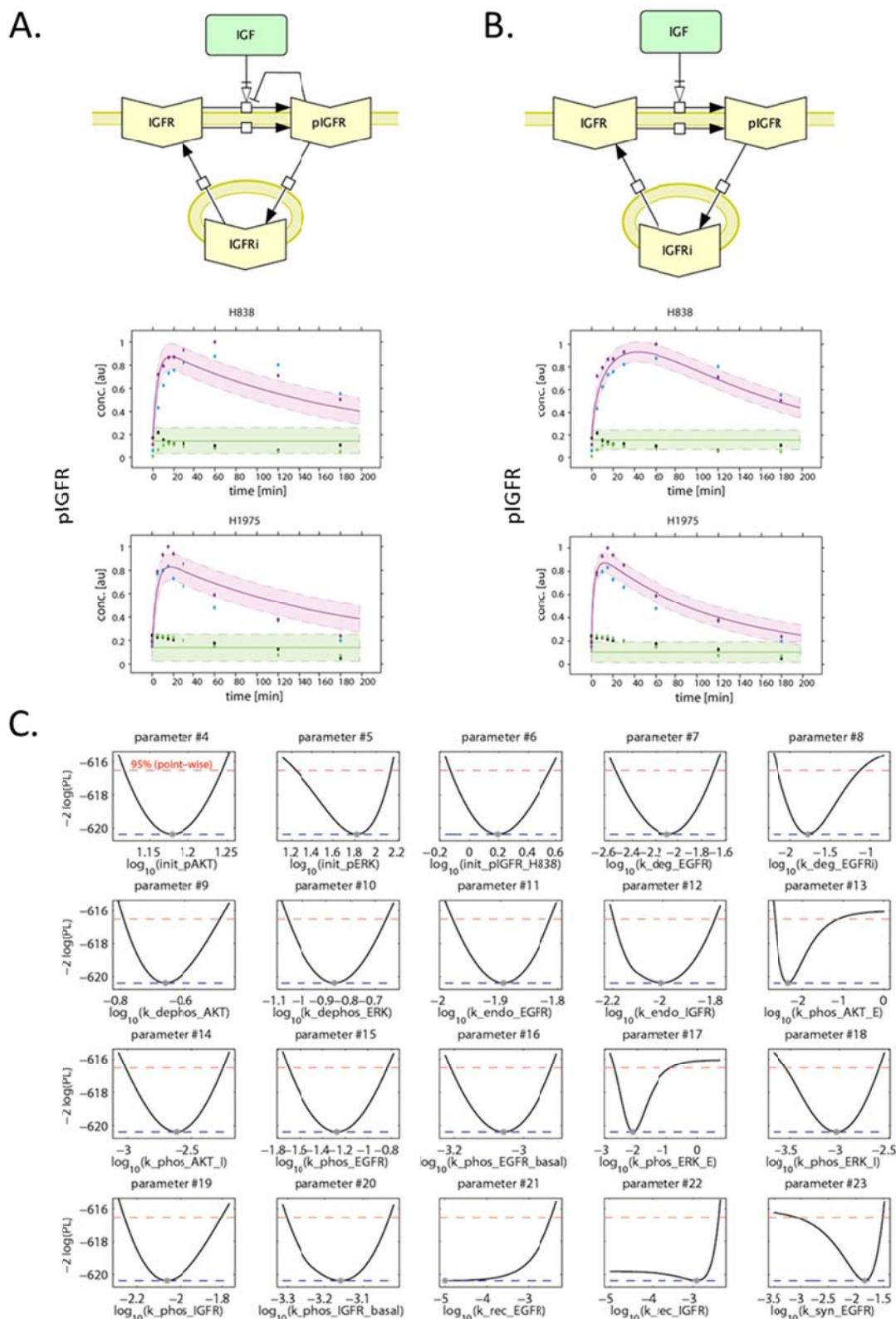
Figure 24: Adaptation of the IGF-1R pathway model. (A) Top: existing pathway model. Bottom: Model fits for IGFR activation for H838 and H1975 data. (B). Top: new model topology with added auto-inhibitory loop from the phosphorylated IGF-1R. Bottom: new model for IGFR activation fits for H838 and H1975 data. (C) Parameter profile likelihood plots for the updated model. Shown are the PLE plots for all biological

parameters. PLEs for scaling factors and standard deviations are fully identifiable and omitted for clarity. Red line denotes 95% confidence interval. Blue line denotes the minimal log likelihood.

4.4 Quantitative measurement of 2D lateral migration and 3D invasion of NSCLC cells

Pathway models can lead to important insights into the dynamic behavior of therapeutically relevant targets. Due to the complexity of cell signaling though, often what presented itself as a promising effect on the pathway level fails to affect the cells in their functional behavior. One of the overarching goals of the LungSys initiative is the establishment of multiscale models to connect pathway activation dynamics and gene expression changes in response to growth factor stimulation with cellular functions like proliferation and migration. With a first usable pathway model in place, I established functional assays to generate phenotypical data to connect the model with meaningful biology.

4.4.1 Establishing a 2D lateral migration assay and proof of principle

In order to generate reproducible quantitative and time resolved migration data, a 2D-migration assay using IBIDI inserts was established. Together with the group of Dr. F. Matthäus, we developed a novel semi-automated evaluation algorithm that yields a variety of parameters from life-cell imaging data, which actively migrate in defined cell-free areas. These parameters include:

- Density distribution of cells measured from nuclear staining
- Dynamic Migration speeds of the whole population
- Directionality of migration: perpendicular to the gap *vs* parallel to the gap, wich can be correlated to directional *vs* random movement

As proof of principle for this approach, the knockdown of *FBP interacting repressor* (FIR), a transcriptional repressor that has been implied in NSCLC migration, was tested. For this, Calu-1 NSCLC cells were selected, since these cells do not respond with reduced proliferation upon FIR silencing. An exemplary picture for the efficient reduction of migration upon knockdown of FIR in Calu-1 cells is shown in Figure 25. Cells (control, nonsense siRNA, and FIR-specific siRNA) were seeded in IBIDI inserts and subsequently monitored using live cell imaging after removing the insert. Figure 25 shows exemplary phase contrast and HOECHT staining images at the start of live cell imaging and after 30 h. This single time point analysis yielded a first observation: the untransfected control as well

as the cells transfected with nonsense siRNA close the gap, whereas the cells treated with FIR siRNA failed to do so.

Quantitative analysis over the complete image stacks (20 sequential images) captured the dynamic properties of this migration phenotype as shown in Figure 26. Plotting the cell density over space and time revealed that control cells closed the gap after approximately 15 h (Figure 26A). In contrast, cells with reduced FIR levels exhibited severely reduced migration, and had not yet closed the gap after 30 h. Effects on cell viability remained not significant (data not shown).

Kymographs of cell velocities demonstrated that control cells (i.e. untreated and nonsense siRNA-transfected cells) showed strong directional migration into the gap area (Figure 26B) with highest speeds at the front and a strong activation for about 20 h. In cells with FIR inhibition, speed was significantly reduced overall. After 20 h no perpendicular migration was detectable. Speed dynamics of cells showed initial acceleration and subsequent deceleration of migration in the control conditions (Figure 26C). In contrast, FIR silencing significantly reduced the speeds and shortened the acceleration phase. Also the onset of gap closure was significantly delayed (controls: 15-27 h; FIR inhibition: 38-65 h). Averaging over space and time shows an overall reduction of speeds to about 50% after FIR inhibition. Figure 26E illustrates that the observed reduction in speeds also included a reduction of the relative velocity component perpendicular to the gap compared to movement in parallel to the gap. This indicates that treatment affects the coordinated migration towards the gap in particular.

In summary, in this proof of principle, the quantitative PIV approach illustrates that FIR drives coordinated and directional movement of cell groups in all phases of 2D migration.
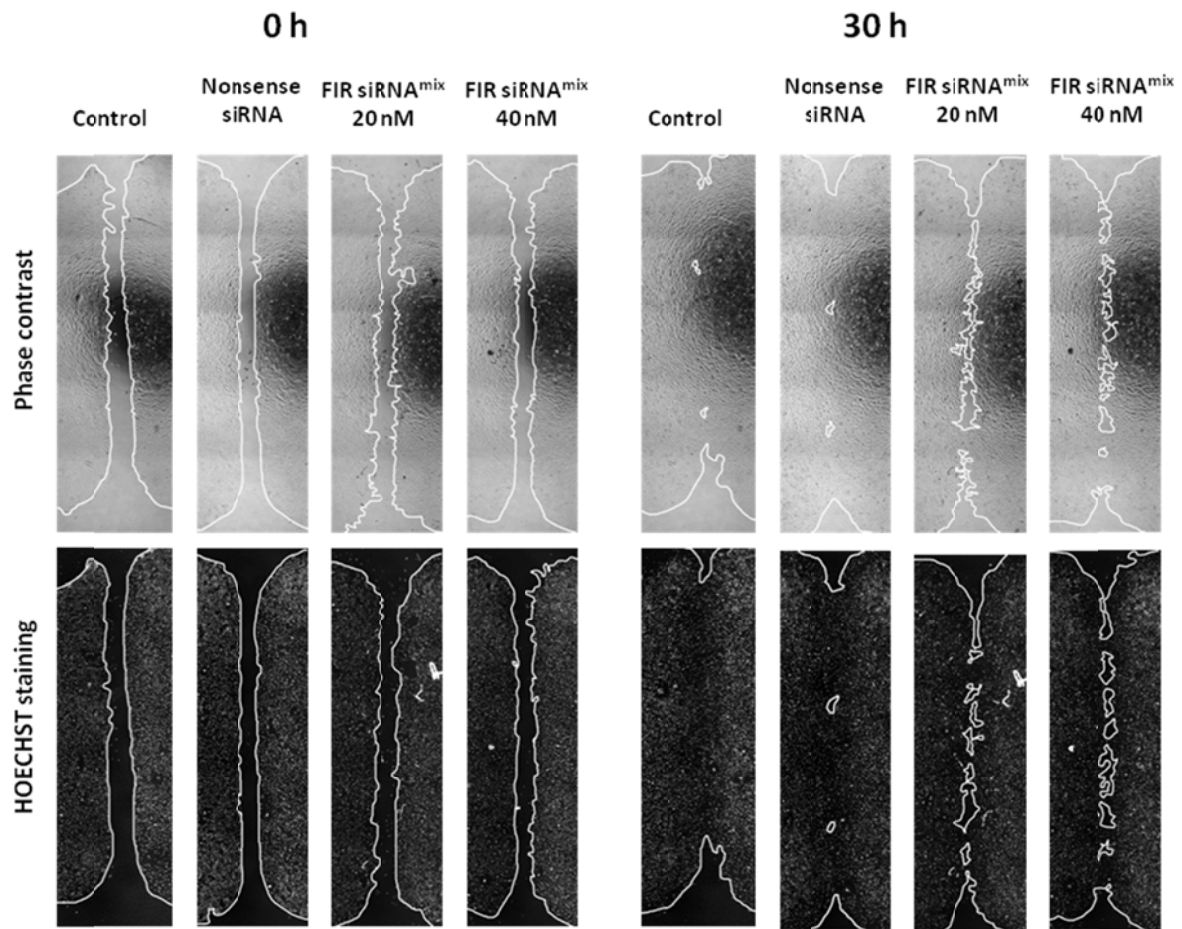
Figure 25: Lateral migration of Calu-1cells after FIR siRNA knockdown and in control cells. Shown are phase contrast and HOECHST staining images for the untransfected control, the nonsense siRNA control, and the gene-specific knockdown with 20 nM and 40 nM of FIR siRNA at 0 h (left) and after 30 h (right). The white contour denotes the edges of the cell populations.
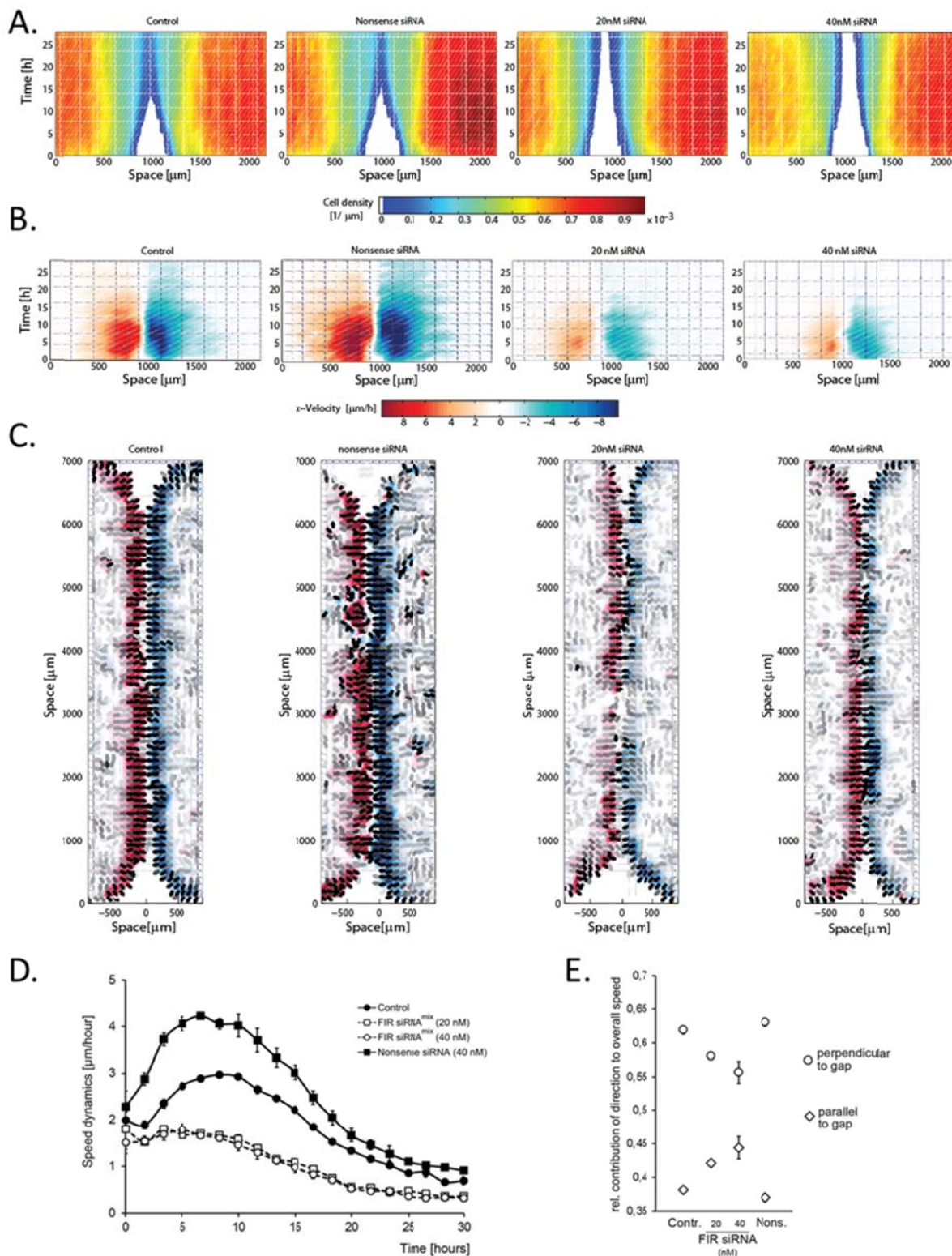
Figure 26: Quantitative analysis of directional NSCLC motion after FIR silencing using PIV. Migration of Calu-1 cells transfected with nonsense siRNA, 20 nM, and 40 nM of FIR siRNA as well as untransfected control cells were analyzed using time-lapse microscopy for 30 h (1 picture/90 min) and HOECHST staining. (A) Cell density kymographs obtained from image segmentation. Color indicates cell density (red: high, blue: low, white: cell-free areas). While the gap closes after about 15 h in untreated cells, FIR strongly reduces migration and impairs gap closure. (B) Cell velocity kymographs. Color indicates speed (red: right, blue: left, with more intensive colors indicating larger displacements) (C) Velocity field obtained by PIV at early time of gap closure (exemplarily frame 5 is shown). Arrows indicate collective displacement of cell

clusters. Color denotes absolute displacements (red: right, blue: left, with more intensive colors indicating larger displacements) in x-direction (perpendicular to the gap). (D) Speed dynamics as a function of time (absolute velocities are averaged over the entire frame) show initial acceleration, then deceleration. The maximum and overall speed is reduced by FIR. (E) Relative velocity components horizontal and perpendicular to the gap. FIR affects in particular directedness of motion into the gap.

4.4.2 Establishing a 3D spheroid invasion/migration model and proof of principle

In vivo, tumor cells are subjected to conditions that are much more complex than 2D migration assays can provide *in vitro*, especially with regard to extracellular matrix components. To supplement the results of 2D migration assays with a more sophisticated cell-culture model that more closely resembles the *in vivo* situation, 3D cell-culture models have been developed. Here, a 3D spheroid model of NSCLC cell invasion capable of providing data for multiscale modeling was established. To this end I used the hanging-drop approach and an analysis tool, which was developed with the group of Dr. D. Drasdo. This software allows the quantitative description of the following parameters from brightfield projection image stacks recorded *via* live cell imaging:

- Total area occupied by cells
- Area of sprouts, which stands for the area occupied by cells that moved out of the central spheroid body
- Number of detached cells, which describes the number of cells that have moved so far out of the spheroid that they have lost connection to the bulk of cells
- Radius of gyration, which measures the distance that all cells (detached or not) moved from the spheroid bulk

As proof of principle for this spheroid generation and evaluation using the newly developed analysis algorithms, the FIR knockdown model was applied.

After successful establishment of Calu-1 spheroids that keep coherency with cells of all conditions (untreated, nonsense siRNA, and FIR-specific siRNA), spheroids with a size of 500 cells/spheroid were transferred in a collagen I matrix (Figure 27). The lower row in Figure 14 shows the last frame of each condition after 72h of life-cell imaging, illustrating that knockdown of FIR has an impact on cell invasion in this specific collagen matrix. However, as in the 2D IBIDI migration system, endpoint analysis lacked the temporal resolution to investigate the dynamics of the invasion/migration phenotype.
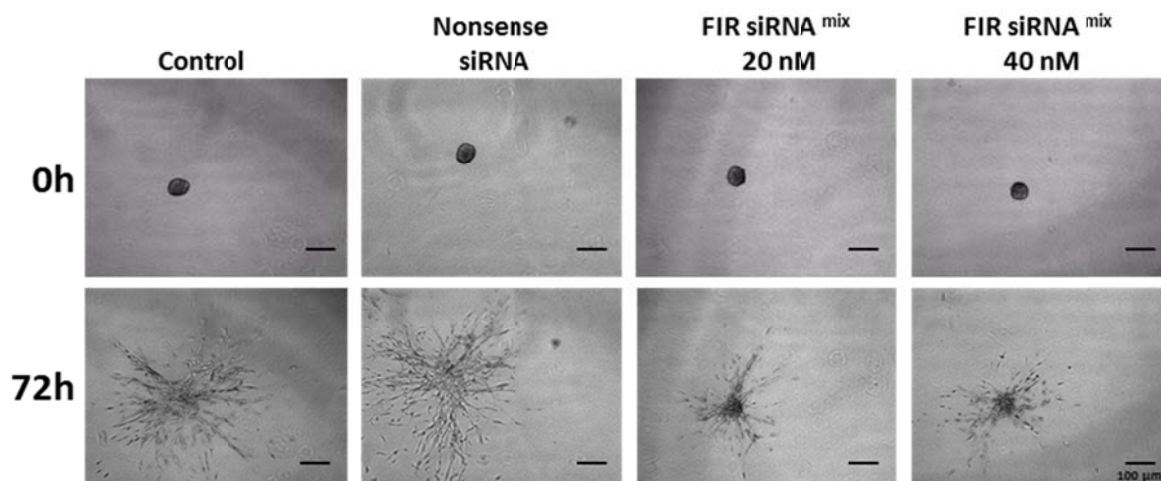
Figure 27: Bright field images of Calu-1 spheroids after FIR siRNA-mediated knockdown in 4x magnification. Spheroids were generated for 48 h using the hanging-drop method. Upper row: spheroids imaged directly after transfer into collagen I matrix. Lower row: Same spheroids after 72 h of live-cell imaging. Scale bar represents 100 μm.

Thus, we employed the novel semi-automated analysis tool to evaluate the growth pattern of at least 5 spheroids for each condition over 72 h, with Figure 28 summarizing the results. Figure 28 A shows representative output images from the software analysis after invasion/migration for 36 h after collagen embedding. The red circles define the central spheroid bodies, the green outline the invading cells in both sprouts as well as detached cells. Total Area Figure 28 B, area of sprouts Figure 28 C and radius of gyration, which indicates the maximum distance cells move away from the center of mass Figure 28 E, show a clear significant and dose dependent reduction under FIR knockdown compared to the control conditions. Total area (i.e. the area covered by cells of both the spheroid body and the sprouting cells) showed strong increases in both control conditions from 20 h until 72 h, with final areas of 6.5 μm² and 2.5 μm² for NTC and KO respectively. Knockdown of FIR reduced this dose dependently to below 2 μm² for 20 nM of siRNA and below 1 μm² for 40 nM of siRNA. The area of sprouts (i.e. the area covered by cells outside of the main spheroid body, but still attached to it) showed the same behavior with the controls growing to 4 μm² and 3 μm² for NTC and KO respectively, and the knockdowns reducing the growth and ending at 1 μm² and 0.5 μm² for 20 nM and 40 nM of siRNA respectively. The radius of gyration (i.e. the farthest distance that cells migrated out of the spheroid, detached or not) also shows a similar behavior. NTC and KO show the largest radius with 425 μm and 400 μm respectively. FIR knockdown reduced this to 250 μm and 200 μm, for 20 nM and 40 nM. The dynamics of all three parameters indicates that FIR may support migration and invasion of NSCLC cells in collagen I matrices. Interestingly, all three of the parameters show an exponential increase in the controls until about 50 h, where the curves seem to switch to a

more linear growth. This shows the value of continuous analysis of 3D invasion dynamics, as this effect would be lost with traditional snapshot evaluation. The number of detached cells Figure 28 D, although less clearly significant, is also reduced from ca. 70 cells/spheroid in the controls to 50 and 20 under FIR knockdown with 20 nM and 40 nM respectively. This reduction indicates that FIR may support separation and detachment of NSCLC cells from the primary tumor mass.
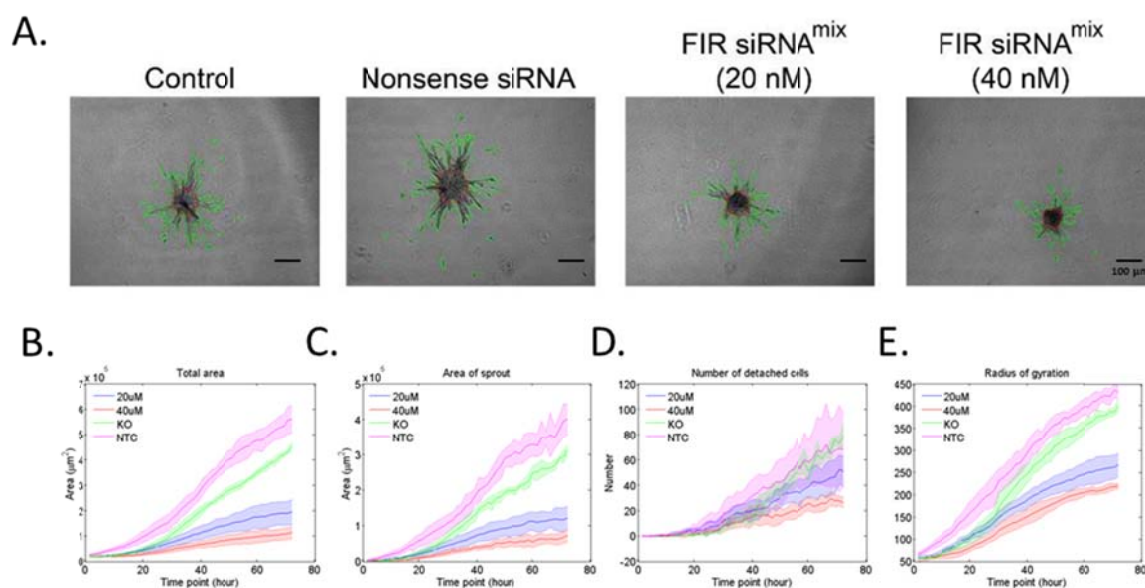
Figure 28: Analysis of time-resolved growth pattern of NSCLC spheroids (500 cells/spheroid) with and without FIR silencing. At least 5 live cell imaging stacks from 72 h were analyzed. KO: untransfected control; NTC: non-target control, nonsense siRNA; 20 nM/40 nM: cells treated with 20 nM or 40 nM of FIR siRNA. (A) Representative pictures of spheroid growth 36 h after transfer in a collagen I/methocel matrix in 4x magnification. Red circle defines the spheroid "body", while the green contour denotes the sprouts and detached cells. (B) Total pixel area occupied by cell mass. (C) Area of sprouts (cells moving out of the spheroid body). (D) Number of detached cells. (E) The radius of gyration, which represents a correlate for tumor cell spread. Scale bar represents 100 μm.

In summary, the novel evaluation algorithm is able to define even small differences in the process of tumor cell invasion, tumor cell separation, and spheroid growth in a quantitative and time-resolved manner.

4.4.3 Effects of IGF-1 and EGF stimulation on NSCLC cell proliferation and migration

As introduced in the beginning of chapter 4.4, one of the central tasks in the project was linking pathway data to biological function in multi scale models. In order to connect the observed pathway activation effects of stimulation with IGF-1, EGF and both factors with functional responses in H838 and H1975 cells, the impact of these treatments on proliferation and migration was investigated in both cell lines. Proliferation of H838 and H1975 cells and migration of H1975 cell was assessed using the CellTiter-Blue Assay after stimulation with 50 ng/ml of EGF (green) and IGF-1 (blue) in single treatment and double

stimulation (violet), at 24 h, 48 h, and 72 h after stimulation. In Figure 29 A/B the resulting proliferation curves are shown.

Figure 29: Effects of IGF-1, EGF and double stimulation on H838 and H1975 cell proliferation and migration. Cells were treated with 50 ng/ml of IGF-1 (blue), 50 ng/ml of EGF (green), and double stimulation with 50 ng/ml of IGF-1 and 50 ng/ml of EGF (violet) over 72 h. ø (grey): Starvation control, FCS (black) cells supplied with full medium after starvation. (A) Proliferation of H838 cells measured with the CellTiter-Blue assay. (B) Proliferation of H1975 cells measured with the CellTiter-Blue assay. (C) Migration speeds for H1975 cells.

Supplying the cells with FCS resulted in strong proliferation in both cell lines, proving that the cells were still susceptible to growth stimuli after starvation. Surprisingly, none of the treatments resulted in a significant increase of proliferation in both H838 and H1975 cells. Investigation of 2D migration in H1975 yielded similar results: cells showed strong migration under FCS, whereas neither EGF nor IGF-1 or double treatment showed an increase over the reduced migration in the control with starvation medium (Figure 29 C). H838 cells lost all migratory capacity under starvation conditions and were thus not further considered for migration experiments.

Investigation of 3D migration/invasion behavior in H1975 spheroids further confirmed the effects seen in proliferation and 2D migration assays. Manual evaluation of sprouting length revealed that stimulation with 50 ng/ml IGF, 50 ng/ml EGF, and double stimulation did not influence sprouting behavior compared to the unstimulated control. Interestingly, in the 3D setting, supplying the cells with FCS lead to a marked reduction of sprouting (Figure 30).

H838 cells did not form coherent spheroids, and as such were not considered for 3D migration/invasion.
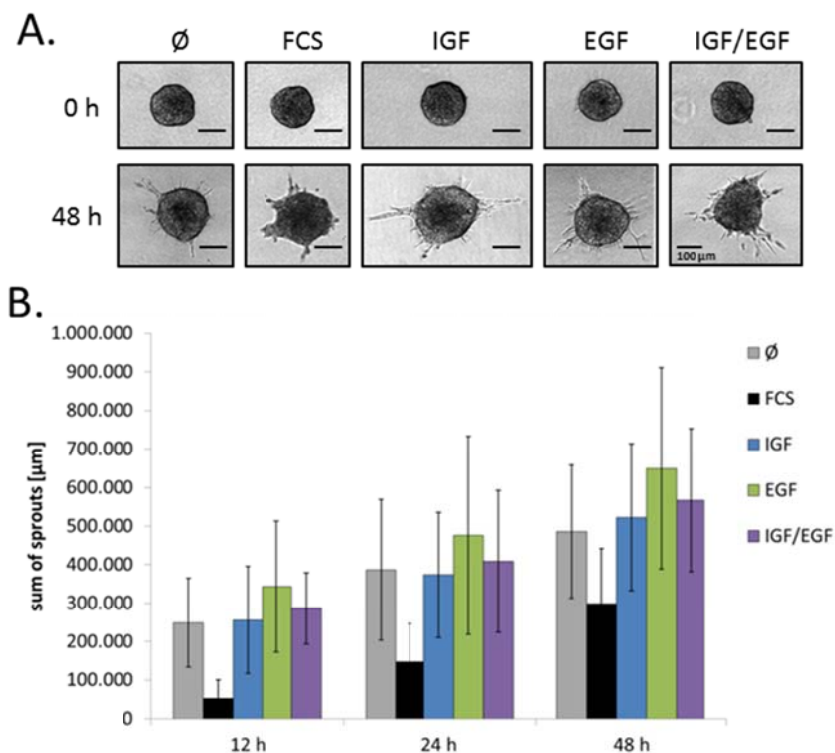
Figure 30: 3D spheroid invasion assay of H1975 cells after stimulation with IGF-1, EGF and double stimulation. Spheroids were treated with 50 ng/ml of IGF-1 (blue), 50 ng/ml of EGF (green) and double stimulation (violet). Ø (grey): Starvation control with medium without FCS, FCS (black) cells supplied with full medium. Initial spheroids were generated with 2000 cells/drop. (A) Exemplary brightfield images of a single spheroid for each condition at the start of imaging (0 h) and after 24 h in 4x magnification. (B) Results of manual evaluation of sprouting (sum of sprouts). Given is the mean of at least 10 spheroids per condition.

In summary, none of the diverse functional test performed resulted in detectable functional effects on cell behavior, despite the clear effects of IGF-1 and EGF stimulation observed on the pathway activation level.

4.4.4 Functional effects of inhibition of IGF-1R and EGFR

Since growth factor stimulation after starvation did not yield any biological effects, it stands to reason that the signaling along the EGFR and IGF-1R pathways is part of a more complex signaling network in these NSCLC cell lines. As such, the cells are missing input signals, which are essential for the proper induction of an IGF-1/EGF-mediated response. This lead to the working hypothesis, that perturbation of the EGFR or IGF-1R axes might be better suited to explain the biological impact of these pathways with regard to proliferation and migration. Accordingly, selective small inhibitory molecules (TKIs, Table 18) were used to

eliminate the specific signaling pathways under full medium conditions for further analysis of proliferation and migration.

Table 18: Overview over the TKIs used in functional assays.

Substance	Specificity	Mode of action
Picropodophyllin	IGF-1R	Blocking of IGF-1R autophosphorylation
CAS-879127-07-8	EGFR (WT, L858R)	ATP competitive inhibition of EGFR phosphorylation
Erlotinib	EGFR (WT, L858R)	Reversible blocking of ATP binding
Afatinib	EGFR (WT, L858R, T790M) / HER2)	Irreversible blocking of ATP binding

Wide ranges of concentrations were used to investigate dose response to the TKIs and find useful inhibitor concentrations (e.g. concentrations that show functional effects without killing the cells outright). All inhibitors lead to a reduction of activation of the ERK and AKT downstream pathway components (data not shown).

Proliferation

In H838 cells, this inhibitor treatment resulted in clear dose-dependent effects on both proliferation (measured through viability) and cell death (measured through the amount of free DNA). Figure 31 shows the resultant cell numbers after 24 h, 48 h, and 72h after inhibition with *Picropodophyllin* (PPP) and CAS-879127-07-8.

- Inhibition of IGF-1R with 10 µM of PPP resulted in the complete death of all cells. Lower doses from 1 µM to 1 nM showed reduced proliferation after 48 h while not affecting cell death.
- Inhibition of EGFR with the three TKIs showed similar effects. CAS-879127-07-8 completely killed the cells in doses upwards of 100 nM accompanied by reduced proliferation. Doses of 10 nM and 1 nM diminished the proliferation dose dependently, with no significant effects on cell death. In contrast, H838 cells showed less sensitivity to Afatinib and Erlotinib. Treatment with 10 µM of Afatinib led to a complete inhibition of proliferation with only minor increases in cell death over the control. Lower concentrations (1 µM and 100 nM) slightly reduced proliferation with no effect on cell

death. Increasing the concentration to 50 µM and above killed the cells after 24 h (data not shown).
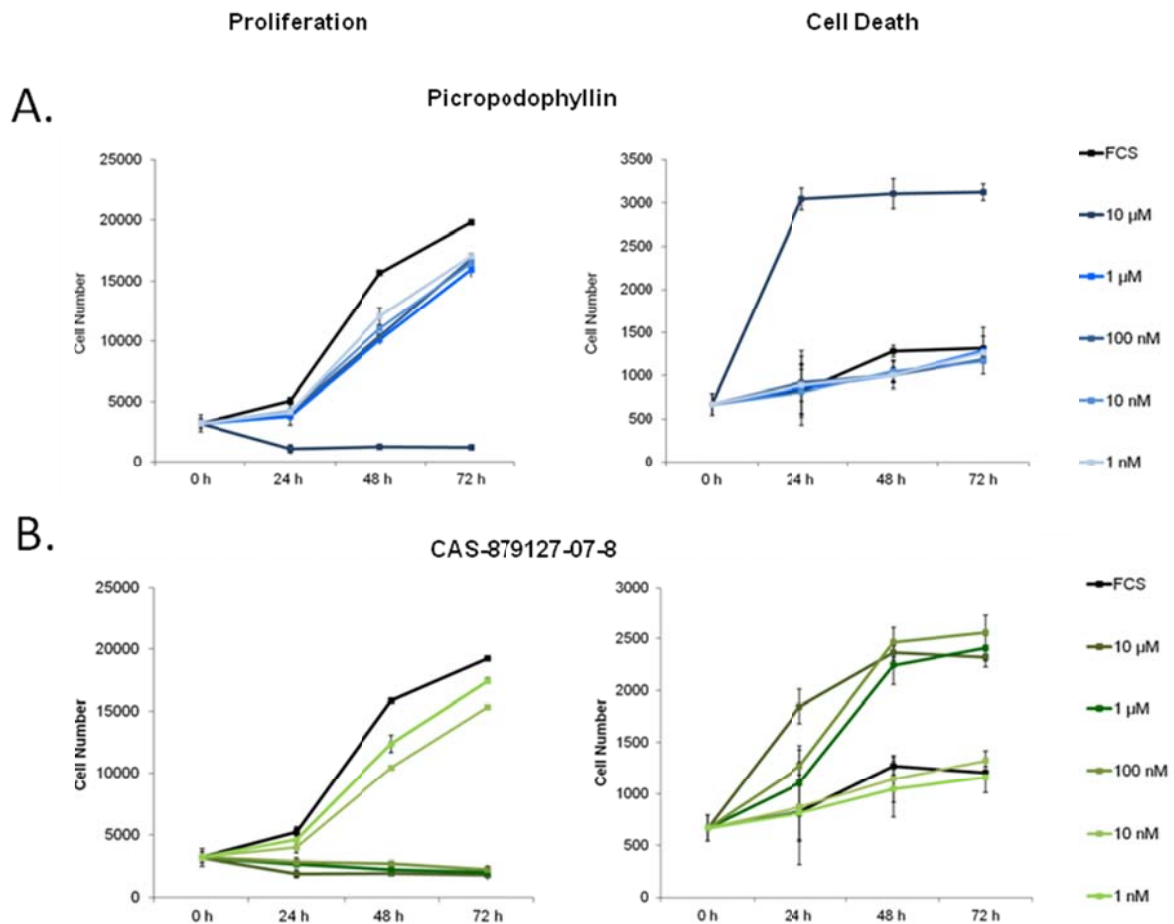
Figure 31: Biological effects of IGF1-R and EGFR inhibition on H838 cell death and proliferation. Cell death and proliferation were measured sequentially in the same wells. (A) Left: Dose-dependent effects of IGF-1R inhibitor Picropodophyllin on proliferation. Right: Dose-dependent effects of IGF-1R inhibitor Picropodophyllin on cell death. (B) Left: Dose-dependent effects of EGFR inhibitor CAS 879127-07-8 on proliferation. Right: Dose-dependent effects of EGFR inhibitors CAS 879127-07-8 on cell death.

In H1975 cells, the inhibition of both receptors with the same inhibitors yielded comparable results. Although, compared to the results in H838, H1975 cells showed a more even distribution in reduction of cell proliferation and increased cell death with the concentrations used. Figure 31 shows the resultant cell numbers after 24, 48, and 72 h after inhibition with *Picropodophyllin* (PPP) and CAS-879127-07-8.

- Concerning IGF-1R inhibition, the treatment with 10 µM of PPP resulted in the complete killing of cells after 24 h. Lower concentrations showed a reduced proliferation after 24 h. The distribution and dose effects of the different concentrations became apparent after 48 h, where the curves for 1 µM, 100 nM, 10 nM and 1nM fan out. A similar behavior can be seen in the cell death analysis, although the separation of the curves is

less pronounced, with 1 µM revealing a higher number of dead cells after 48 h and thus separating from the cluster of lower concentrations that still show a small increase over the control (Figure 32A).

- Inhibition of EGFR through CAS-879127-07-8 shows a comparable effect. Treatment with 10 µM resulted in declining cell numbers until 72 h. Correspondingly, the number of apoptotic cells increased. Lower doses again led to a differentiated response in proliferation, with 1 µM leading to slightly decreased cell numbers, 100 nM to a more or less stable amount of cells and 10 nM as well as 1 nM to a slightly proliferative phenotype that keeps up with the FCS control at 24 h. After 48 h the reduced proliferation compared to FCS becomes apparent. For the cell death numbers, the doses lower than 10 µM cluster together and only show increased cell death after 48 h and 72 h. H1975 cells showed reduced sensitivity to Afatinib and Erlotinib compared to H838 (data not shown).
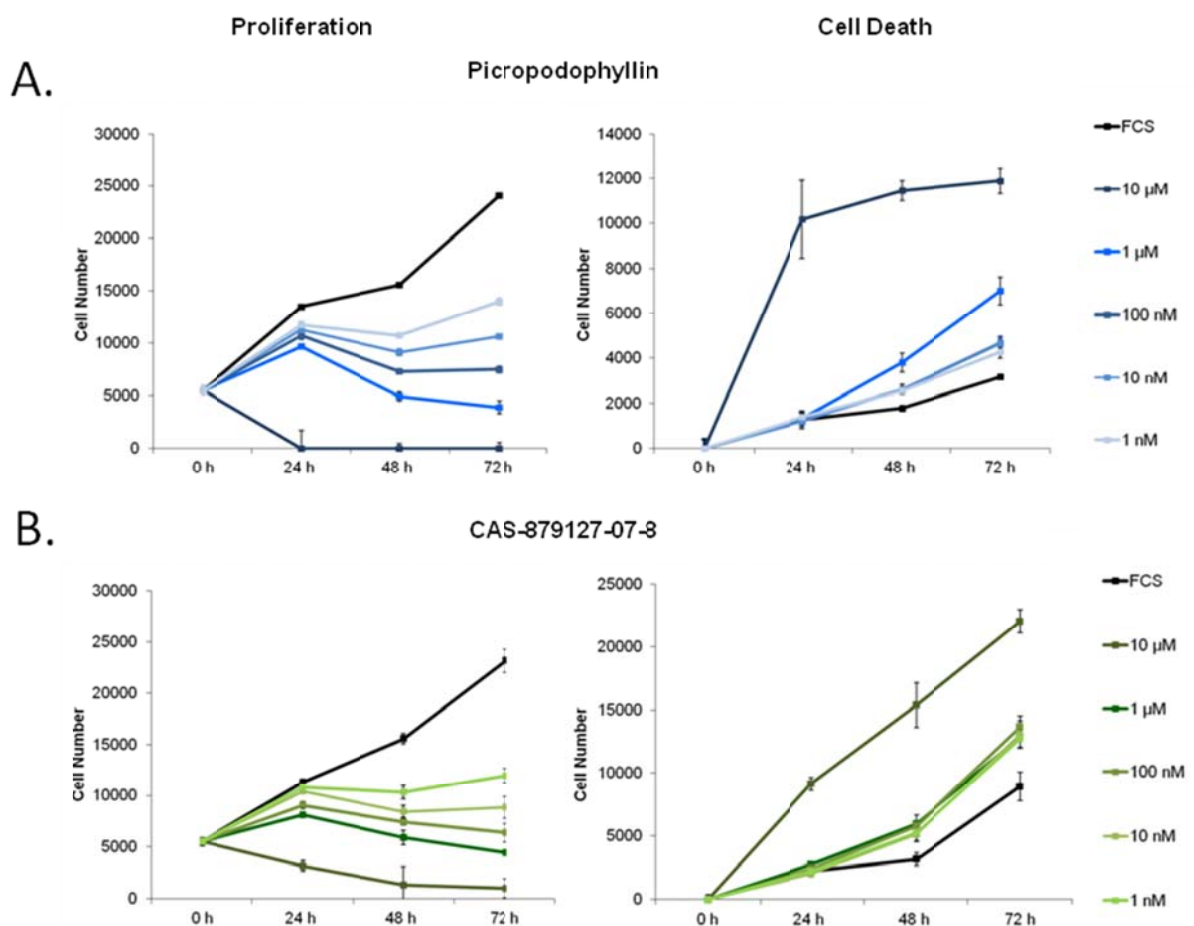
Figure 32: Proliferation and cell death of H1975 cells after inhibition of IGF-1R and EGFR. Cell death and proliferation were measured sequentially in the same wells. (A) Left: Dose dependency of IGF-1R inhibition with Picropodophyllin on proliferation. Right: Dose dependency of IGF-1R inhibition with IGF-1R inhibitor Picropodophyllin on cell death. (B) Left: Dose dependency of EGFR inhibition with CAS 879127-07-8 on proliferation. Right: Dose dependency of EGFR inhibition with CAS 879127-07-8 on cell death.

Migration

After having shown the dose-dependent effect of IGF-1R and EGFR inhibition in both H838 and H1975 cells, I continued to investigate the effects of the receptor inhibition with PPP and CAS-879127-07-8 on 2D migration in H1975 cells as shown in Figure 33. Inhibition of both receptors results in reduced migration compared to the FCS control. In order to exclude effects of the TKIs on cell viability, inhibitor concentrations that do not kill the cells were chosen as determined from Figure 32. Reduction of migration was less pronounced with PPP, than with CAS-879127-07-8. While 1 μM of PPP reduced both maximum speed and duration of migration, treatment with 100 nM moderately decreased the maximum speed, but significantly affected the duration the cells migrated. In contrast, treatment with 10 nM of PPP decreased the max speed more noticeably but did not reduce the duration of migration compared to the FCS control.
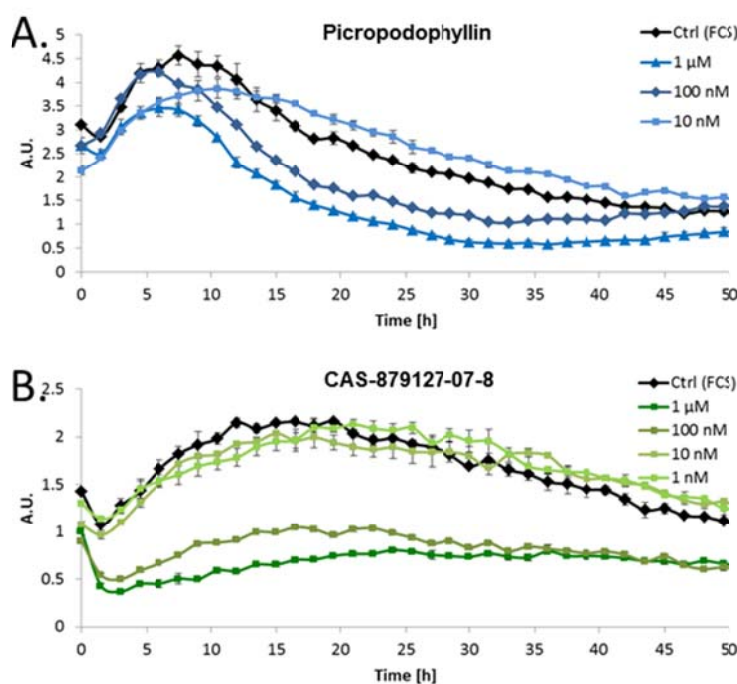
Figure 33: Biological effects of receptor inhibition on H1975 2D migration. Cells were stained with HOECHST and monitored over 50 h with live cell imaging. Images were taken every 90 min and evaluated using PIV. (A) IGF-1R inhibition with different doses of PPP. (B) EGFR inhibition with different doses of CAS-879127-07-

Still, with all three concentrations, the cells showed a comparable migration dynamic as the FCS control. Inhibition of EGFR with CAS-879127-07-8 on the other hand completely abolished migration with a concentration of 1 μM and severely reduced it with 100 nM. Conversely, treatment with 10 nM showed only a very small reduction of max speed, whereas treatment of 1 nM yielded no effect on max speed and migration duration. Similar effects have been observed with Erlotinib and Afatinib, where doses that do not kill the cells

outright (10 µM and 20 µM for Erlotinib, 1 µM and 10µM for Afatinib) show strong reductions in migration as well (data not shown).

Thus, inhibition of IGF-1R and EGFR both affect migration of H1975 NSCLC cells, however, IGF-1R and EGFR signaling seem to affect cell migration differently.

4.4.5 Rescue of the phenotype after inhibition of IGF-1R and EGFR

Having shown that IGF-1R and EGFR inhibition in a full medium context affected both proliferation and migration of NSCLC cells, I further investigated the possibility of rescuing this phenotype by stimulating cells under EGFR inhibition with IGF-1 and *vice versa*.
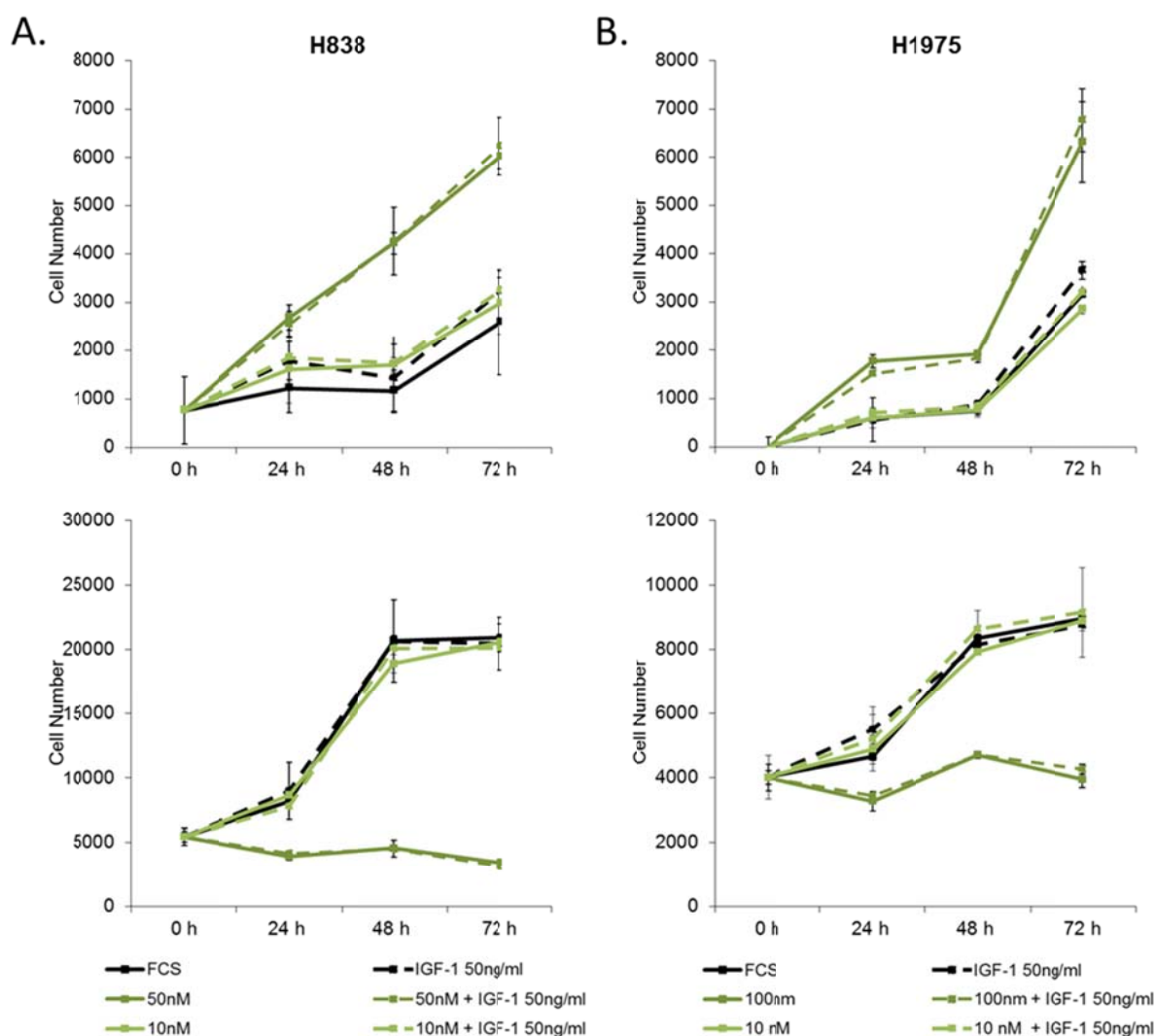
Figure 34: Biological effects on H838 and H1975 cell death and proliferation after TKI-mediated inhibition of EGFR with CAS 879127-07-8 (solid lines) and simultaneous stimulation with IGF-1 (dashed lines). Cell death and proliferation were measured sequentially in the same wells. (A) Results from H838 cells. Top: Rescue effects on cell death. Bottom: Rescue effects on proliferation. (B) Results from H1975 cells. Top: Rescue effects on cell death. Bottom: Rescue effects on proliferation.

Figure 34 exemplarily shows the effects of EGFR inhibition with CAS-879127-07-8 and simultaneous stimulation with 50 ng/ml of IGF-1. As illustrated, stimulating with 50 ng/ml of IGF-1 did not show any rescue of the phenotype, neither with concentrations of the TKI sufficient to abolish proliferation (50 nM of inhibitor in H838, 100 nM of inhibitor in H1975), nor with lower concentrations. In both cases, the curves run completely congruent. Comparable results have been generated for Erlotinib and Afatinib, as well as for IGF-1R inhibition with PPP and simultaneous stimulation with EGF (data not shown). Thus, these data indicate that IGF or EGF cannot compensate the effects induced by the loss of the other pathway with regard to proliferation in the analyzed cell systems.

Since trying to rescue the phenotype after receptor inhibition with stimulation of the other pathway yielded no effect on proliferation of H838 or H1975 cells, I investigated their impact on 2D migration.

Figure 35 shows the resulting speed curves after live-cell imaging and evaluation with PIV. IGF-1R inhibition with 100 nM PPP reduced migration speeds and inhibiting the EGFR with 50 nM of CAS-879127-07-8 led to the expected drastic reduction in migration, confirming previous results (Figure 33). Simultaneous treatment with 50 ng/ml of EGF and 100 nM PPP did not rescue the TKI-induced phenotype, but led to a further reduction in speeds (Figure 35 A). Importantly, supplying simultaneous stimulation with 50 ng/ml of IGF-1, together with 50 nM of CAS-879127-07-8 did show a marked increase in migration speed in a 10 hour timeframe from 5 h to 15 h (Figure 35 B). Migration increased to a maximum of
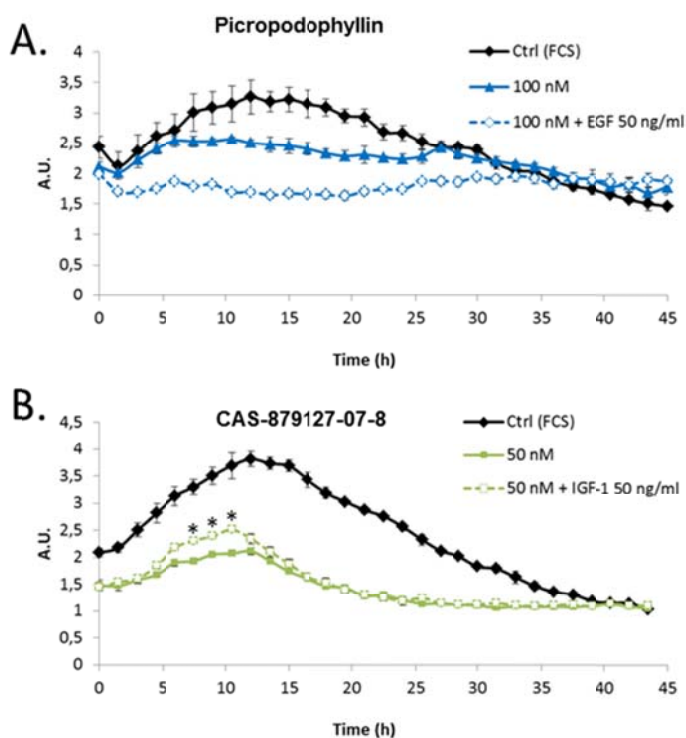
Figure 35: Rescue effects on H1975 2D migration after receptor inhibition and stimulation of the opposite pathway. Cells were stained with HOECHST and monitored over 45 h with live cell imaging. Images were taken every 90 min. (A) IGF-1R inhibition with 100 nM of PPP and simultaneous stimulation with 50 ng/ml of EGF. (B) EGFR inhibition with 50 nM of CAS-879127-07-8, and simultaneous stimulation with 50 ng/ml of IGF-1. Statistical analysis was performed between the conditions with only the inhibitor and the inhibitor plus IGF-1 treatment, using the student's t-test. * denotes significant differences between the means of 3 technical replicates (P value < 0,01)

approximately 10% rescue from roughly 60% to 70% of the speed reached in the untreated control. This finding could be replicated in a second independent experiment.

The functional investigation of the rescue effect of IGF-1 and EGF after EGFR and IGF-1R inhibition respectively, yielded no impact on proliferation of H838 and H9175 cells. While EGF also has no effect on the migration of H1975 cells treated with IGF-1R inhibitor, stimulation with IGF-1 can reduce the effects of EGFR inhibition. Thus a connection of IGF-1 and EGFR signaling could be shown on a functional level.

4.4.6   Effects of IGF-1 and EGF on the transcription level

The results from IGF-1 and EGF-induced IGF-1R and EGFR pathway activation on protein level led to a first usable pathway model, and the functional data from receptor inhibition and rescue experiments indicate that both EGF and IGF-1 can have an influence on proliferation and migration in the analyzed NSCLC cell lines. In order to link pathway activation and phenotype to the transcription of relevant genes, I also investigated the effects of EGF and IGF-1 stimulation on transcript level of IGF-1R and EGFR target genes in H1975 cells. To this end, Affimetrix GeneChip Human Gene 2.0 ST Arrays were hybridized with mRNA from time courses of H1975 cells treated with 50 ng/ml of EGF or 50 ng/ml of IGF-1, as well as unstimulated controls. The resulting expression profiles were pre-processed and GO annotation as well as analysis of differential expression was performed, resulting in ranked lists of significantly regulated genes for each stimulation condition compared to the unstimulated control. Table 19 shows the resulting top 20 ranked genes after EGF stimulation

Table 19: The 20 highest-ranked genes from microarray analysis of H1975 cells after EGF stimulation

Gene symbol	Full name	GO annotation	Function in the cell
CTGF	connectve tissue growth factor	cell-matrix adhesion, FGF receptor signaling pathway, cell migration, lung development	fibronectin binding/integrin binding/IGFR binding/heparin binding/
EGR1	Early growth response protein 1	INF-α signaling pathway, IL-1-mediated signaling pathway, positive regulation of cell death	transcription factor binding/ histone acetyltransferase binding
PTGS2	Prostaglan-din-endo-peroxide synthase 2	positive regulation of cell migration, negative regulation of cell proliferation, VEGF production, FGF production	peroxidase activity, lipid binding, oxidoreductase activity/

GLIPR1	Glioma pathogenesis-related protein 1	cellular lipid metabolic process, small molecule metabolic process	NA
JUN	JUN	TGF beta receptor signaling pathway, SMAD protein import into nucleus, negative regulation of cell proliferation	transcription coactivator activity/Rho GTPase activator /CRE binding/ R-SMAD binding
FOS	FBJ Murine Osteosarcoma Viral Oncogene Homolog	toll-like receptor signaling pathway, DNA methylation, stress-activated MAPK cascade, SMAD protein signal transduction	transcription factor binding, sequence-specific DNA binding
CYR61	Cysteine-rich angiogenic inducer 61	cell proliferation, ECM organization, cell migration, regulation of ERK1 and ERK2 cascade, cell adhesion, cell-cell adhesion	integrin binding, IGFR binding, heparin binding, ECM binding
AREG	Amphiregulin	EGFR signaling pathway, cell-cell signaling, cell proliferation, DNA replication	cytokine activity, growth factor activity
CLDN1	Claudin-1	cell adhesion, cell-cell junction organization	structural molecule activity
DUSP1	Dual specificity protein phosphatase 1	inactivation of MAPK activity, regulation of apoptotic process /	MAP kinase tyrosine/ serine/ threonine phosphatase activity
F3	coagulation factor III	PDGF receptor signaling pathway, cell migration, positive chemotaxis	protease binding, phospholipid binding
IL8	Interleukin-8	cell-cycle arrest, cell proliferation, cell adhesion, response to FGF stimulus, positive chemotaxis, response to IL-1, response to TNF	IL8 receptor binding, chemokine activity, cytokine activity
CEACAM6	Carcinoembryonic antigen-related cell adhesion molecule 6	signal transduction, cell-cell signaling, biological_process	protein binding/molecular_function
TMPRSS11E	transmembrane protease, serine 11E	proteolysis	serine-type peptidase activity/ hydrolase activity
EGR2	Early growth response 2	protein sumoylation, response to insulin stimulus, negative regulation of apoptotic process, cellular response to cAMP	ubiquitin protein ligase binding, HMG box domain binding
CD274	Programmed death-ligand 1 (PD-L1)	immune response, T cell costimulation , positive regulation of IL-10 secretion	protein binding

SERPINE1	SERPINE1	TGF beta-receptor signaling pathway, cell migration, regulation of IL-8 production, negative regulation of cell adhesion, regulation of cell proliferation, ECM organization	protease binding, serine-type endopeptidase inhibitor activity, peptidase inhibitor activity
EDN1	Endothelin 1	cell growth, cell migration, MAP kinase activity, JUN kinase activity, response to TNF	cytokine activity, hormone activity
MCM2	minichromosome maintenance deficient 2	mitotic cell cycle, DNA replication	DNA replication origin binding, histone binding, helicase activity
HBEGF	Heparin-binding EGF-like growth factor	EGFR signaling pathway, FGF receptor signaling pathway, cell growth, cell migration, wound healing, spreading of epidermal cells, protein kinase B signaling cascade	EGFR binding, heparin binding

In order to validate the datasets, the expression of a number of genes from these lists was re-evaluated using real-time PCR. Figure 36 shows examples for EGF regulated genes (CTGF, ranked on 1; AREG, ranked on 10; IL8, ranked on 16), whose dynamic differential expression from the array was reproduced with real-time PCR. Particularly, the dynamics for AREG and IL8 after EGF stimulation could be very well reproduced, with spikes in the first 2 h and subsequently converging signals in the EGF and the control. On the other hand, while the microarray expression of CTGF showed a narrow peak at 2 h, sinking back to base levels at 4 h, the qRT-PCR validation showed a sustained activation from 0.5 until 8 h before dropping back to starting levels and below the control. While the microarray dataset for EGF stimulation could be well reproduced and validated with qRT-PCR, this could not be achieved for the IGF-1 dataset. In light of this, together with the initial finding of the PCA analysis by the group of Dr. F. Matthäus which showed an unexpected shift in the complete time course, the IGF-1 microarray dataset was not considered in further analysis.
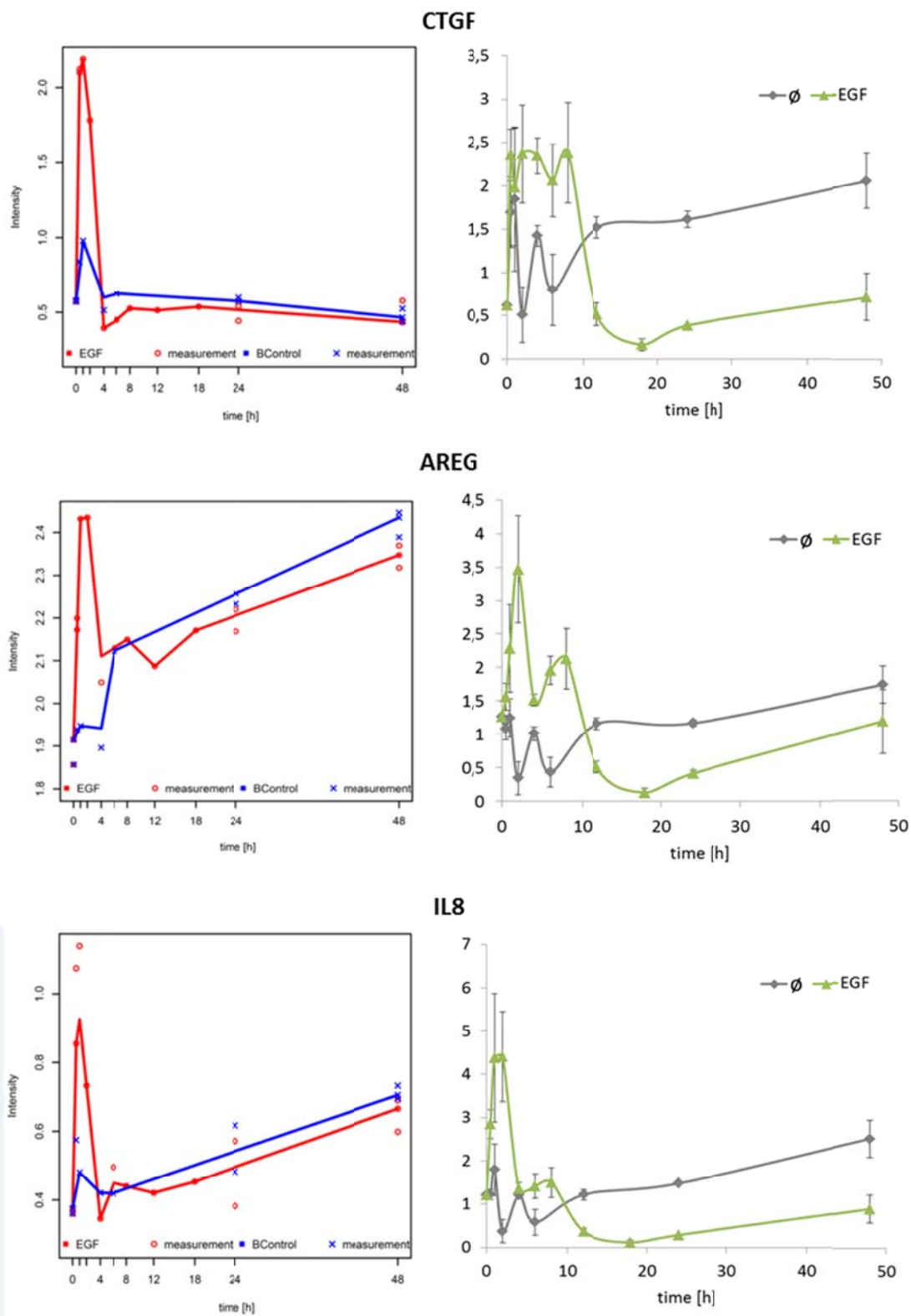
Figure 36: Validation of microarray results from EGF stimulated H1975 cells with qRT-PCR. Left: Result figures from the microarray evaluation after preprocessing, GO annotation and differential expression analysis for treatment with 50 ng/ml of EGF (red) and unstimulated control (blue). Samples were measured in triplicates for 0 h, 24 h, and 48 h, and single samples for all other time points. Right: Results of qRT-PCR validation for treatment with 50 ng/ml EGF (green) and untreated control (Ø, grey), samples were measured in triplicates for all time points.

In summary, the presented data further corroborate the importance of the interaction of EGF and IGF-1 signaling in NSCLC cells. While Western immunoblot and microarray analysis showed activation of signaling pathways after EGF and IGF-1 stimulation, functional assays showed that proliferation and migration in the NSCLC cell lines investigated depend on a more complex signaling network. Interestingly, IGF-1 was able to rescue migration after EGFR inhibition in such a setting.

5 Discussion

The aim of this project was to address two central problems with regards to NSCLC: the evasion of inhibition after IGR-1R and/or EGFR perturbation and the impact of these signaling pathways on the early spread of NSCLC cells. To this end, a systems biology approach was implemented, with the generation of an ODE pathway model from dynamic signaling-pathway activation data with a high temporal resolution. Furthermore, the development and application of partly novel, semi-automated evaluation algorithms for migration and invasion assays was pursued in order to generate quantitative data in high spatial-temporal resolutions that are suitable for the implementation in multi-scale models. Linking these different molecular and cellular scales is of central importance, since it has been shown that the pathway dynamic is crucial for the specific cellular response in the context of complex interconnected signaling networks [126-128].

5.1 Quantitative analysis of NSCLC cell migration

The presented lateral migration approach using IBIDI inserts and PIV evaluation in a semi-automated fashion enables medium-throughput analysis of dynamic collective migration behavior. Traditionally, migration has been evaluated by measuring the areas covered by cells and closing of a gap at distinct times (e.g. 24, 48 and 72 h) after scratching a confluent monolayer of cells with a pipette tip (the so-called scratch-assay).[129] In contrast to these scratches, IBIDI inserts produce gaps of a defined 500 µm width with high reproducibility, which is advantageous for quantitative modeling. Furthermore, for automated live cell imaging approaches, using a 24-well plate with one IBIDI chamber in each well increases the number of testable samples compared to manual scratching, which is only feasible in up to a plate size of 12-well plates due to handling issues. While manual imaging has advantages with regard to low technical prerequisites and sample quantity, it is severely limited with regards to temporal resolution and measurable parameters: few time points can be feasibly imaged and only a snapshot evaluation of area coverage can be performed. Therefore, information on dynamic changes in speed and cell morphology cannot be monitored.

With the application of the PIV algorithm presented here, which was developed in cooperation with the Matthäus lab, the following important parameters for lateral migration can be obtained: cell density, migration speeds, and directionality of migration (i.e. perpendicular vs. parallel to the gap, which can be correlated to directional vs. random movement) as well as, due to the high temporal resolution, acceleration and deceleration dynamics. The importance of this approach is supported by the work of others illustrating that PIV approaches can be utilized on migration questions. Petitjean et al. investigated the differences in migratory behavior between two kidney-cell models using a similar scratch migration approach, showing that MDCK cells migrate with higher velocity than NRK cells.[130] Czirok et al. examined collective cell streams in confluent keratinocyte cell layers, showing the relevance of calcium-dependent cell-adhesion for the phenotype of those streams. [131]

As proof of principle, the effect of FIR-knockdown in NSCLC cells was shown to decrease cell motility. In particular, due to the distinct spatial information gathered through the PIV algorithm, directed movement into the gap could be differentiated from "random" movement perpendicular to the gap. Thus, not only the decrease in motility, but the specific reduction in directional migration could be demonstrated after silencing of FIR.

More importantly, the relevance of the continuous observation with low time intervals (i.e. 90 min or less between single frames) becomes apparent, as the moderate but statistically

significant rescue effect of IGF-1 after specific silencing of EGFR in NSCLC cells was detectable only between 5 and 15 hours of the time course, which would have been lost using traditional evaluation approaches (Figure 35). The continuous observation also enables a better correlation of migratory phenotypes with molecular events in the cell, like pathway activation for short-term responses and gene expression analysis for longer-term effectors. Another advantage of the technique presented here is it's general applicability for image stacks recorded with any live-cell imaging setup. While the ability to image nuclear stains (e.g. using HOECHST dye) is generally of advantage and necessary for the analysis of cell density distributions, PIV-based speed analysis also works on bright field images, further reducing technical hurdles.

Finally, the quantitative nature and high spatio-temporal resolution make these datasets ideal for modeling purposes. Indeed, modeling of 2D migration has been an active field in recent years.[132] Models that concentrate on single events in the motility cycle have been built, for example describing the generation of protrusions on the leading edge of cells.[133] In contrast, *individual based models* (IBM, *also called agent-based models*, ABM) and continuum models consider migration on a holistic scale. IBMs can either be lattice based, meaning cell positions are restricted to discrete points on a lattice[134] or off-lattice where cells can occupy any position in a continuous space.[135] Due to the continuity of space, off-lattice models can describe the mechanical interaction of the cells more realistically and capture cell-cell interactions more accurately.[135] Where IBMs model low numbers of cells with parameters describing single cells, continuum models employ a top-down approach. As such, they describe larger cell populations with the dynamics of local parameter means. The model, which is currently developed by the Matthäus group (building on previous work from Middleton et al.[136]), connects both approaches and aims to extrapolate individual cell properties from the collective migration datasets.

In conclusion, combining the PIV-based evaluation algorithm with the experimental 24-well IBIDI insert approach represents a quantitative, fast, and reliable method to generate migration data with a sufficient spatio-temporal resolution to enable sophisticated modeling that is achievable using standard live-cell imaging setups.

5.2 Quantitative 3D analysis of NSCLC cell invasion

Traditional 2D monolayer cell culture has served well as the basis for data generation in biological science and continues to do so as also evident in the work presented here. However, the plastic and glass surfaces commonly used in cell culture cannot resemble the cellular environment in organisms and even with coated cell dishes, tissue-specific architecture, mechanical, and biochemical cues as well as 3D cell-cell communications are lost under these simplified conditions.

Experiments in living animals or ex vivo whole organ technologies are usually employed to correct for these limitations. However, the heterogeneity and low transparency of animal experiments and organotypic approaches is challenging with regard to imaging and data collection. Additionally, the time requirements and experimental costs increase exponentially when working with these more sophisticated approaches, and the difference between the fundamental human and the animal setting remains a central problem.[137]

Thus, in vitro 3D cell-culture models can fulfill an important function, bridging the gap between culture dish and living organism. A multitude of 3D cell-culture techniques have been established during the last decades, with varying grades of complexity.[138,139] Among these, 3D spheroids hold a special position with regard to resemblance to real tumors, reproducibility and ease of handling. Originally employed in experimental radiotherapy, photodynamic treatment and hyperthermia assays, spheroids were adapted to chemotherapy and target-specific approaches, gene therapy, and cell or antibody based immunotherapy.[140,141]
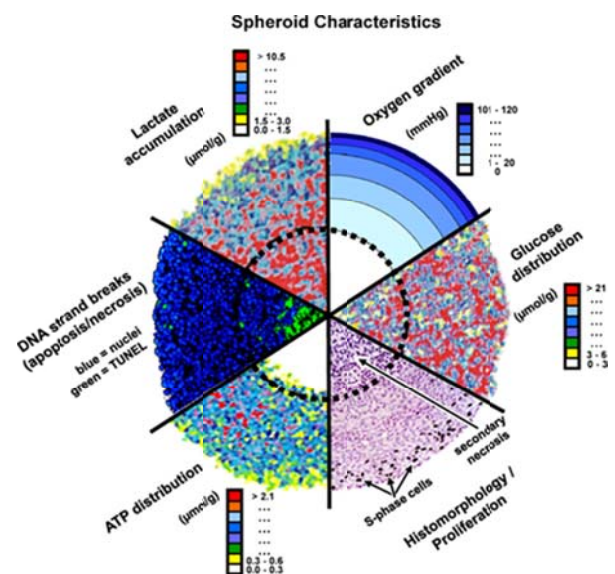

Figure 37: Histomorphological and physiological parameters of spheroids using autoradiography, tunnel assay, bioluminescence imaging, and probing with oxygen microelectrodes. Together these measurements ilustrate the concentric arrangement of spheroids with regard to cell proliferation, viability, and the micromilieu. Modified from Hirschhaeuser et al.[141]

Central to the success of the spheroid system in tumor biology are the histomorphological, functional, and environmental properties, which closely resemble the *in vivo* situation in non-vascular tumors.[141] For example, the distribution of important nutrients like glucose and oxygen decreases along a gradient towards the center of the spheroid. Likewise, metabolic products like lactate and metabolic waste increase along the same axis. Factors like extra-cellular matrix (ECM) and basal membrane production and its dissemination also show a realistic spatial distribution. This results in a spread of living, quiescent, and dead cells that mirrors the actual structure in solid tumor nodules. The second important advantage of this model system compared to other 3D approaches is the relative ease of handling and high reproducibility. In addition, the biological relevance of the spheroid system as a bridging system between 2D cell-culture and *in vivo* models was proven by a number of studies, as reviewed by Breslin et al.[142]

In the work presented here, spheroids from H1975 and Calu-1 NSCLC cells were successfully established using the hanging drop approach.[142] A sprouting assay after embedding spheroids in a collagen-I gel was employed to measure growth of the cell mass and invasion of both cells attached to and cells disassociating from the central mass. Analogous to the 2D migration approach, traditional evaluation of spheroid sprouting and growth involves time intensive manual analysis of relatively small numbers of time points. With the emerging use of spheroids in high throughput drug screening, image analysis tools have been developed that enable the automated evaluation of spheroids.[143,144] However, since size increase of the central spheroid is the relevant parameter of these screenings, analysis usually does not include sprouting efficiency or detachment of cells. The novel evaluation algorithm Ti-Quant-BF-2D allows the analysis of all these parameters on live-cell imaging data with a high temporal resolution (90 min or less).The list of parameters, which are thus evaluable, is the following: total spheroid area, area of the main spheroid, area of sprouts, number of detached cells, estimated radius, radius of gyration, and cell density distribution.

Other groups have also put efforts into developing evaluation methods for spheroid-invasion assays. For example, Evensen et al. presented another approach to quantify spheroid invasion suitable for standardized drug-screening settings.[145] However, this assay relies on staining of the cell nuclei for automated evaluation, whereas the novel algorithm presented here works well with bright field images. This has several advantages with regard to toxicity[146] and acquisition time. Also, by detecting the nuclei of invading cells, one runs

the risk of severely underestimating the invasion distance and behavior, since the cells frequently show elongated phenotypes (see Figure 27). The evaluation presented here takes this into account as represented by the radius of gyration parameter. However, one advantage of previous algorithms is the ability to analyze single spheroids without the influence of other nearby spheroids in the same gel.[145] While this influence can be mitigated by choosing isolated spheroids in the gel, paracrine effects cannot be completely excluded in the approach presented here. Ultimately, the experimental approach and evaluation algorithm presented here provide a very useful tool for systems-biology research-endeavors, and can improve on other approaches for commercial high-throughput screening-applications.[145]

FIR knockdown in Calu-1 cells again served as proof of principle, analogous to the 2D migration analysis. Here, the results of 2D migration could be confirmed in the 3D setting: knockdown of FIR resulted in reduced sprouting and radius of gyration (which stands for the maximum distance of cells migrating), but also reduced total area. Moreover, the number of detached cells was decreased.

Manual evaluation of H1975 spheroids subjected to IGF-1 and/or EGF stimulation did not show any significant effect on overall spheroid growth and sprouting. Applying the novel algorithm to the evaluation of H1975 spheroids after IGF-1 and EGF treatment might uncover effects of EGF and IGF-1 treatment that were not visible using traditional evaluation methods.

Several mathematical models were proposed that link the growth kinetics on the multi-cellular level (radius/volume in time) to cellular mechanisms (cell growth, contact inhibition, nutrient limitation, etc.), either as continuum models for component densities evolving over time and space (using PDEs)[147,148] or *agent based models* (ABMs) that model cells and their behavior (growth, division, movement, death) individually.[149] Models based on quantitative bright field imaging approaches like the one presented here have been published by Frieboes et al.[150] in a Non-Hodgkin lymphoma setting and Macklin et al. to predict ductal carcinoma growth in individual patients and in breast cancer [151,152]. Similar approaches for NSCLC will help to elucidate cellular mechanisms for the early spread and dissemination of cancer cells.

5.3 Effects of IGF-1 and EGF stimulation on NSCLC cells

5.3.1 Pathway activation and ODE model

To build a first ODE model for the EGFR and IGF-1R signaling pathways, comprehensive time course data of the activation kinetics of both receptors and the key downstream proteins ERK and AKT were generated for H838 NSCLC cells. In a second step, the same dataset was generated for H1975 cells and first measures were taken to adapt the model to be able to explain the pathway activation behavior in both cell lines. In order to ensure the validity of the stimulation setup, depletion and secretion of both factors in both cell lines was investigated, with both cell lines showing no secretion over 24 hours and quick depletion of both EGF and IGF-1.

IGF-1 and EGF pathway activation in H838

A. EGFR stimulation

Firstly, no receptor cross-activation with the opposite cytokine respectively was detected. EGFR activation/phosphorylation could be detected under EGF stimulation with a strong and rapid activation and transient kinetics. Very similar activation kinetics have been shown in HeLa cells after EGF administration.[153]. Interestingly, after double stimulation with EGF and IGF-1, EGFR activation is reduced while the general transient activation kinetic is preserved. This negative regulation between IGF and EGF signalling has so far not been observed in any published study. Reasons for this down regulation of maximal signal intensity could be direct interactions between the activated receptor (as implemented in the ODE model through a single inhibitory reaction of phosphorylated IGF-1R towards EGFR), but also indirect mechanisms such as competition for high-energy donor-molecules. Furthermore, phosphatase activity has been reported to be important for the rapid negative feedback regulation of signaling pathways.[154] As such, even though both receptors show equally rapid phosphorylation kinetics with strong activation in the first 5 to 10 minutes, activation of phosphatases by IGF-1R might explain the reduced EGFR activation.

Equally intriguing is the fact that depletion of the receptor starts directly after stimulation and shows the same dynamic in the double-stimulation condition as with stimulation with EGF alone (even though EGFR activation is significantly higher with EGF alone). Thus the receptor depletion seems to be at least partially independent from the observed receptor phosphorylation/activation. Technical explanations for this could lie in the choice of antibodies, as the anti-phospho EGFR antibody used in this study detects the specific

phosphorylation site at Tyr1068. As there are over fifty other activating phoshpo-sites at the EGFR,[155] it is possible that phosphorylation on other sites might be even earlier events, thus leading to a "masked" activation of the EGFR that already leads to degradation after internalization. For example, Jiang et al. reported that next to Tyr1068, Tyr1086 was responsible for Grb2 dependent and clathrin-mediated internalization of activated EGFR in the first minutes after EGF stimulation[156] and Tanos et al. showed the involvement of Tyr1173 in Abl regulated EGFR internalization.[157] A systematic analysis of phospho-site-specific EGFR internalization efficiency has not been performed yet.

On the other hand, clathrin-mediated endocytosis of ligand-bound receptors is a very fast process with a rate constant K_e of up to 0.6 min-1.[158] Thus the noticeable drop in total EGFR amounts might be explained by biology, with the subsequent plateau being explained by the upregulation of rapid recycling after 10 minutes resulting in a new steady state. In the model, the assumed K_e is decidedly lower with 0.01 min-1. This discrepancy to the literature data can be attributed to the simplifications in the model. For example, the model only considers internalization of activated receptors. The actual endocytosis rates and dynamic behavior of EGFR after stimulation and ligand binding is under investigation by cooperation partners in the LungSysII consortium in the Single-Molecule Spectroscopy Research Group of Prof. Dr. D. Herten (Cellnetworks Cluster and Inst. for Physical Chemistry, Heidelberg University) using single-molecule imaging-techniques. Incorporating this information into the model will contribute to the elucidation of this interesting behavior.

B. IGF-1R stimulation

Activation/phosphorylation dynamics of IGF-1R after IGF-1 stimulation were comparable to the EGFR activation in terms of speed of response, with maximal activation levels being reached at 10 minutes. Whereas EGFR activation was transient, IGF-1R phosphorylation displayed a sustained activation on the maximal level until 2 hours before slowly declining. Guakova et al. showed a similarly sustained IGF-1R activation in breast cancer cells,[159] whereas Hallak et al. demonstrated a more transient activation in rat hepatocytes[160]. In contrast to the reducing effect of double stimulation on EGFR activation, both the dynamic as well as total strength of response of IGF-1R phosphorylation stayed the same in the double stimulation compared to treatment with IGF-1 alone. Equally, in contrast to EGFR internalization after EGF administration, total IGF-1R levels also stayed constant over the observed time.

C. Downstream effectors

Downstream of the receptors, ERK and AKT activation behaved different with regard to stimulation with EGF, IGF-1, or both cytokines. For the treatment with single growth factors, the dynamics of phosphorylated AKT followed those of the activated receptors, albeit with a somewhat reduced strength of response and a delay of 5 to 10 minutes. As such, AKT activation after EGF stimulation shows a more transient progression with the maximum after ~15minutes (similar to results published in pancreatic cancer[161]), whereas the activation after IGF-1 stimulation shows a more sustained phenotype with the maximum being reached at 30 minutes. This sustained activation has been shown in NSCLC[162] and other cell systems such as skeletal muscle,[163] HEK293 and neuroblastoma.[164]

Double stimulation shows an additive effect on AKT compared to the single treatments, with a higher maximum activation being reached after 15 minutes and a more sustained dynamic compared to EGF stimulation. Neither complete addition of the signals nor any synergistic effects could be detected, as the signal of the double stimulation does not equal the sum of both single stimulations at the maximum signal intensity at 15 minutes. At later time points (e.g. at 60 minutes and later) this is achieved and the signal strength in the double stimulation does equal the sum of both single stimulations. A first explanation for this follows from the receptor activation dynamics: the down regulation of EGFR activation in the double stimulation compared to EGF alone would explain the reduced signal. Alternatively, a saturation of available AKT molecules could limit the signal. Both hypotheses can be tested with the ODE model. Here, the first hypothesis was supported by the model, whereas pAKT levels were far from being saturated. This model prediction would be experimentally testable by applying semi-quantitative mass-spectrometry to investigate the ratio of AKT to pAKT during the time course as described by Hahn et al.[165]

Concerning ERK activation, the situation is less complex. While the phosphorylation of ERK follows the EGFR activation after EGF stimulation closely, IGF-1 stimulation results in a similar but decidedly weaker activation. Olsen et al. showed very similar ERK activation after EGF stimulation in HeLa cells,[153] whereas Girnita et al. reported a similar transient activation after IGF-1 stimulation in melanoma cells.[166] Double stimulation shows no change compared to EGF stimulation alone, thus either the ERK activation was already saturated and surplus EGFR activation in the single treatment had no effect, or the low ERK activation after IGF-1 stimulation is able to compensate for the reduced EGFR signaling. Again, after taking the model parameters into account, saturation of ERK activation can be disregarded in favor of the compensation via IGF-1R activation.

Summing up, in H838 cells, EGF stimulation activated both AKT and ERK with a similar dynamic of the receptor activation. IGF-1 signaling is transmitted more prominently via AKT, with only low ERK activation. Double stimulation shows some additive effects on AKT signalingand to a lesser extent on ERK signaling. Concerning the direct crosstalk between the receptors, only an inhibitory effect of activated IGF-1R on EGFR activation could be detected beyond the activation of the same downstream receptors.

Model generation

The EGFR pathway is one of the best studied growth-factor pathways. Modeling it has been called a paradigm for systems biology.[167] Accordingly, a number of EGF pathway models have been published over the years, with some taking into account the activation dynamics[168] and crosstalk between EGFR and other TRKs like IGF-1R.[169] However, the approach reported here has major advantages over others. For one, most models were either based on standard cell-culture cell-lines like HeLa,[168] which is probably not informative for NSCLC cell lines, or do not incorporate measured pathway activation data at all. These aspects might be the reason for differences in the assumptions and predictions between these published models and the one presented here. For example, Bianconi et al. argued from clinical data and histological investigation, and incorporated a pathway scheme from literature.[169] While the reported transient dynamic behavior of ERK activation resulting from the model simulations fits with the experimental observations made in the present study in both cell lines, Bianconi et al. reported that in their simulations both EGFR and IGF-1R dynamics induced the same ERK activation whereas in the study presented here, EGFR leads to a significantly increased ERK activation compared to IGF-1R.

Thus, to generate meaningful and applicable models for a given cell type and disease, a data driven approach to ODE models as used in the present study seems warranted, if not downright necessary.

The minimal model approach that was employed here follows the general principle of the Akaike information criterion (AIC), which is used to describe the quality of a model. In short, the principle stands for the fact that the more exact a given model represents the data and the fewer parameters are needed, the better the model quality. High numbers of parameters incur the risk of overfitting and unidentifiability if too many model components are not supported by measured data.

Additionally, publications like the ones from Csete et al. showed that a complex system could still give rise to simple behavior as a characteristic of robust systems.[170] Thus, when focusing on the behavior of central pathway nodes, most of the complexity of the upstream signaling pathways can be ignored. This is supported when comparing the ERK data from my study to previously published results from Bianconi et al. that used a more complex pathway model, [169] as our (simple) model yields a comparable dynamic behavior.

EGF and IGF-1 dose effect in H838 and model refinement

Dose-response experiments confirmed some but not all of the findings from the kinetics. Generally, dose-dependent activation of both receptors and downstream effectors ERK and AKT could be shown with some differences to the kinetic dataset. These inconsistencies can be explained by the lower number of replicates and the measurements at single time points, as small shifts in the dynamic behavior especially impact factors with steep initial activation like the ones investigated here. Nevertheless, by incorporating these dose response data for IGF-1, EGF, and double stimulation into the model, the identifiability was significantly increased for the phosphorylation and dephosphorylartion parameters for AKT and ERK.

EGF and IGF-1 pathway activation in H1975

The pathway activation dataset for H1975 was generated in the same manner as the H838 dataset. Nevertheless, the data is considerably noisier and displays higher variations in the replicates. One possible explanation for these effects might be the activating mutations in the EGFR of H1975 cells. Hereby, the activating mutation raises the background activation, especially of the downstream effectors, and thus increases the noise in the measurements.

Important differences between the H838 and the H1975 in the dataset are:

- The constitutively active EGFR receptor partly leads to insensitivity against EGF stimulation in the pEGFR measurements.

- IGF-1R is strongly activated (as also shown by Peled et al.[171]) and this activation shows a transient behavior with a narrow peak shape comparable to findings by Hallak et al. generated in rat hepatocytes.[160] In the double stimulation condition, the mean phosphorylation peaks higher than with IGF-1 alone, but the high variation renders this insecure.

- The downstream effects do not completely mirror the receptor activation. For one, ERK phosphorylation reacts to EGF stimulation even though no change in EGFR Tyr1068 phospho site could be detected. In contrast, IGF-1 treatment results in only a very low activation of ERK, even though the receptor showed a clear activation.

- For AKT, only the double stimulation resulted in measurable phosphorylation, with the maximum being reached at 15 minutes followed by a sustained response, similar to the findings of Ma et al.[162] and Bijur et al.[164] for IGF-1 stimulation.

Interestingly, the dose-response experiments in H1975 showed a better accordance to the kinetics dataset than was the case for H838:

- EGFR activation showed the same insensitivity for a wide range of concentrations.

- IGF-1R activation showed saturation of signal at 10 ng/ml, with no difference between stimulation with just IGF-1 and the double treatment.

- ERK phosphorylation showed a similar behavior as with the time courses, saturating at 10 ng/ml of EGF and double stimulation.

- AKT phosphorylation showed dependency on IGF and EGF stimulation, with additive effects in the double stimulation.

Integration of H1975 data in ODE model

The noisiness of the data made the incorporation into the ODE model difficult. As a first step, the IGF-1R activation could be integrated into the model so that both the activation dynamics for H838 and H1975 cells can be sufficiently explained by the same model. Hereby, parameter fitting lead to the assumption that H838 cells harbor highly increased amounts, i.e. 17 times more IGF-1R than H1975. Experimental validation showed that H838 contain 21 times more IGF-1R than H1975. In a comparative analysis of different NSLCLC cell lines by Gong et al., H1975 cells equally showed low IGF-1R protein levels[172]. This excellent agreement between model assumption and experimental validation indicates that the simple ODE model in it's current state is already able to explain central pathway processes. Fitting both datasets also lead to a further refinement of the model by adding an autoinhibitory loop to the IGF-1R signaling module, thereby further increasing model fits for the IGF-1R activation dynamics for both cell lines. Biologically this autoinhibitory loop could be interpreted as the effect of up regulated IGF binding proteins (IGFBPs)[173] or an increased activity of phosphatases abolishing IGF-1R phosphorylation.[174]

5.3.2 Biological effects after stimulation

In both viability and migration assays, IGF-1 and EGF single stimulation as well as double stimulation did not show significant effects. Whereas H838 cells lost all migratory capacity under starvation, H1975 cells still showed migration capability, albeit with a highly reduced strength, making them a good model to analyse IGF-1R- and EGFR-induced NSCLC mobility.

The lack of obvious effects of both the single treatments as well as the double stimulation points to the involvement of more co-factors necessary for the induction of complete migratory phenotype: the FCS supplied in full propagation medium contains a wide array of growth factors and low-molecular substances, which may play a part in the complex signaling network that governs migration[175].

5.4 Effects of IGF-1R and EGFR inhibition on NSCLC cells

From the lack of phenotypes after stimulation with IGF and/or EGF, the conclusion arises that the cells might need to be primed for migration by a combination of growth factors, which is then taken advantage of by increased EGF and/or IGF-1 signaling. In order to investigate this hypothesis, the functional effects of EGFR and IGF-1R inhibition on NSCLC cells under full propagation medium with FCS were studied. Inhibition of signaling through small molecule TKIs is inherently less specific than stimulation with specific ligands, due to possible off-target effects.[176] To control for these effects, three different EGFR inhibitors were used: Erlotinib, Afatinib and CAS-879127-07-8. While both Erlotinib andCAS-879127-07-8 inhibit the EGFR by reversibly binding to the ATP site of the EGFR kinase domain,[177] Afatinib inhibition functions by irreversibly binding to the ATP site via sulfate bridges.[48] In the experimental setup used in this study, all three inhibitors effectively impair cell proliferation, increase apoptosis and reduce 2D migration of both H838 and H1975, illustrating that EGFR signaling is a relevant regulator of these processes.

First corresponding results for IGF-1R inhibition have been obtained through the use of PPP. PPP inhibits IGF-1R autophosphorylation through an ATP independent mechanism.[166] It has been shown to be effective and selective for IGF-R inhibition in several in vitro and in vivo model systems[178] and is currently tested in lung cancer patients in trial NCT01561456 .

Comparison of H838 and H1975 proliferation after TRK inhibition

Interestingly, H1975 cells show a more differentiated response to the different doses of all used inhibitors in the proliferation assays. Whereas H838 showed a distinct threshold behavior, where the response increased drastically between two of the tested concentrations (e.g. hardly any impact on proliferation for 1 μM of Afatinib and complete abolishment of proliferation at 10 μM), H1975 showed a gradual increase of the dose response for all tested inhibitors. For the EGFR inhibition, this might be explained by the increased affinity of EGFR to ATP in H1975 cells due to the T790M mutation, which could reduce the sensitivity for all inhibitory treatments. However, as the response to IGF-1R inhibition shows the same effect, it stands to reason that the makeup of the downstream signaling network is responsible for this more differentiated response. Indeed, quantitative mass-spectrometry analysis revealed, that H838 cells harbor about 220 nM of AKT and 950 nM of ERK (ERK1/2 combined), whereas H1975cells harbor about 120 nM of AKT and 890 nM of ERK, respectively (private correspondence with Prof. U. Klingmüller). Thus different

stoichiometry of cellular downstream effectors might explain the observed differences between the inhibitors in the cell systems used.

Rescue of migration after EGFR inhibition

In order to further support the hypothesis of EGF and IGF-1 pathway interconnection, the rescue of the observed phenotypes after inhibition of EGFR and IGF-1R by stimulation with the opposite growth factor was investigated. Neither of the experiments resulted in a measurable rescue effect on proliferation and apoptosis for H838 nor H1975 cells. Interestingly, for 2D migration, stimulation with IGF-1 after EGFR inhibition with 50 nM CAS-879127-07-8 resulted in a significant and temporally limited, but nevertheless reproducible increase in migration compared to the EGFR inhibition alone.

Similar findings have been published for HGF, which rescued EGFR inhibition in colorectal cancer[179] and NSCLC[180] as well as for EGF, HGF, and FGF in a multi-kinase inhibitor setting in pediatric low grade astrocytoma and ependymoma[181], indicating that the rescue of specific pathway inhibition by parallel acting cytokines is a general mechanism in cancer cells. As also demonstrated in these and other studies, the rescue effect shown here is only partial, which is in accordance with findings from Jameson et al.[81] This makes sense in the context of the complex signaling system, as also implied in the results of EGF and IGF stimulation presented here: The ultimate phenotype depends on the interplay of more than two growth factors. The increase in AKT activation under double stimulation shown here for H1975 indicates that the partial rescue via IGF-1 stimulation might be facilitated by AKT in this experimental setting.

5.5 Transcriptional effects of IGF-1 and EGF stimulation

Having shown connections between both EGF and IGF-1 signaling pathways on protein-activation level as well as for 2D migration, first steps were taken to connect those two levels of cellular response via expression of target genes. To this end, expression analysis of H1975 cells after IGF-1 and EGF stimulation was performed. Using novel approaches developed by cooperation partners in the LungSysII consortium (M. Albrecht from the group of Dr. F. Matthäus), GO annotation was performed and gene responses were ranked according to expression change over the total time course. Using qRT-PCR investigations, genes with GO terms connected to migration and invasion were chosen to validate the microarray results. EGF responding genes such as CTGF, AREG, and IL8 could be validated at the transcript level.

GO terms for CTGF indicate a connection to migration and cell matrix adhesion. Interestingly, CTGF overexpression has been found to suppress AKT activation after IGF-1 stimulation, and ERK activation after EGF stimulation.[182] As the EGFR is constitutively active in H1975 cells, this mechanism might be in part responsible for the low activation of AKT in these cells. Also, together with the activation seen after EGF stimulation, this points to CTGF facilitating the transient shape of ERK activation. AREG on the other hand yielded GO terms connected to DNA replication and cell proliferation. Nevertheless, in ovarian cancer, AREG has been shown to induce cell invasion.[183] Additionally, it has been linked to IGF-1 signaling in NSCLC,[184] thus presenting a promising target for therapy.[185] Finally, IL8 GO annotation points toward roles in proliferation but also cell adhesion and chemotaxis. Accordingly, in NSCLC, IL8 has been shown to stimulate proliferation,[186] whereas invasion enhancing effects could be shown in breast cancer cells.[187]

In contrast, genes that were identified as responding to IGF-1 stimulation on the microarray dataset could not be validated. Reasons for this could lie in the general quality of the IGF response. PCA analysis of the preprocessed datasets revealed that the trajectory of the IGF-1 stimulation transcriptome data resembles that of the EGF stimulation, but with a parallel shift already after 0.5h.

5.6 Implications for early spread and TKI resistance in NSCLC

Early and frequent metastasis is one of the reasons for the high mortality among lung cancer patients, as introduced in 1.1.1.Therefore, controlling the early spread and invasion of lung cancer cells promises to increase patient survival. Accordingly, migration and invasion have been important output parameters for *in vitro* experiments regarding cancer and NSCLC therapy.[188-190] The results presented here further underpin the importance of EGFR and IGF1-R signaling in NSCLC, by showing both reduction of proliferation and, more importantly, migration after inhibition of both IGF-1R and EGFR. Additionally, the microarray analysis of especially EGF stimulated H1975 substantiates the impact of EGF on NSCLC cell migration.

The second important contributor to the low 5-year survival of NSCLC is the emergence of acquired resistances to TKI treatment generally limiting therapy.[10] The most common mechanisms here are secondary mutations. For instance, up to 60% of patients with TKI resistant EGFR-mutant NSCLC harbor the T790M mutation in the threonine gatekeeper residue in addition to the activating L858R mutations or exon 19 deletions.[60,61,191] As introduced in 1.2.3, a second generation of EGFR inhibitors have been developed that showed potency against T790M mutated cells in preclinical models,[48,192] but also showed

only modest effects in clinical studies with patients that had developed resistance against Erlotinib or Gefitinib.[193,194] One reason for this, as hypothesized by Cortot et al., could be the relatively low achievable drug concentration in patients *vs* the in vitro studies.[90] This is corroborated by further in vitro studies that showed emergence of T790M mutant cells under treatment with similarly low concentration of Afatinib.[195,196] Accordingly, Cortot at al. identified combinatorial treatment strategies of efficient T790M inhibition together with IGF-1R inhibition that prevented the emergence of drug resistant clones in vitro.[90]

The results of the study presented here also support an impact of IGF-1R signaling on the resistance of NSCLC cells against EGFR inhibition. Firstly, IGF-1R and EGFR activation was transmitted along the same downstream effectors ERK and AKT, albeit with different activation dynamics. Secondly, while no effect on proliferation could be shown here, IGF-1 signaling could rescue the reduction of migration after EGFR inhibition.

Concerning the molecular mechanisms, an additional factor worth considering in the contributions of the IGF signaling system to acquired resistance of NSCLC is the role of IGF-binding proteins (IGFBPs), that control IGF-1R signaling through the binding of ligands. For example, IGFBP-3 secretion was reduced and lead to increased activity of the IGF1R/PI3K/AKT pathways in NSCLC lines with acquired resistance to Gefitinib or Erlotinib[88] as well as cisplatin resistant cells[197]. These studies have been conducted in cells, which were not checked for EGFR status. It will be interesting to investigate the available NGS sequences of see if the rescue effect observed in this study in the T790M mutated H1975 cell line is at least in part induced by similar down regulation of IGFBPs.

5.7 Outlook

In summary, in the work presented here, I could show that, while EGFR and IGF-1R signaling are important for NSCLC migration in both cells with the wild type and the mutated EGFR, they are contributors in a more complex growth-factor signaling-network. It will be of importance to further investigate the dynamic interactions between large subsets of this network to engage kinase switching and other forms of acquired resistance and elucidate possible points of intervention for novel therapies. The novel phenotypical evaluation algorithms delivered useful quantitative data for modeling approaches, and the resulting data were used as a basis for agent-based modeling of NSCLC migration. In the framework of the LungSys consortium, the data and models generated in this work will be used as the basis for integrated multiscale modeling of the complex conditions governing NSCLC migration and the relevant cell signaling. Going forward, the ODE model generated here will need to be expanded and the phenotypical data will need to be integrated in order to generate biologically useful testable hypotheses. Thus, important insight will be gained into the dynamic signaling interplay and resulting therapeutic options for NSCLC, the deadliest cancer to date.

6 References

1   Siegel, R., Ma, J., Zou, Z. & Jemal, A. Cancer statistics, 2014. *CA Cancer J Clin* **64**, 9-29, doi:10.3322/caac.21208 (2014).

2   IARC. *GLOBOCAN*, <http://http://globocan.iarc.fr/> (2015).

3   Travis D, B. E., Mueller-Hermelink HK, Harris CC. *World Health Organization classification of tumors. Pathology and genetics. Tumors of the lung, pleura, thymus and heart.*, (IARC Press, 2004).

4   Morgensztern, D., Ng, S. H., Gao, F. & Govindan, R. Trends in stage distribution for patients with non-small cell lung cancer: a National Cancer Database survey. *Journal of thoracic oncology : official publication of the International Association for the Study of Lung Cancer* **5**, 29-33, doi:10.1097/JTO.0b013e3181c5920c (2010).

5   Lortet-Tieulent, J. *et al.* International trends in lung cancer incidence by histological subtype: adenocarcinoma stabilizing in men but still increasing in women. *Lung Cancer* **84**, 13-22, doi:10.1016/j.lungcan.2014.01.009 (2014).

6   Travis, W. D. *et al.* International association for the study of lung cancer/american thoracic society/european respiratory society international multidisciplinary classification of lung adenocarcinoma. *Journal of thoracic oncology : official publication of the International Association for the Study of Lung Cancer* **6**, 244-285, doi:10.1097/JTO.0b013e318206a221 (2011).

7   Warth, A. *et al.* EGFR, KRAS, BRAF and ALK gene alterations in lung adenocarcinomas: patient outcome, interplay with morphology and immunophenotype. *The European respiratory journal* **43**, 872-883, doi:10.1183/09031936.00018013 (2014).

8   Sandler, A. *et al.* Paclitaxel-carboplatin alone or with bevacizumab for non-small-cell lung cancer. *The New England journal of medicine* **355**, 2542-2550, doi:10.1056/NEJMoa061884 (2006).

9   Rosell, R. *et al.* Erlotinib versus standard chemotherapy as first-line treatment for European patients with advanced EGFR mutation-positive non-small-cell lung cancer (EURTAC): a multicentre, open-label, randomised phase 3 trial. *The Lancet. Oncology* **13**, 239-246, doi:10.1016/S1470-2045(11)70393-X (2012).

10   Engelman, J. A. & Janne, P. A. Mechanisms of acquired resistance to epidermal growth factor receptor tyrosine kinase inhibitors in non-small cell lung cancer. *Clinical cancer research : an official journal of the American Association for Cancer Research* **14**, 2895-2899, doi:10.1158/1078-0432.CCR-07-2248 (2008).

11   Cortot, A. B. & Janne, P. A. Molecular mechanisms of resistance in epidermal growth factor receptor-mutant lung adenocarcinomas. *European respiratory review : an official journal of the European Respiratory Society* **23**, 356-366, doi:10.1183/09059180.00004614 (2014).

12   Sun, C. & Bernards, R. Feedback and redundancy in receptor tyrosine kinase signaling: relevance to cancer therapies. *Trends in biochemical sciences* **39**, 465-474, doi:10.1016/j.tibs.2014.08.010 (2014).

13   Hanahan, D. & Weinberg, R. A. Hallmarks of cancer: the next generation. *Cell* **144**, 646-674, doi:10.1016/j.cell.2011.02.013 (2011).

14   Salani, B. *et al.* IGF-IR internalizes with Caveolin-1 and PTRF/Cavin in HaCat cells. *PloS one* **5**, e14157, doi:10.1371/journal.pone.0014157 (2010).

15   Downward, J. Targeting RAS signalling pathways in cancer therapy. *Nature reviews. Cancer* **3**, 11-22, doi:10.1038/nrc969 (2003).

16   Marais, R., Light, Y., Paterson, H. F. & Marshall, C. J. Ras recruits Raf-1 to the plasma membrane for activation by tyrosine phosphorylation. *The EMBO journal* **14**, 3136-3145 (1995).

17   McCubrey, J. A. *et al.* Targeting survival cascades induced by activation of Ras/Raf/MEK/ERK, PI3K/PTEN/Akt/mTOR and Jak/STAT pathways for effective leukemia therapy. *Leukemia* **22**, 708-722, doi:10.1038/leu.2008.27 (2008).

18   McCubrey, J. A. *et al.* Emerging Raf inhibitors. *Expert Opin Emerg Drugs* **14**, 633-648, doi:10.1517/14728210903232633 (2009).

19   Lefloch, R., Pouyssegur, J. & Lenormand, P. Total ERK1/2 activity regulates cell proliferation. *Cell cycle* **8**, 705-711 (2009).

20   Steelman, L. S. *et al.* Roles of the Raf/MEK/ERK and PI3K/PTEN/Akt/mTOR pathways in controlling growth and sensitivity to therapy-implications for cancer and aging. *Aging* **3**, 192-222 (2011).

21   Xing, J., Ginty, D. D. & Greenberg, M. E. Coupling of the RAS-MAPK pathway to gene activation by RSK2, a growth factor-regulated CREB kinase. *Science* **273**, 959-963 (1996).

22   Meloche, S. & Pouyssegur, J. The ERK1/2 mitogen-activated protein kinase pathway as a master regulator of the G1- to S-phase transition. *Oncogene* **26**, 3227-3239, doi:10.1038/sj.onc.1210414 (2007).

23   Provenzano, P. P., Inman, D. R., Eliceiri, K. W. & Keely, P. J. Matrix density-induced mechanoregulation of breast cell phenotype, signaling and gene expression through a FAK-ERK linkage. *Oncogene* **28**, 4326-4343, doi:10.1038/onc.2009.299 (2009).

24   Chen, H. *et al.* Extracellular signal-regulated kinase signaling pathway regulates breast cancer cell migration by maintaining slug expression. *Cancer research* **69**, 9228-9235, doi:10.1158/0008-5472.CAN-09-1950 (2009).

25   Huang, C., Jacobson, K. & Schaller, M. D. MAP kinases and cell migration. *Journal of cell science* **117**, 4619-4628, doi:10.1242/jcs.01481 (2004).

26   Martelli, A. M., Evangelisti, C., Chiarini, F. & McCubrey, J. A. The phosphatidylinositol 3-kinase/Akt/mTOR signaling network as a therapeutic target in acute myelogenous leukemia patients. *Oncotarget* **1**, 89-103 (2010).

27   Lee, J. T., Steelman, L. S., Chappell, W. H. & McCubrey, J. A. Akt inactivates ERK causing decreased response to chemotherapeutic drugs in advanced CaP cells. *Cell cycle* **7**, 631-636 (2008).

28   Altomare, D. A. & Testa, J. R. Perturbations of the AKT signaling pathway in human cancer. *Oncogene* **24**, 7455-7464, doi:10.1038/sj.onc.1209085 (2005).

29   Manning, B. D. & Cantley, L. C. AKT/PKB signaling: navigating downstream. *Cell* **129**, 1261-1274, doi:10.1016/j.cell.2007.06.009 (2007).

30   Kane, L. P., Shapiro, V. S., Stokoe, D. & Weiss, A. Induction of NF-kappaB by the Akt/PKB kinase. *Current biology : CB* **9**, 601-604 (1999).

31   Romashkova, J. A. & Makarov, S. S. NF-kappaB is a target of AKT in anti-apoptotic PDGF signalling. *Nature* **401**, 86-90, doi:10.1038/43474 (1999).

32   Cross, D., Alessi, R., Cohen, P., Andjelkovich, M. & Hemmings, B. A. Nature_Inhibition of glycogen synthase kinase-3 by insulin mediated by protein kinase B. *Nature* **378** (1995).

33   Xue, G. & Hemmings, B. A. PKB/Akt-dependent regulation of cell motility. *J Natl Cancer Inst* **105**, 393-404, doi:10.1093/jnci/djs648 (2013).

34   Enomoto, A. *et al.* Akt/PKB regulates actin organization and cell motility via Girdin/APE. *Developmental cell* **9**, 389-402, doi:10.1016/j.devcel.2005.08.001 (2005).

35   Kim, D. *et al.* Akt/PKB promotes cancer cell invasion via increased motility and metalloproteinase production. *FASEB journal : official publication of the Federation of American Societies for Experimental Biology* **15**, 1953-1962, doi:10.1096/fj.01-0198com (2001).

36   Laplante, M. & Sabatini, D. M. Regulation of mTORC1 and its impact on gene expression at a glance. *Journal of cell science* **126**, 1713-1719, doi:10.1242/jcs.125773 (2013).

37   Du, K. & Montminy, M. CREB is a regulatory target for the protein kinase Akt/PKB. *The Journal of biological chemistry* **273**, 32377-32379 (1998).

38   Brennan, P. *et al.* Phosphatidylinositol 3-kinase couples the interleukin-2 receptor to the cell cycle regulator E2F. *Immunity* **7**, 679-689 (1997).

39   Ding, L. *et al.* Somatic mutations affect key pathways in lung adenocarcinoma. *Nature* **455**, 1069-1075, doi:10.1038/nature07423 (2008).

40   Kim, Y., Apetri, M., Luo, B., Settleman, J. E. & Anderson, K. S. Differential Effects of Tyrosine Kinase Inhibitors on Normal and Oncogenic EGFR Signaling and Downstream Effectors. *Molecular cancer research : MCR* **13**, 765-774, doi:10.1158/1541-7786.MCR-14-0326 (2015).

41   Schlessinger, J. Ligand-induced, receptor-mediated dimerization and activation of EGF receptor. *Cell* **110**, 669-672 (2002).

42   Oda, K., Matsuoka, Y., Funahashi, A. & Kitano, H. A comprehensive pathway map of epidermal growth factor receptor signaling. *Molecular systems biology* **1**, 2005 0010, doi:10.1038/msb4100014 (2005).

43   Yarden, Y. The EGFR family and its ligands in human cancer. signalling mechanisms and therapeutic opportunities. *Eur J Cancer* **37 Suppl 4**, S3-8 (2001).

44   Hynes, N. E. & Lane, H. A. ERBB receptors and cancer: the complexity of targeted inhibitors. *Nature reviews. Cancer* **5**, 341-354, doi:10.1038/nrc1609 (2005).

45   Sharma, S. V., Bell, D. W., Settleman, J. & Haber, D. A. Epidermal growth factor receptor mutations in lung cancer. *Nature reviews. Cancer* **7**, 169-181, doi:10.1038/nrc2088 (2007).

46   Paik, J. H. *et al.* Screening of anaplastic lymphoma kinase rearrangement by immunohistochemistry in non-small cell lung cancer: correlation with fluorescence in situ hybridization. *Journal of thoracic oncology : official publication of the International Association for the Study of Lung Cancer* **6**, 466-472, doi:10.1097/JTO.0b013e31820b82e8 (2011).

47   Araujo, A. *et al.* Genetic polymorphisms of the epidermal growth factor and related receptor in non-small cell lung cancer--a review of the literature. *Oncologist* **12**, 201-210, doi:12/2/201 [pii] 10.1634/theoncologist.12-2-201 (2007).

48   Li, D. *et al.* BIBW2992, an irreversible EGFR/HER2 inhibitor highly effective in preclinical lung cancer models. *Oncogene* **27**, 4702-4711, doi:10.1038/onc.2008.109 (2008).

49   Cheng, L. *et al.* Molecular pathology of lung cancer: key to personalized medicine. *Modern pathology : an official journal of the United States and Canadian Academy of Pathology, Inc* **25**, 347-369, doi:10.1038/modpathol.2011.215 (2012).

50   Chung, K. P. *et al.* Clinical outcomes in non-small cell lung cancers harboring different exon 19 deletions in EGFR. *Clinical cancer research : an official journal of the American Association for Cancer Research* **18**, 3470-3477, doi:10.1158/1078-0432.CCR-11-2353 (2012).

51   Roengvoraphoj, M., Tsongalis, G. J., Dragnev, K. H. & Rigas, J. R. Epidermal growth factor receptor tyrosine kinase inhibitors as initial therapy for non-small cell lung cancer: focus on epidermal growth factor receptor mutation testing and mutation-positive patients. *Cancer treatment reviews* **39**, 839-850, doi:10.1016/j.ctrv.2013.05.001 (2013).

52   Lynch, T. J. *et al.* Activating mutations in the epidermal growth factor receptor underlying responsiveness of non-small-cell lung cancer to gefitinib. *The New England journal of medicine* **350**, 2129-2139, doi:10.1056/NEJMoa040938 (2004).

53   Paez, J. G. *et al.* EGFR mutations in lung cancer: correlation with clinical response to gefitinib therapy. *Science* **304**, 1497-1500, doi:10.1126/science.1099314 (2004).

54   Pao, W. *et al.* EGF receptor gene mutations are common in lung cancers from "never smokers" and are associated with sensitivity of tumors to gefitinib and erlotinib. *Proc Natl Acad Sci U S A* **101**, 13306-13311, doi:10.1073/pnas.0405220101 (2004).

55   Shigematsu, H. *et al.* Clinical and biological features associated with epidermal growth factor receptor gene mutations in lung cancers. *J Natl Cancer Inst* **97**, 339-346, doi:10.1093/jnci/dji055 (2005).

56   John, T., Liu, G. & Tsao, M. S. Overview of molecular testing in non-small-cell lung cancer: mutational analysis, gene copy number, protein expression and other biomarkers of EGFR for the prediction of response to tyrosine kinase inhibitors. *Oncogene* **28 Suppl 1**, S14-23, doi:10.1038/onc.2009.197 (2009).

57   Ladanyi, M. & Pao, W. Lung adenocarcinoma: guiding EGFR-targeted therapy and beyond. *Modern pathology : an official journal of the United States and Canadian Academy of Pathology, Inc* **21 Suppl 2**, S16-22, doi:10.1038/modpathol.3801018 (2008).

58   Shepherd, F. A. *et al.* Erlotinib in previously treated non-small-cell lung cancer. *The New England journal of medicine* **353**, 123-132, doi:10.1056/NEJMoa050753 (2005).

59   Sordella, R., Bell, D. W., Haber, D. A. & Settleman, J. Gefitinib-sensitizing EGFR mutations in lung cancer activate anti-apoptotic pathways. *Science* **305**, 1163-1167, doi:10.1126/science.1101637 (2004).

60   Oxnard, G. R. *et al.* Acquired resistance to EGFR tyrosine kinase inhibitors in EGFR-mutant lung cancer: distinct natural history of patients with tumors harboring the T790M mutation. *Clinical cancer research : an official journal of the American Association for Cancer Research* **17**, 1616-1622, doi:10.1158/1078-0432.CCR-10-2692 (2011).

61   Kobayashi, S. *et al.* EGFR mutation and resistance of non-small-cell lung cancer to gefitinib. *The New England journal of medicine* **352**, 786-792, doi:10.1056/NEJMoa044238 (2005).

62   Pao, W. *et al.* Acquired resistance of lung adenocarcinomas to gefitinib or erlotinib is associated with a second mutation in the EGFR kinase domain. *PLoS medicine* **2**, e73, doi:10.1371/journal.pmed.0020073 (2005).

63   Sharma, S. V. *et al.* A common signaling cascade may underlie "addiction" to the Src, BCR-ABL, and EGF receptor oncogenes. *Cancer cell* **10**, 425-435, doi:10.1016/j.ccr.2006.09.014 (2006).

64   Giaccone, G. & Wang, Y. Strategies for overcoming resistance to EGFR family tyrosine kinase inhibitors. *Cancer treatment reviews* **37**, 456-464, doi:10.1016/j.ctrv.2011.01.003 (2011).

65   Jones, J. I. & Clemmons, D. R. Insulin-like growth factors and their binding proteins: biological actions. *Endocrine reviews* **16**, 3-34, doi:10.1210/edrv-16-1-3 (1995).

66   Hubbard, S. R. & Miller, W. T. Receptor tyrosine kinases: mechanisms of activation and signaling. *Current opinion in cell biology* **19**, 117-123, doi:10.1016/j.ceb.2007.02.010 (2007).

67   Pollak, M. Insulin and insulin-like growth factor signalling in neoplasia. *Nature reviews. Cancer* **8**, 915-928, doi:10.1038/nrc2536 (2008).

68   Hayashi, K. *et al.* Insulin receptor substrate-1/SHP-2 interaction, a phenotype-dependent switching machinery of insulin-like growth factor-I signaling in vascular smooth muscle cells. *The Journal of biological chemistry* **279**, 40807-40818, doi:10.1074/jbc.M405100200 (2004).

69   Baserga, R. The insulin-like growth factor I receptor: a key to tumor growth? *Cancer research* **55**, 249-252 (1995).

70   Renehan, A. G. *et al.* Insulin-like growth factor (IGF)-I, IGF binding protein-3, and cancer risk: systematic review and meta-regression analysis. *Lancet* **363**, 1346-1353, doi:10.1016/S0140-6736(04)16044-3 (2004).

71   Aleem, E., Nehrbass, D., Klimek, F., Mayer, D. & Bannasch, P. Upregulation of the insulin receptor and type I insulin-like growth factor receptor are early events in

hepatocarcinogenesis. *Toxicologic pathology* **39**, 524-543, doi:10.1177/0192623310396905 (2011).

72   Favoni, R. E. *et al.* Expression and function of the insulin-like growth factor I system in human non-small-cell lung cancer and normal lung cell lines. *Int J Cancer* **56**, 858-866 (1994).

73   Spitz, M. R. *et al.* Serum insulin-like growth factor (IGF) and IGF-binding protein levels and risk of lung cancer: a case-control study nested in the beta-Carotene and Retinol Efficacy Trial Cohort. *Cancer Epidemiol Biomarkers Prev* **11**, 1413-1418 (2002).

74   Cohen, B. D. *et al.* Combination therapy enhances the inhibition of tumor growth with the fully human anti-type 1 insulin-like growth factor receptor monoclonal antibody CP-751,871. *Clinical cancer research : an official journal of the American Association for Cancer Research* **11**, 2063-2073, doi:10.1158/1078-0432.CCR-04-1070 (2005).

75   Karp, D. D. *et al.* Phase II study of the anti-insulin-like growth factor type 1 receptor antibody CP-751,871 in combination with paclitaxel and carboplatin in previously untreated, locally advanced, or metastatic non-small-cell lung cancer. *Journal of clinical oncology : official journal of the American Society of Clinical Oncology* **27**, 2516-2522, doi:10.1200/JCO.2008.19.9331 (2009).

76   Karp, D. D. *et al.* Safety, pharmacokinetics, and pharmacodynamics of the insulin-like growth factor type 1 receptor inhibitor figitumumab (CP-751,871) in combination with paclitaxel and carboplatin. *Journal of thoracic oncology : official publication of the International Association for the Study of Lung Cancer* **4**, 1397-1403, doi:10.1097/JTO.0b013e3181ba2f1d (2009).

77   Langer, C. J. *et al.* Randomized, phase III trial of first-line figitumumab in combination with paclitaxel and carboplatin versus paclitaxel and carboplatin alone in patients with advanced non-small-cell lung cancer. *Journal of clinical oncology : official journal of the American Society of Clinical Oncology* **32**, 2059-2066, doi:10.1200/JCO.2013.54.4932 (2014).

78   Reinmuth, N. *et al.* Insulin-like growth factor 1 pathway mutations and protein expression in resected non-small cell lung cancer. *Human pathology* **45**, 1162-1168, doi:10.1016/j.humpath.2014.01.010 (2014).

79   Tieri, P. *et al.* Network, degeneracy and bow tie. Integrating paradigms and architectures to grasp the complexity of the immune system. *Theoretical biology & medical modelling* **7**, 32, doi:10.1186/1742-4682-7-32 (2010).

80   Morgillo, F., Woo, J. K., Kim, E. S., Hong, W. K. & Lee, H. Y. Heterodimerization of insulin-like growth factor receptor/epidermal growth factor receptor and induction of survivin expression counteract the antitumor action of erlotinib. *Cancer research* **66**, 10100-10111, doi:10.1158/0008-5472.CAN-06-1684 (2006).

81   Jameson, M. J. *et al.* Activation of the insulin-like growth factor-1 receptor induces resistance to epidermal growth factor receptor antagonism in head and neck squamous carcinoma cells. *Molecular cancer therapeutics* **10**, 2124-2134, doi:10.1158/1535-7163.MCT-11-0294 (2011).

82   Desbois-Mouthon, C. *et al.* Impact of IGF-1R/EGFR cross-talks on hepatoma cell sensitivity to gefitinib. *Int J Cancer* **119**, 2557-2566, doi:10.1002/ijc.22221 (2006).

83   Huether, A. *et al.* Signaling pathways involved in the inhibition of epidermal growth factor receptor by erlotinib in hepatocellular cancer. *World journal of gastroenterology : WJG* **12**, 5160-5167 (2006).

84   Desbois-Mouthon, C. *et al.* Insulin-like growth factor-1 receptor inhibition induces a resistance mechanism via the epidermal growth factor receptor/HER3/AKT signaling pathway: rational basis for cotargeting insulin-like growth factor-1 receptor and epidermal growth factor receptor in hepatocellular carcinoma. *Clinical cancer research : an official journal of the American Association for Cancer Research* **15**, 5445-5456, doi:10.1158/1078-0432.CCR-08-2980 (2009).

85   Nahta, R., Yu, D., Hung, M. C., Hortobagyi, G. N. & Esteva, F. J. Mechanisms of disease: understanding resistance to HER2-targeted therapy in human breast cancer. *Nature clinical practice. Oncology* **3**, 269-280, doi:10.1038/ncponc0509 (2006).

86   Milano, A., Dal Lago, L., Sotiriou, C., Piccart, M. & Cardoso, F. What clinicians need to know about antioestrogen resistance in breast cancer therapy. *Eur J Cancer* **42**, 2692-2705, doi:10.1016/j.ejca.2006.06.022 (2006).

87   Nahta, R., Yuan, L. X., Zhang, B., Kobayashi, R. & Esteva, F. J. Insulin-like growth factor-I receptor/human epidermal growth factor receptor 2 heterodimerization contributes to trastuzumab resistance of breast cancer cells. *Cancer research* **65**, 11118-11128, doi:10.1158/0008-5472.CAN-04-3841 (2005).

88   Guix, M. *et al.* Acquired resistance to EGFR tyrosine kinase inhibitors in cancer cells is mediated by loss of IGF-binding proteins. *The Journal of clinical investigation* **118**, 2609-2619, doi:10.1172/JCI34588 (2008).

89   Morgillo, F. *et al.* Implication of the insulin-like growth factor-IR pathway in the resistance of non-small cell lung cancer cells to treatment with gefitinib. *Clinical cancer research : an official journal of the American Association for Cancer Research* **13**, 2795-2803, doi:10.1158/1078-0432.CCR-06-2077 (2007).

90   Cortot, A. B. *et al.* Resistance to irreversible EGF receptor tyrosine kinase inhibitors through a multistep mechanism involving the IGF1R pathway. *Cancer research* **73**, 834-843, doi:10.1158/0008-5472.CAN-12-2066 (2013).

91   Ramalingam, S. S. *et al.* Randomized phase II study of erlotinib in combination with placebo or R1507, a monoclonal antibody to insulin-like growth factor-1 receptor, for advanced-stage non-small-cell lung cancer. *Journal of clinical oncology : official journal of the American Society of Clinical Oncology* **29**, 4574-4580, doi:10.1200/JCO.2011.36.6799 (2011).

92   Yu, H. A., Riely, G. J. & Lovly, C. M. Therapeutic strategies utilized in the setting of acquired resistance to EGFR tyrosine kinase inhibitors. *Clinical cancer research : an official journal of the American Association for Cancer Research* **20**, 5898-5907, doi:10.1158/1078-0432.CCR-13-2437 (2014).

93   Weiner, N. *Cybernetics or Control and Communication in the Animal and the Machine*. (MIT Press, Cambidge, MA, 1948).

94   Bertalanffy, L. v. *General System Theory* (Braziller, New York, 1968).

95   Umbarger, H. E. Threonine deamination in Escherichia coli. II. Evidence for two L-threonine deaminases. *J. Bacteriol*, 105-120 (1957).

96   Yates, R. A. Control by uracil of formation of enzymes required for orotate synthesis. *J. Biol. Chem.* , 677-692 (1957).

97   Beckwith, J. R. Regulation of the lac operon. Recent studies on the regulation of lactose metabolism in Escherichia coli support the operon model. *Science*, 597-604 (1967).

98   Westerhoff, H. V. & Palsson, B. O. The evolution of molecular biology into systems biology. *Nature biotechnology* **22**, 1249-1252, doi:10.1038/nbt1020 (2004).

99   Kitano, H. Systems biology: a brief overview. *Science* **295**, 1662-1664, doi:10.1126/science.1069492 (2002).

100   Marshall, C. J. Specificity of receptor tyrosine kinase signaling: transient versus sustained extracellular signal-regulated kinase activation. *Cell* **80**, 179-185 (1995).

101   Batchelor, E., Loewer, A., Mock, C. & Lahav, G. Stimulus-dependent dynamics of p53 in single cells. *Molecular systems biology* **7**, 488, doi:10.1038/msb.2011.20 (2011).

102   Kholodenko, B. N., Hancock, J. F. & Kolch, W. Signalling ballet in space and time. *Nature reviews. Molecular cell biology* **11**, 414-426, doi:10.1038/nrm2901 (2010).

103   Niethammer, P., Bastiaens, P. & Karsenti, E. Stathmin-tubulin interaction gradients in motile and mitotic cells. *Science* **303**, 1862-1866, doi:10.1126/science.1094108 (2004).

104   Spencer, S. L., Gaudet, S., Albeck, J. G., Burke, J. M. & Sorger, P. K. Non-genetic origins of cell-to-cell variability in TRAIL-induced apoptosis. *Nature* **459**, 428-432, doi:10.1038/nature08012 (2009).

105   Chang, H. H., Hemberg, M., Barahona, M., Ingber, D. E. & Huang, S. Transcriptome-wide noise controls lineage choice in mammalian progenitor cells. *Nature* **453**, 544-547, doi:10.1038/nature06965 (2008).

106   Waks, Z., Klein, A. M. & Silver, P. A. Cell-to-cell variability of alternative RNA splicing. *Molecular systems biology* **7**, 506, doi:10.1038/msb.2011.32 (2011).

107   Rea, D., Rousselot, P., Guilhot, J., Guilhot, F. & Mahon, F. X. Curing chronic myeloid leukemia. *Current hematologic malignancy reports* **7**, 103-108, doi:10.1007/s11899-012-0117-2 (2012).

108   Bachmann, J. *et al.* Predictive mathematical models of cancer signalling pathways. *Journal of internal medicine* **271**, 155-165, doi:10.1111/j.1365-2796.2011.02492.x (2012).

109   Kitano, H. Computational systems biology. *Nature* **420**, 206-210, doi:10.1038/nature01254 (2002).

110   Aldridge, B. B., Burke, J. M., Lauffenburger, D. A. & Sorger, P. K. Physicochemical modelling of cell signalling pathways. *Nature cell biology* **8**, 1195-1203, doi:10.1038/ncb1497 (2006).

111   Chen, W. W., Niepel, M. & Sorger, P. K. Classic and contemporary approaches to modeling biochemical reactions. *Genes & development* **24**, 1861-1875, doi:10.1101/gad.1945410 (2010).

112   Swameye, I., Muller, T. G., Timmer, J., Sandra, O. & Klingmuller, U. Identification of nucleocytoplasmic cycling as a remote sensor in cellular signaling by databased modeling. *Proc Natl Acad Sci U S A* **100**, 1028-1033, doi:10.1073/pnas.0237333100 (2003).

113   Kanehisa, M. *et al.* KEGG for linking genomes to life and the environment. *Nucleic acids research* **36**, D480-484, doi:10.1093/nar/gkm882 (2008).

114   Samanta T, G. J. Model selection - An overview. *Curr Sci* **80**, 135–144 (2001).

115   Kreutz, C. & Timmer, J. Systems biology: experimental design. *The FEBS journal* **276**, 923-942, doi:10.1111/j.1742-4658.2008.06843.x (2009).

116   Ehemann, V., Sykora, J., Vera-Delgado, J., Lange, A. & Otto, H. F. Flow cytometric detection of spontaneous apoptosis in human breast cancer using the TUNEL-technique. *Cancer letters* **194**, 125-131 (2003).

117   Schilling, M. *et al.* Computational processing and error reduction strategies for standardized quantitative data in biological networks. *The FEBS journal* **272**, 6400-6411, doi:10.1111/j.1742-4658.2005.05037.x (2005).

118   Raue, A. *et al.* Lessons learned from quantitative dynamical modeling in systems biology. *PloS one* **8**, e74335, doi:10.1371/journal.pone.0074335 (2013).

119   Hindmarsh, A. C. *et al.* SUNDI- ALS: Suite of nonlinear and differential/algebraic equation solvers. *ACM T Math Software* **3**, 363-396 (2005).

120   Raue, A. *et al.* Structural and practical identifiability analysis of partially observed dynamical models by exploiting the profile likelihood. *Bioinformatics* **25**, 1923-1929, doi:10.1093/bioinformatics/btp358 (2009).

121   Piccolo, S. R. *et al.* A single-sample microarray normalization method to facilitate personalized-medicine workflows. *Genomics* **100**, 337-344, doi:10.1016/j.ygeno.2012.08.003 (2012).

122   Brossard, C. *et al.* Principles and Applications of Particle Image Velocimetry. *Aerospace Lab J*, 1-11 (2009).

123   Sveen, J. K. *An introduction to MatPIV v. 1.6.1.: Mechanics and Applied Mathematics. vol.2* (Dept. of Mathematics, University of Oslo., 2004).

124   Olivo-Marin, J.-C. Extraction of spots in biological images using multiscale products. *Pattern Recognition* **35**, 1989-1996 (2002).

125   Liu, J. *et al.* in *IEEE International Conference on Image Processing*   3893-3896 (2009).

126   Murphy, L. O., MacKeigan, J. P. & Blenis, J. A Network of Immediate Early Gene Products Propagates Subtle Differences in Mitogen-Activated Protein Kinase Signal Amplitude and Duration. *Molecular and cellular biology* **24**, 144-153, doi:10.1128/mcb.24.1.144-153.2004 (2003).

127   Kholodenko, B. N. Cell-signalling dynamics in time and space. *Nature reviews. Molecular cell biology* **7**, 165-176, doi:10.1038/nrm1838 (2006).

128   Nakakuki, T. *et al.* Ligand-specific c-Fos expression emerges from the spatiotemporal control of ErbB network dynamics. *Cell* **141**, 884-896, doi:10.1016/j.cell.2010.03.054 (2010).

129   Liang, C. C., Park, A. Y. & Guan, J. L. In vitro scratch assay: a convenient and inexpensive method for analysis of cell migration in vitro. *Nature protocols* **2**, 329-333, doi:10.1038/nprot.2007.30 (2007).

130   Petitjean, L. *et al.* Velocity fields in a collectively migrating epithelium. *Biophysical journal* **98**, 1790-1800, doi:10.1016/j.bpj.2010.01.030 (2010).

131   Czirok, A., Varga, K., Mehes, E. & Szabo, A. Collective cell streams in epithelial monolayers depend on cell adhesion. *New journal of physics* **15**, doi:10.1088/1367-2630/15/7/075006 (2013).

132   Flaherty, B., McGarry, J. P. & McHugh, P. E. Mathematical Models of Cell Motility. *Cell biochemistry and biophysics* **49**, 14-28, doi:10.1007/s12013-007-0045-2 (2007).

133   Maly, I. V. & Borisy, G. G. Self-organization of a propulsive actin network as an evolutionary process. *Proc Natl Acad Sci U S A* **98**, 11324-11329, doi:10.1073/pnas.181338798 (2001).

134   Graner, F. & Glazier, J. A. Simulation of biological cell sorting using a two-dimensional extended Potts model. *Phys Rev Lett* **69**, 2013-2016 (1992).

135   Sepulveda, N. *et al.* Collective cell motion in an epithelial sheet can be quantitatively described by a stochastic interacting particle model. *PLoS computational biology* **9**, e1002944, doi:10.1371/journal.pcbi.1002944 (2013).

136   Middleton, A. M., Fleck, C. & Grima, R. A continuum approximation to an off-lattice individual-cell based model of cell migration and adhesion. *Journal of theoretical biology* **359**, 220-232, doi:10.1016/j.jtbi.2014.06.011 (2014).

137   Perel, P. *et al.* Comparison of treatment effects between animal experiments and clinical trials: systematic review. *Bmj* **334**, 197, doi:10.1136/bmj.39048.407928.BE (2007).

138   Abbott, A. Cell culture: biology's new dimension. *Nature* **424**, 870-872, doi:10.1038/424870a (2003).

139   Friedrich, J., Seidel, C., Ebner, R. & Kunz-Schughart, L. A. Spheroid-based drug screen: considerations and practical approach. *Nature protocols* **4**, 309-324, doi:10.1038/nprot.2008.226 (2009).

140   Desoize, B. & Jardillier, J. Multicellular resistance: a paradigm for clinical resistance? *Critical reviews in oncology/hematology* **36**, 193-207 (2000).

141   Hirschhaeuser, F. *et al.* Multicellular tumor spheroids: an underestimated tool is catching up again. *Journal of biotechnology* **148**, 3-15, doi:10.1016/j.jbiotec.2010.01.012 (2010).

142   Breslin, S. & O'Driscoll, L. Three-dimensional cell culture: the missing link in drug discovery. *Drug discovery today* **18**, 240-249, doi:10.1016/j.drudis.2012.10.003 (2013).

143   Hoque, M. T., Windus, L. C., Lovitt, C. J. & Avery, V. M. PCaAnalyser: a 2D-image analysis based module for effective determination of prostate cancer progression in 3D culture. *PloS one* **8**, e79865, doi:10.1371/journal.pone.0079865 (2013).

144   Chen, W. *et al.* High-throughput image analysis of tumor spheroids: a user-friendly software application to measure the size of spheroids automatically and accurately. *Journal of visualized experiments : JoVE*, doi:10.3791/51639 (2014).

145   Evensen, N. A. *et al.* Development of a high-throughput three-dimensional invasion assay for anti-cancer drug discovery. *PloS one* **8**, e82811, doi:10.1371/journal.pone.0082811 (2013).

146   Purschke, M., Rubio, N., Held, K. D. & Redmond, R. W. Phototoxicity of Hoechst 33342 in time-lapse fluorescence microscopy. *Photochemical & photobiological sciences : Official journal of the European Photochemistry Association and the European Society for Photobiology* **9**, 1634-1639, doi:10.1039/c0pp00234h (2010).

147   Chen, Y., Wise, S. M., Shenoy, V. B. & Lowengrub, J. S. A stable scheme for a nonlinear, multiphase tumor growth model with an elastic membrane. *International journal for numerical methods in biomedical engineering* **30**, 726-754, doi:10.1002/cnm.2624 (2014).

148   Wise, S. M., Lowengrub, J. S., Frieboes, H. B. & Cristini, V. Three-dimensional multispecies nonlinear tumor growth--I Model and numerical method. *Journal of theoretical biology* **253**, 524-543, doi:10.1016/j.jtbi.2008.03.027 (2008).

149   Drasdo, D., Hoehme, S. & Block, M. On the Role of Physics in the Growth and Pattern Formation of Multi-Cellular Systems: What can we Learn from Individual-Cell Based Models? *Journal of Statistical Physics* **128**, 287-345, doi:10.1007/s10955-007-9289-x (2007).

150   Frieboes, H. B. *et al.* An integrated computational/experimental model of lymphoma growth. *PLoS computational biology* **9**, e1003008, doi:10.1371/journal.pcbi.1003008 (2013).

151   Macklin, P., Mumenthaler, S. & Lowengrub, J. in *Multiscale Computer Modeling in Biomechanics and Biomedical Engineering*   (ed Amit Gefen) Ch. 13, 349-380 (Springer, 2013).

152   Macklin, P. & Edgerton, M. E. in *Multiscale modeling of cancer: an integrated experimental and mathematical modeling approach*   (ed John Lowengrub) 206-234 (Cambridge University Press, 2010).

153   Olsen, J. V. *et al.* Global, in vivo, and site-specific phosphorylation dynamics in signaling networks. *Cell* **127**, 635-648, doi:10.1016/j.cell.2006.09.026 (2006).

154   Nguyen, L. K., Matallanas, D., Croucher, D. R., von Kriegsheim, A. & Kholodenko, B. N. Signalling by protein phosphatases and drug development: a systems-centred view. *The FEBS journal* **280**, 751-765, doi:10.1111/j.1742-4658.2012.08522.x (2013).

155   Hornbeck, P. V. *et al.* PhosphoSitePlus, 2014: mutations, PTMs and recalibrations. *Nucleic acids research* **43**, D512-520, doi:10.1093/nar/gku1267 (2015).

156   Jiang, X., Huang, F., Marusyk, A. & Sorkin, A. Grb2 regulates internalization of EGF receptors through clathrin-coated pits. *Molecular biology of the cell* **14**, 858-870, doi:10.1091/mbc.E02-08-0532 (2003).

157   Tanos, B. & Pendergast, A. M. Abl tyrosine kinase regulates endocytosis of the epidermal growth factor receptor. *The Journal of biological chemistry* **281**, 32714-32723, doi:10.1074/jbc.M603126200 (2006).

158   Goh, L. K. & Sorkin, A. Endocytosis of receptor tyrosine kinases. *Cold Spring Harbor perspectives in biology* **5**, a017459, doi:10.1101/cshperspect.a017459 (2013).

159   Guvakova, M. A. *et al.* The small GTPase Rap1 promotes cell movement rather than stabilizes adhesion in epithelial cells responding to insulin-like growth factor I. *The Biochemical journal* **463**, 257-270, doi:10.1042/BJ20131638 (2014).

160   Hallak, H. *et al.* Epidermal growth factor-induced activation of the insulin-like growth factor I receptor in rat hepatocytes. *Hepatology* **36**, 1509-1518, doi:10.1053/jhep.2002.37138 (2002).

161   Lange, F., Rateitschak, K., Kossow, C., Wolkenhauer, O. & Jaster, R. Insights into erlotinib action in pancreatic cancer cells using a combined experimental and mathematical approach. *World journal of gastroenterology : WJG* **18**, 6226-6234, doi:10.3748/wjg.v18.i43.6226 (2012).

162   Ma, X. & Bai, Y. IGF-1 activates the P13K/AKT signaling pathway via upregulation of secretory clusterin. *Molecular medicine reports* **6**, 1433-1437, doi:10.3892/mmr.2012.1110 (2012).

163   Miyazaki, M., McCarthy, J. J. & Esser, K. A. Insulin like growth factor-1-induced phosphorylation and altered distribution of tuberous sclerosis complex (TSC)1/TSC2 in C2C12 myotubes. *The FEBS journal* **277**, 2180-2191, doi:10.1111/j.1742-4658.2010.07635.x (2010).

164   Bijur, G. N. & Jope, R. S. Rapid accumulation of Akt in mitochondria following phosphatidylinositol 3-kinase activation. *J Neurochem* **87**, 1427-1435, doi:10.1046/j.1471-4159.2003.02113.x (2003).

165   Hahn, B. *et al.* One-source peptide/phosphopeptide standards for accurate phosphorylation degree determination. *Proteomics* **11**, 490-494, doi:10.1002/pmic.201000569 (2011).

166   Girnita, A. *et al.* Cyclolignans as inhibitors of the insulin-like growth factor-1 receptor and malignant cell growth. *Cancer research* **64**, 236-242 (2004).

167   Wiley, H. S., Shvartsman, S. Y. & Lauffenburger, D. A. Computational modeling of the EGF-receptor system: a paradigm for systems biology. *Trends in cell biology* **13**, 43-50 (2003).

168   Schoeberl, B., Eichler-Jonsson, C., Gilles, E. D. & Muller, G. Computational modeling of the dynamics of the MAP kinase cascade activated by surface and internalized EGF receptors. *Nature biotechnology* **20**, 370-375, doi:10.1038/nbt0402-370 (2002).

169   Bianconi, F. *et al.* Computational model of EGFR and IGF1R pathways in lung cancer: a Systems Biology approach for Translational Oncology. *Biotechnology advances* **30**, 142-153, doi:10.1016/j.biotechadv.2011.05.010 (2012).

170   Csete, M. E. & Doyle, J. C. Reverse engineering of biological complexity. *Science* **295**, 1664-1669, doi:10.1126/science.1069981 (2002).

171   Peled, N. *et al.* Insulin-like growth factor-1 receptor (IGF-1R) as a biomarker for resistance to the tyrosine kinase inhibitor gefitinib in non-small cell lung cancer. *Cellular oncology* **36**, 277-288, doi:10.1007/s13402-013-0133-9 (2013).

172   Gong, Y. *et al.* High expression levels of total IGF-1R and sensitivity of NSCLC cells in vitro to an anti-IGF-1R antibody (R1507). *PloS one* **4**, e7273, doi:10.1371/journal.pone.0007273 (2009).

173   Noll, K., Wegmann, B. R., Havemann, K. & Jaques, G. Insulin-like growth factors stimulate the release of insulin-like growth factor-binding protein-3 (IGFBP-3) and degradation of IGFBP-4 in nonsmall cell lung cancer cell lines. *J Clin Endocrinol Metab* **81**, 2653-2662, doi:10.1210/jcem.81.7.8675593 (1996).

174   Haase, H. & Maret, W. Intracellular zinc fluctuations modulate protein tyrosine phosphatase activity in insulin/insulin-like growth factor-1 signaling. *Experimental Cell Research* **291**, 289-298, doi:10.1016/s0014-4827(03)00406-3 (2003).

175   Goustin, A. S., Leof, E. B., Shipley, G. D. & Moses, H. L. Growth factors and cancer. *Cancer research* **46**, 1015-1029 (1986).

176   Broekman, F., Giovannetti, E. & Peters, G. J. Tyrosine kinase inhibitors: Multi-targeted or single-targeted? *World journal of clinical oncology* **2**, 80-93, doi:10.5306/wjco.v2.i2.80 (2011).

177   Zhang, Q. *et al.* Discovery of EGFR selective 4,6-disubstituted pyrimidines from a combinatorial kinase-directed heterocycle library. *Journal of the American Chemical Society* **128**, 2182-2183, doi:10.1021/ja0567485 (2006).

178   Vasilcanu, R. *et al.* Picropodophyllin induces downregulation of the insulin-like growth factor 1 receptor: potential mechanistic involvement of Mdm2 and beta-arrestin1. *Oncogene* **27**, 1629-1638, doi:10.1038/sj.onc.1210797 (2008).

179   Liska, D., Chen, C. T., Bachleitner-Hofmann, T., Christensen, J. G. & Weiser, M. R. HGF rescues colorectal cancer cells from EGFR inhibition via MET activation. *Clinical cancer research : an official journal of the American Association for Cancer Research* **17**, 472-482, doi:10.1158/1078-0432.CCR-10-0568 (2011).

180   Tang, Z. *et al.* Dual MET-EGFR combinatorial inhibition against T790M-EGFR-mediated erlotinib-resistant lung cancer. *British journal of cancer* **99**, 911-922, doi:10.1038/sj.bjc.6604559 (2008).

181   Sie, M. *et al.* Growth-factor-driven rescue to receptor tyrosine kinase (RTK) inhibitors through Akt and Erk phosphorylation in pediatric low grade astrocytoma and ependymoma. *PloS one* **10**, e0122555, doi:10.1371/journal.pone.0122555 (2015).

182   Chien, W. *et al.* Suppression of cell proliferation and signaling transduction by connective tissue growth factor in non-small cell lung cancer cells. *Molecular cancer research : MCR* **4**, 591-598, doi:10.1158/1541-7786.MCR-06-0029 (2006).

183   So, W. K. *et al.* Amphiregulin induces human ovarian cancer cell invasion by down-regulating E-cadherin expression. *FEBS letters* **588**, 3998-4007, doi:10.1016/j.febslet.2014.09.017 (2014).

184   Hurbin, A. *et al.* Cooperation of amphiregulin and insulin-like growth factor-1 inhibits Bax- and Bad-mediated apoptosis via a protein kinase C-dependent pathway in non-

small cell lung cancer cells. *The Journal of biological chemistry* **280**, 19757-19767, doi:10.1074/jbc.M413516200 (2005).

185   Busser, B., Coll, J. L. & Hurbin, A. The increasing role of amphiregulin in non-small cell lung cancer. *Pathologie-biologie* **57**, 511-512, doi:10.1016/j.patbio.2008.10.002 (2009).

186   Luppi, F., Longo, A. M., de Boer, W. I., Rabe, K. F. & Hiemstra, P. S. Interleukin-8 stimulates cell proliferation in non-small cell lung cancer through epidermal growth factor receptor transactivation. *Lung Cancer* **56**, 25-33, doi:10.1016/j.lungcan.2006.11.014 (2007).

187   Li, S. *et al.* TWIST1 associates with NF-kappaB subunit RELA via carboxyl-terminal WR domain to promote cell autonomous invasion through IL8 production. *BMC biology* **10**, 73, doi:10.1186/1741-7007-10-73 (2012).

188   Friedl, P. & Wolf, K. Tumour-cell invasion and migration: diversity and escape mechanisms. *Nature reviews. Cancer* **3**, 362-374, doi:10.1038/nrc1075 (2003).

189   Wei, Y. *et al.* CHCHD2 is Co-amplified with EGFR in NSCLC and Regulates Mitochondrial Function and Cell Migration. *Molecular cancer research : MCR*, doi:10.1158/1541-7786.MCR-14-0165-T (2015).

190   Cui, T. *et al.* XPC inhibits NSCLC cell proliferation and migration by enhancing E-Cadherin expression. *Oncotarget* **6**, 10060-10072 (2015).

191   Sequist, L. V. *et al.* Genotypic and histological evolution of lung cancers acquiring resistance to EGFR inhibitors. *Science translational medicine* **3**, 75ra26, doi:10.1126/scitranslmed.3002003 (2011).

192   Engelman, J. A. *et al.* PF00299804, an irreversible pan-ERBB inhibitor, is effective in lung cancer models with EGFR and ERBB2 mutations that are resistant to gefitinib. *Cancer research* **67**, 11924-11932, doi:10.1158/0008-5472.CAN-07-1885 (2007).

193   Miller, V. A. *et al.* Phase IIB/III Double-Blind Randomized Trial of Afatinib (BIBW2992, an Irreversible Inhibitor of EGFR/HER1 and HER2) + Best Supportive Care (BSC) Versus Placebo + BSC in Patients with NSCLC Failing 1–2 Lines of Chemotherapy and Erlotinib or Gefitinib (LUX-LUNG 1). *Annals of Oncology*, LBA1 (2010).

194   Sequist, L. V. *et al.* Neratinib, an irreversible pan-ErbB receptor tyrosine kinase inhibitor: results of a phase II trial in patients with advanced non-small-cell lung cancer. *Journal of clinical oncology : official journal of the American Society of Clinical Oncology* **28**, 3076-3083, doi:10.1200/JCO.2009.27.9414 (2010).

195   Chmielecki, J. *et al.* Optimization of Dosing for EGFR-Mutant Non-Small Cell Lung Cancer with Evolutionary Cancer Modeling. *Science translational medicine* **3**, doi:ARTN 90ra59 DOI 10.1126/scitranslmed.3002356 (2011).

196   Godin-Heymann, N. *et al.* The T790M "gatekeeper" mutation in EGFR mediates resistance to low concentrations of an irreversible EGFR inhibitor. *Molecular cancer therapeutics* **7**, 874-879, doi:10.1158/1535-7163.MCT-07-2387 (2008).

197   Cortes-Sempere, M. *et al.* IGFBP-3 methylation-derived deficiency mediates the resistance to cisplatin through the activation of the IGFIR/Akt pathway in non-small cell lung cancer. *Oncogene* **32**, 1274-1283, doi:10.1038/onc.2012.146 (2013).

7 Danksagung

ERKLÄRUNG GEMÄß § 8 (3B, C) DER PROMOTIONSORDNUNG

Hiermit erkläre ich, dass ich die vorgelegte Dissertation mit dem Titel „Interactions of EGFR / IGF-1R Signaling in NSCLC – A Systems Biology Approach" selbst verfasst und mich dabei keiner anderen als der von mir ausdrücklich bezeichneten Quellen und Hilfen bedient habe. Des Weiteren bestätige ich, dass ich an keiner anderen Stelle ein Prüfungsverfahren beantragt bzw. die Dissertation in dieser oder anderer Form bereits anderweitig als Prüfungsarbeit verwendet oder einer anderen Fakultät als Dissertation vorgelegt habe.

Heidelberg, den

Benedikt Müller